Cardiac Activation Mapping using Ultrasound Current Source Density Imaging

by

Ragnar Olafsson

A dissertation submitted in partial fulfillment
of the requirements for the degree of
Doctor of Philosophy
(Biomedical Engineering)
in The University of Michigan
2008

Doctoral Committee:

Professor Matthew O'Donnell, Chair
Professor Daryl R. Kipke
Professor Douglas C. Noll
Associate Professor J. Brian Fowlkes
Associate Professor Hakan Oral
Assistant Professor Russell S. Witte, University of Arizona

2008

Tileinkað mömmu, pabba og Bjarna fyrir stuðning þeirra og ást.

ACKNOWLEDGEMENTS

I am grateful to the many people that have accompanied, helped and encouraged me in order to get to this point.

I would like start by thanking my parents for their love, support and encouragement to succeed both as a person and a professional. I would also like to thank Christine for her love and support.

I would like to thank my thesis advisor, Dr. Matthew O'Donnell for his great support, encouragement and very solid advise on my road to the Ph.D. It has been a privilege to have been his student. I am a much better researcher, engineer, presenter, and writer because of him. I am grateful for his enthusiasm for crazy ideas and for creating the great environment and atmosphere that the BUL lab has been.

I would also like to thank my dissertation committee: Professors Matthew O'Donnell, Douglas C. Noll, J. Brian Fowlkes, Daryl R. Kipke, Hakan Oral and Russell S. Witte, University of Arizona, for their help and service. I would especially like to thank Russell Witte who has been my mentor and co-worker since I came to Ann Arbor and given me solid and critical advise and help at every turn. The idea behind this work came initially from him and we have worked together on this project hand-in hand.

A special thanks to my pals in the BUL lab, past and present, for making grad school such a great experience. I would like to particularly thank my dear friends Congxian Jia, my partner during all those long cold nights, morning and days doing rabbit experiments, Sheng-Wen, for all the help and advise, Kang for his support and good discussion and

Tim for all his help. I would also like to thank Shai Ashkenazi, Frank Winterroth, Marwa Zhody, Todd Erpelding, Becca Booi, Yan Shi, Zhen Xu, Tak Buma, Xunchang Chen, Javier de Ana, Binh Tran, Zhen-Zhen Fang, Tzu-Yin Wang, Hua Xie, Kyle Hollman and the rest of the BULlies, for their great camaraderie and friendship.

I would also like to thank Nancy Roeser and Kimberly Ives for their generous help and training and Adam Lauver and Erin Booth for their help with the Langendorff setup.

I am thankful for the support of the Fulbright program at the U.S. Department of State and the National Institutes of Health for their financial support throughout my studies. Thanks also to the fantastic BME department staff for all their help, with special thanks to Maria Steele, Kristin Romelhardt, Deb Lyons, and Tonya Brown.

TABLE OF CONTENTS

LIST OF FIGURES

LIST OF TABLES

LIST OF MOVIES

CHAPTER 1
INTRODUCTION

1.1. Motivation

Cardiac arrhythmia is a serious health problem whose prevalence increases as the population ages. Over 2.2 million U.S. citizen suffer from atrial fibrillation and 400,000 deaths are attributed to ventricular fibrillation annually [1, 2]. In advanced cases when drug therapy is ineffective, the arrhythmia can be treated through either ablation or resynchronization therapy. These interventions are planned and evaluated through mapping of the activation sequence. Traditional mapping techniques are done through time-consuming sequential mapping, are guided by fluoroscopy and place significant demands on the operator for mentally visualizing the activation [3]. In the last 10-15 years these procedures have been improved through the use of electro-anatomical mapping. These techniques record the spatial location of the mapping catheter with respect to a reference coordinate system. By moving the catheter around the cardiac chamber of interest, the operator can sequentially build up a computerized map of the cardiac anatomy and the activation pattern. This reduces fluoroscopy time and facilitates the visualization of the arrhythmia [4-6]. However, these maps are coarse, the sequential mapping procedure is slow and the geometric reference they provide is static, being acquired with electrocardiogram (ECG) gating. These techniques are therefore inadequate for mapping complex, unstable arrhythmia.

Non-contact mapping has been developed to reduce mapping time. In non-contact mapping the endocardial distribution is estimated from far field potentials, measured with a free floating array catheter, by solving an inverse problem. In principle this allows the operator to map the entire endocardial surface in a single heart beat [7]. As a result, the beat to beat variability of unstable arrhythmia can be captured. However, the inverse problem is highly underdetermined and ill posed and thus sensitive to geometrical errors and electronic noise [8].

Presurgical imaging with Computed Tomography (CT) and Magnetic Resonance Imaging (MRI) provide anatomical images of the heart to help guide the procedure, whereas ultrasound pulse-echo imaging provides real-time feedback of the endocardium's morphology [9-14]. The registration process is not perfect and the registration error between the high resolution CT/MR images, intracardiac pulse echo, and electroantomical maps can be significant [15, 16].

The motivation for this thesis was to develop a new imaging method, Ultrasound Current Source Density Imaging (UCSDI) that could potentially improve on the existing methods. UCSDI is based on the acoustoelectric (AE) effect, a pressure modulated change in electric conductivity [17]. By combining an electronically steered ultrasonic beam with an array of electrodes, this method has the potential to rapidly map the cardiac activation wave with high spatial resolution determined by the ultrasonic point spread function. A further advantage of this method is that UCSDI is automatically registered to B-mode ultrasound because the same acoustic wave produces both.

1.2. The Cardiac Activation Wave

1.2.1. Spreading of the Activation Wave

The role of the activation wave is to control the contraction of the heart. The anatomy of the heart and its conduction pathways are shown in Fig. 1.1. The wave starts in the sino-atrial (SA) node which is a bundle of specialized muscle cells in the right atrium next to the vena cava. It is under the ultimate control of the nervous system but has an intrinsic rate of firing of ~70 beats-per-minute (bpm). The wave spreads from the SA node throughout the atria, causing them to contract. The atria are largely electrically insulated from the ventricles except at the atrio-ventricular (AV) node. Wave propagation through the node is slow, which allows the ventricles to fill completely prior to contraction. From the AV node the wave enters the specialized conduction system composed of the His-bundle, the right and left bundle branches and the Purkinje fibers. The propagation speed within the specialized conduction is faster (3-4 m/s) than in normal myocardium (0.5-1 m/s). This allows it to spread the activation wave throughout the endocardial surface, first at the septum then from the apex to the base. This ensures that as the wave propagates from the endocardium outwards the entire myocardium is activated simultaneously, resulting in a uniform contraction. [18, 19].

1.2.2. Cardiac Current Density Modeled as a Sheet of Dipoles

The cardiac activation wave can be modeled in terms of equivalent current density to estimate its spatial extent and magnitude. For a single isolated fiber of circular cross section the equivalent current density, $\mathbf{J}_{sf}$, is

$$\mathbf{J}_{sf} = -\sigma_i \frac{\partial V_m}{\partial x}\mathbf{i}. \qquad (1.1)$$

where the fiber lies along the x-axis, **i** is the unit vector along the x-axis, σ_i is the intracellular conductivity and V_m is the membrane potential. Idealized shape and values for V_m, and $\partial V_m/\partial x$ in cardiac tissue are shown as a function of x in Fig. 1.2. V_m(t) satisfies the wave equation due to the regenerative properties of excitable membranes. Assuming these idealized parameters and σ_i=2mS/cm the equivalent peak current density is ~5 mA/cm^2.

The extension of equation (1.1) to three dimensions in an infinite homogenous myocardium is

$$\mathbf{J}_{ds} = -\sigma_i \nabla V_m. \qquad (1.2)$$

Equation (1.2) describes, $\mathbf{J}_{ds}$, a 1-mm wide, gaussian shaped, sheet of dipoles or double layer of current sources propagating in 3D [20].

1.3. Arrhythmias and Their Mechanism

Arrhythmia is a condition when the heart beats incorrectly due to abnormal generation or propagation of the activation wave. It is classified according to timing into bradycardias, tachycardias, and premature beats and according to the anatomical location into ventricular and supraventricular arrhythmias as well as blockages of the bundle branches and Purkinje fiber system. Supraventricular arrhythmias are problems in the atria, pulmonary veins, the sinus node and the junction between the atria and ventricles (junctional rhythm) [18].

Bradycardias (slowing of the cardiac rhythm) is commonly caused by a congenital condition, AV block, sick sinus dysfunction or medication [21, 22]. Tachycardia, a condition where the rate of impulses is more rapid than the normal heart beat, is due to either focal discharge or reentry [23, 24]. Focal discharge in the atria commonly originates in the pulmonary veins through a poorly understood mechanism [25-27] while focal discharge in the ventricles arises most commonly during acute ischemia at the border between ischemic and healthy tissue [28]. One reason for this focal discharge is an injury current due to a gradient in extracellular potassium across the boundary. Extracellular potassium concentration increases in the ischemic zone because cellular potassium pumps become less efficient due to lack of energy [29, 30].

Reentry is a condition where the impulse travels along a circuitous route that may or may not be stationary. There are two requisites for reentry to occur: there has to be a unidirectional block of conduction and the wave has to take longer to propagate along the path than the longest refractory period [24]. Reentry is subdivided further into anatomic and functional reentry. In anatomical reentry the wave travels around a anatomical structure such as an artery or region with reduced or no excitability, for example due to infarction, while functional reentry is caused when an activation wave encounters a region of healthy tissue in refraction [24].

1.4. Cardiac Activation Mapping Technologies.

1.4.1. Traditional Catheter Mapping Techniques

Traditional catheter mapping is guided by fluoroscopy and uses both fixed curve electrode catheters, placed for reference in key anatomical positions, and steerable mapping and ablation catheters. The choice of reference positions is guided by pre-operative analysis of surface ECG and the arrhythmia being treated. The arrhythmogenic regions are found through an interactive combination of activation mapping and pacing. The activation mapping is done sequentially with a mapping catheter and the operator builds the activation map mentally. Pacing is used to identify if a particular position is at the focus of an arrhythmia or a part of a reentrant circuit by sending pacing pulses at a rate that matches the arrhythmia. If during pacing the endocardial electrograms and surface ECG match those during arrhythmia, the position is declared a part of an arrhythmogenic region [31].

Because these techniques require a mental representation of the cardiac currents, they may be adequate for characterizing basic arrhythmias, but not complex and unstable reentrant circuits [3]. To overcome some of these short-comings these techniques have for the last 10-15 years been augmented with electroanatomic and noncontact mapping.

1.4.2. Electroanatomic Mapping

There are three main catheter-based technologies in clinical use for endocardial geometric mapping and catheter guidance: triangulation by magnetic fields, electric fields, or ultrasound. The mapping is performed in a similar way for all of these

technologies. The mapping catheter, which has a sensor at its tip, is moved sequentially around the cardiac chamber of interest. At each location the position of the catheter tip is triangulated and the position is recorded at a certain point in the cardiac cycle through ECG gating [3, 31]. In addition to facilitating mapping of complex arrhythmia the key advantage of electroanatomical mapping is reduction in fluoroscopy time needed [32, 33]. This is significant since for every 1 hr of fluoroscopy the risk of fatal malignancy is 0.7-1 per 1000 patients [34].

In the CARTO™ system from Biosense Webster the mapping catheter has a magnetic sensor in its tip. Using this sensor to measure the magnetic field strength emitted by three coils located under the patients the location of the catheter can be triangulated. It was first demonstrated by Gepstein and co-workers [4] and is illustrated in Fig. 1.3. In their seminal paper they reported mean relative location error of 0.73±0.03 mm and good reproducibility of 0.73±0.05 mm. However, they did reject any point that wasn't stable enough with inter-cycle distance > 2 mm. In one study the time (mean±standard deviation) to acquire the 3D map of a chamber was 35.7±17.8 min [35].

Ensite™ Nav X™ uses generation and detection of electric field to locate the electrodes. The system has two configurations. In one (the LocaLisa system), electric fields are generated by three pairs of orthogonally placed skin electrodes and detected by catheter electrodes (see Fig. 1.4). The assumption is that the fields within the heart are unidirectional and the difference in potential measured by a catheter electrode at two different locations is proportional to the distance between them along the field direction. The localization accuracy of LocaLisa is better than 2 mm with reproducibility of 1.4±1.1 mm [5].

In the other configuration potential is generated between a mapping catheter and a catheter electrode array. The position of the mapping catheter relative to the array is derived from potentials measured with each array electrode and the known 3D shape of the array. The accuracy of the system, which was tested in phantoms by locating an electrode emitting a driving potential with an EP roving electrode, was determined to be 2.33±0.44 mm and 7.50±1.13 mm using inverse solution [7, 11].

The Realtime Position Management (RPM) System from Cardiac Pathways uses ultrasound transducers placed on the catheters as illustrated in Fig. 1.5. Two fixed curve catheters with four transducers each are used for reference and a steerable catheter with three transducers for mapping. The relative location of the catheters with respect to each other is obtained from time of flight measurements of acoustic pulses between the transducers. The reproducibility of this system is 2.0±1.2 mm [6].

The nominal accuracy (< 2 mm) of these methods is comparable to each other. As a result the sequential acquisition of these methods the mapping has to be performed over multiple cycles. As a result both cardiac and respiratory motion can negatively affect this accuracy such that the total accrued error can be 5-10 mm [36]. Ensite^{TM} is more flexible than either CARTO^{TM} or RPM because it can be used to locate any electrode catheter; it also does not require catheters with specialized sensors. On the other hand, the low frequency magnetic fields and the intracardiac ultrasound waves employed by CARTO and RPM respectively are not distorted by the body to the same degree as the low frequency electric fields employed by Ensite^{TM}. The common disadvantage shared by these methods is that it is performed over multiple cycles. As a result it is difficult to map unstable arrhythmias using this technology alone. To map unstable arrhythmias, non-

contact mapping has been developed.

1.4.3. Non-Contact Mapping

Non-contact mapping of the heart has been studied for decades using both intracardiac and surface electrodes [8]. The first intracardiac non-contact mapping using multielectrode catheter was done by Taccardi and co-workers in 1987 [37]. Intracavity non-contact mapping is accomplished by measuring far-field potentials with a multi-electrode catheter array and then solving an inverse problem to estimate the spatial distribution of electrical activity [8]. The two main approaches are potential mapping and activation sequence mapping, where the goal of potential mapping is to reconstruct the endocardial potential, whereas activation time mapping is only concerned with reconstructing the activation time for each part of the myocardium [38, 39]. Endocardial potential mapping has been developed into a clinically available system, Ensite^{TM}. In this system the endocardial potential at 3360 points is estimated from potential measurements on 64 electrodes on an electrode catheter by solving the inverse Laplace equation. A geometrical transfer matrix (size 3360 x 64) is calculated between the endocardial surface and the catheter [7, 11]. This problem is ill posed, and the solution space must be constrained to physiologically plausible outcomes. The solution of this inverse problem is sensitive to perturbation in the geometrical transfer matrix (or the geometrical estimation of the heart surface), as well as electronic noise [7, 8].

.

1.4.4. Registration of Electroanatomical Mapping with CT and MRI

The electro-anatomical methods described in 1.4.2 produce coarse maps of endocardial anatomy and take a long time to produce. To obtain greater anatomical detail, CT and MR images are obtained pre-operatively and then registered to the electro-anatomical map.

Registration is accomplished in three steps. First CT/MRI and electroanatomical coordinate systems are aligned. Second, a number of anatomical landmarks such as the aorta are selected and aligned between them. Finally, the average surface error between electro-anatomic points and the CT/MRI surface is minimized through an optimization algorithm [16, 40]. For good registration, CT/MR images and the electro-anatomical mapping must be obtained at the same point in both cardiac and respiratory cycles. There is even a measurable difference in cardiac dimensions between inspirational and expirational breath holding [41, 42]. Reports of the registration error of these methods are conflicting. Some report small average surface to surface errors of 1.33±0.96 mm and 2.3±0.4 mm [43, 44] while others report extremely large errors of 10-20 mm [15, 45].

1.5. Ultrasound Current Source Density Imaging (UCSDI)

1.5.1. Introduction

Ultrasound current source density imaging maps electric current distributions using the acousto-electric effect, focused ultrasound transducers, and electrode technology. We first proposed this technique in a conference paper [46] and demonstrated its sensitivity and generated first images with *in vitro* experiments [47].

1.5.2. The Acousto-Electric Effect

It has been known for just under a century that pressure affects the conductivity of electrolytes [17]. The first to study this effect using ultrasound was Fox in 1946 [48]. Interest in the phenomenon was revived recently by Jossinet, Lavandier and Cathignol [49]. The conductivity, σ, of a binary electrolyte can be written as

$$\sigma = \mathrm{F}\, k_{\pm}\, \alpha\, \mathrm{C}(z_{+}\hat{u}_{+} + z_{-}\hat{u}_{-}),\ [\mathrm{S\ m^{-1}}] \tag{1.3}$$

where F is the Faraday constant [96487 Coulomb $\mathrm{mol^{-1}}$], $k_{\pm}$=mean ionic activity, α=dissociation coefficient, C = volume concentration [$\mathrm{mol\ m^{-3}}$], $z_{\pm}$ = number of charges, $\hat{u}_{\pm}$ = electric ionic mobilities of anion/cation [$\mathrm{m^2V^{-1}s^{-1}}$] [17]. Most physiological ions are fully disassociated ($\alpha \approx 1$) and $k_{\pm} \approx 1$ at physiological concentrations. Therefore, the differentials of equation (1.3) are

$$\frac{\Delta\sigma}{\sigma} \approx \frac{\Delta C}{C} + \frac{\Delta(\hat{u}_{+} + \hat{u}_{-})}{(\hat{u}_{+} + \hat{u}_{-})}, \tag{1.4}$$

For short pulses and small pressures, the system can be assumed to be adiabatic. That is, thermal energy does not flow into or out of the system [50]. The ultrasound wave changes σ through two mechanisms. The primary mechanism is modulation of material density since the ionic charge density of physiological saline solutions is proportional to material density. The secondary mechanism is modulation of ionic mobility from adiabatic temperature change due to acoustic pressure. As a result, the change in σ, $\Delta\sigma$, due to a pressure wave with amplitude ΔP can be written as

$$\frac{\Delta\sigma}{\sigma} = K_I \Delta P, \tag{1.5}$$

where

$$K_I = \beta_s - H_P + \frac{\partial T}{\partial P}\frac{(\hat{u}_+ m_{T+} + \hat{u}_- m_{T-})}{(\hat{u}_+ + \hat{u}_-)}, \tag{1.6}$$

and β_s is the adiabatic compressibility of water. H_P is the change in ionic mobility due to the change of the viscosity of water with pressure and $m_{T\pm} \approx 0.02$ K^{-1} is the percent change in ionic mobility as a function of temperature.

The value of K_I for NaCl, KCl and $CaCl_2$ is 10^{-9} Pa^{-1} [17, 51]. The interaction constant K_I is stated for change in conductivity. The equivalent relationship to equation (1.5), in terms of resistivity is

$$\frac{\Delta\rho}{\rho_0} = -K_I \Delta P, \tag{1.7}$$

where $\Delta\rho$ is the resistivity change and ρ_0 the direct current (DC) resistivity.

1.5.3. Lead Fields and Voltage Measurement

A pair of electrodes is called a lead. A lead's sensitivity distribution is called its lead field, a vector field with dimensions of m^{-2}. Its shape and distribution are the same as that of the electric field when unit current is injected through the electrodes [20, 52]. The voltage measured by lead i, V_i, due to a distributed current source $\mathbf{J}^I = \mathbf{J}^I(x, y, z)$ is

$$\mathrm{V_i} = \iiint \rho\,(\tilde{\mathbf{J}}_\mathrm{i}^\mathrm{L} \bullet \mathbf{J}^\mathrm{I})\,\mathrm{dxdydz}, \tag{1.8}$$

where $\tilde{\mathbf{J}}_i^L = \tilde{\mathbf{J}}_i^L(x,y,z)$ is the lead field of lead i and $\rho = \rho(x,y,z)$ is the resistivity. Integration variables (such as x, y and z) are omitted from subsequent equations, except when needed for clarity.

1.5.4. Acousto-Electric Signal Equation

An approximation of the AE signal equation was presented in [17] and is rewritten here below

$$\Delta Z(t) \approx K_I \iint_{\text{path width}} s(x,y,z)\,\sigma(x,y,z)\,P(t)\,dv\,. \tag{1.9}$$

where the path width is the extent of the acoustic beam, *Z(t)* is the complex impedance measured with the electrodes, *P(t)* is the pressure waveform, *s(x,y,z)* is sensitivity region of the electrodes and dv is a differential volume element *dxdydz*. The authors define *s(x,y,z)* in a way that is equivalent to the dot product of the lead fields in equation (1.8) although they don't refer explicitly to the concept of lead fields.

We expand on these results by deriving the AE signal equation for focused ultrasound using a more complex model of the pressure field. At time *t* the ultrasound pressure field is $\Delta P = \Delta P(x,y,z,t)$ and using (1.7) the resistivity distribution is

$$\rho = \rho_0 - K_I \rho_0 \Delta P\,. \tag{1.10}$$

Substituting (1.10) into (1.8) leads to

$$V_i = \iiint \left(\tilde{\mathbf{J}}_i^L \bullet \mathbf{J}^I\right)\left(\rho_0 - K_I \rho_0 \Delta P\right) dx\,dy\,dz\,. \tag{1.11}$$

Expanding V_i gives

$$V_i = \underbrace{\iiint \left(\tilde{\mathbf{J}}_i^L \bullet \mathbf{J}^I\right)\rho_0 \, dxdydz}_{V_i^{LF}} + \underbrace{\iiint \left(\tilde{\mathbf{J}}_i^L \bullet \mathbf{J}^I\right)\left(-K_I \rho_0 \Delta P\right) dxdydz}_{V_i^{AE}}. \tag{1.12}$$

The first term, V_i^{LF}, represents the low frequency (DC – 10 kHz) content of V_i while the second term, V_i^{AE}, represents the high frequency (MHz) AE signal. In practice V_i^{LF} and V_i^{AE} can be separated using analog and digital filters. Within V_i^{AE} we expand the ultrasound pressure factor, ΔP, into its subcomponents such that

$$\Delta P(x, y, z, t) = P_0 \, b(x, y, z) \, a(t - z/c), \tag{1.13}$$

with ultrasound beam pattern *b*(x,y,z) defined with respect to the transducer at the origin with the beam parallel to the z-axis, P_0 the amplitude of the pressure pulse, and *a*(t) the pulse waveform. Inserting (1.13) into (1.12) we rewrite V_i^{AE} as

$$V_i^{AE}(x_1, y_1, t) = \iiint \underbrace{\left(\tilde{\mathbf{J}}_i^L \bullet \mathbf{J}^I\right)\rho_0}_{A} \underbrace{\left(-K_I \, b(x - x_1, y - y_1, z) \, P_0 \, a\left(t - \frac{z}{c}\right)\right)}_{B} dxdydz, \tag{1.14}$$

where $V_i^{AE}(x_1, y_1, t)$ represents the AE voltage trace measured when the ultrasound beam has been translated to (x_1,y_1).

There are two ways to think about equation (1.14). One way is to think of it from an imaging standpoint, where A is analogous to a reflectivity distribution while B is the one-way point spread function of the ultrasound system. The other way to think about it is from an electrophysiological point of view where B is a sifter/localizer of an electric measurement.

1.5.5. The Sifting Property of the Ultrasound Beam in UCSDI

Traditional inverse methods reconstruct electric current density from voltage measurements using (1.8). This is a projection of the entire unknown current density field onto the lead field of the recording electrodes. To resolve a 2D current density distribution on an N x M grid, with N and M integers, at least 2NM independent measurements are required; otherwise the problem is underdetermined [53].

The AE signal equation (1.14) is essentially the same as (1.8) except for the multiplicative factor of the ultrasonic beam pattern. The focal volume of a beam b(x,y,z) is typically an ellipsoid with short axis diameter of 1 mm and long axis diameter of 3-4 mm [54]. By contrast, the integration volume of a lead is on the order of centimeters. Because b(x,y,z) is small compared to the integration volume, it acts as a sifting function similar to a Dirac delta function. The AE voltage measurement is, therefore, only proportional to the projection of $\mathbf{J}^I$ onto the lead field local to the focal zone, not the entire field. Furthermore, the MHz frequency of a(t) is a spatial label distinguishing it from the low frequency voltage, V_i^{LF}, simultaneously measured by the electrodes.

The sifting property of b(x,y,z) is illustrated in Fig. 1.6. In this example two electrodes (+ and -) generate a dipole current distribution $\mathbf{J}^I$ (blue, dashed vector field) in a 2D circular bath and the ultrasound beam spot is presented as a dashed circle. Two different recording leads 1 and 2 are shown, which correspond to two different positions of the mobile recording electrode M. The lead fields of leads 1 and 2 are $\widetilde{\mathbf{J}}_1^L$ and $\widetilde{\mathbf{J}}_2^L$ and are depicted as red vector fields. Since $\widetilde{\mathbf{J}}_1^L$ is anti-parallel to $\mathbf{J}^I$ within the beam spot, the AE signal measured by lead 1 is relatively large. By contrast, as $\widetilde{\mathbf{J}}_2^L$ is roughly

orthogonal to $\mathbf{J}^I$, we expect the AE signal measured by lead 2 to be small. From this example, we see that $\mathbf{J}^I$ cannot be obtained using only one lead. To solve $\mathbf{J}^I$ from UCSD images, at least one independent lead field for each spatial dimension is required. That is, two measurements are required for a 2-D geometry, and three for a 3-D geometry. This is, however, a great improvement over conventional methods since only 3 leads are required to yield a fully determined inverse problem, and still retain good spatial resolution. The sifting property of $b(x,y,z)$, as well as the spatial label of the high frequency of $a(t)$, are two key enhancements to electrical mapping with UCSDI.

1.6. Overview of Thesis

The overview provided in this chapter has shown the need for an accurate and rapid mapping of the cardiac activation wave during intracardiac ablation treatment. Current methods provide a static geometric reference frame, have limited spatial resolution and are time-consuming. The objective of this dissertation is to describe a new method, Ultrasound Current Source Density Imaging, that can potentially improve on these existing methods for mapping cardiac activation currents.

Chapter 2 describes a validation study where UCSDI was used to map and reconstruct an artificially generated two-dimensional current distribution. The results were compared both to direct electrode mapping of the distribution as well as to the results of a conventional inverse algorithm.

Chapter 3 describes the first mapping of cardiac activation currents in an isolated rabbit heart using UCSDI. In this proof-of-principle study the motion of the heart was

reduced with an excitation-contraction decoupler to reduce any possible influence of motion on UCSDI measurements. The heart was stimulated alternatively from apex and right atrium and the timing of the UCSDI, measured on each pair of electrodes, was compared to ECG signals independently measured on the same electrodes.

Chapter 4 describes the first measurements of localized electromechanical delay in a live rabbit heart using a new method that combines UCSDI with phase sensitive ultrasound speckle tracking. The delay between UCSDI and both local displacement and strain was measured.

The dissertation concludes in Chapter 5 with a summary of the results and some thoughts on future work and clinical application.

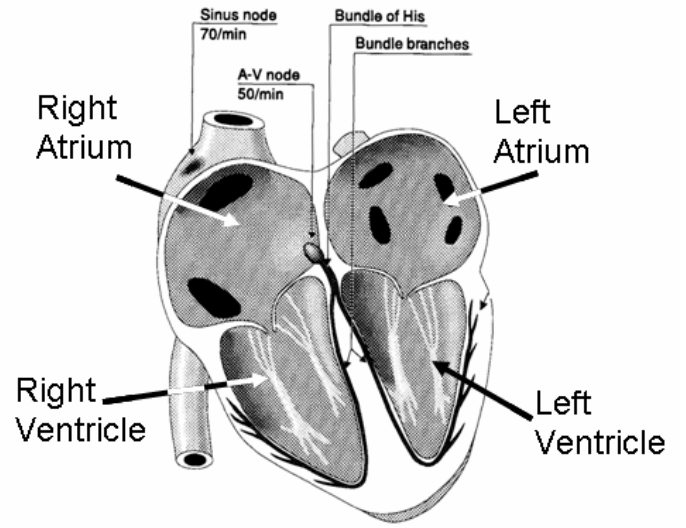

Figure 1.1. The conduction system and anatomy of the heart. Adapted from [19].

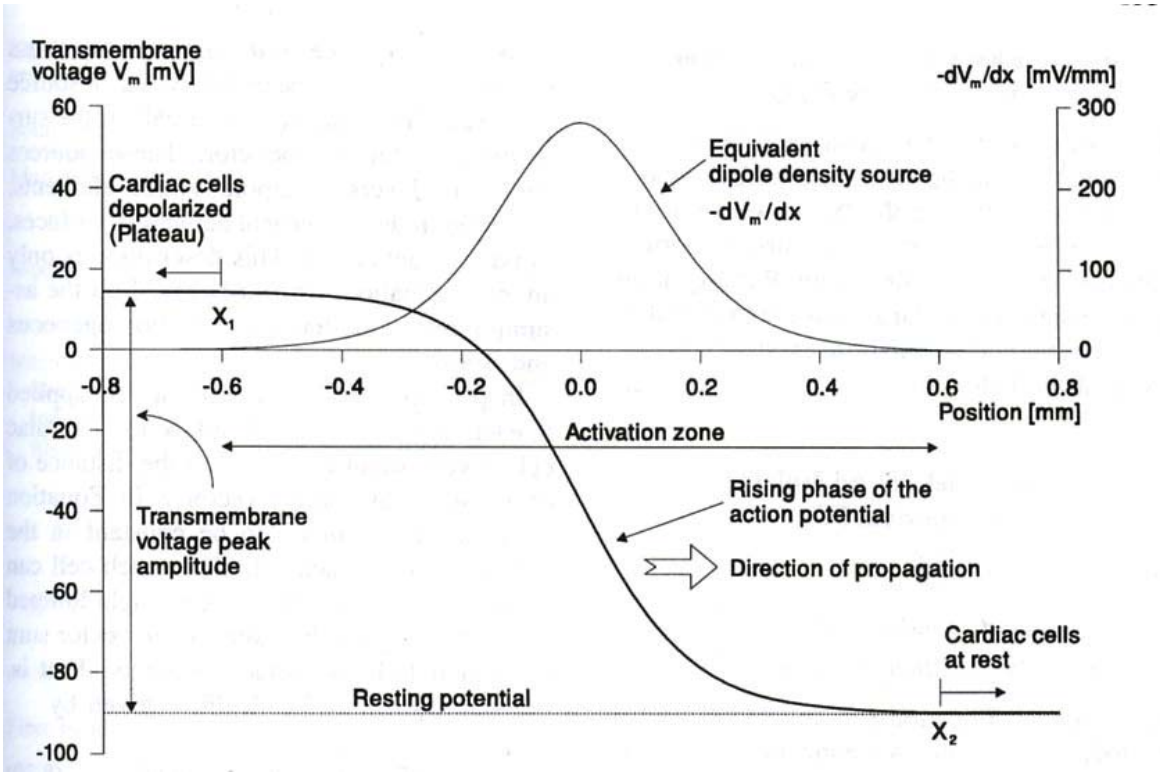

Figure 1.2. Idealized shape and values of the transmembrane voltage V_m and its spatial derivative $\partial V_m/\partial x$ as a function of space. Adapted from [55].

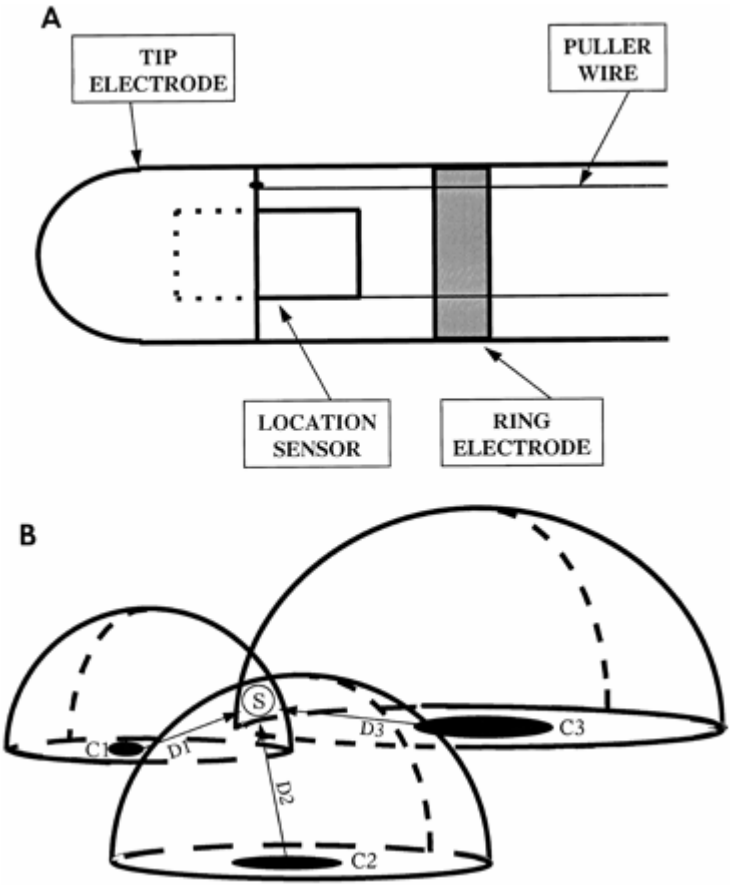

Figure 1.3. A schematic of the CARTO catheter localization system. Three magnetic coils (C1, C2, C3) emit weak temporally coded magnetic fields. A magnetic sensor (S) on the catheter measures the field strength of each coil and from the field decay estimates the relative distance (D1, D2, D3) to each coil. Adapted from [4].

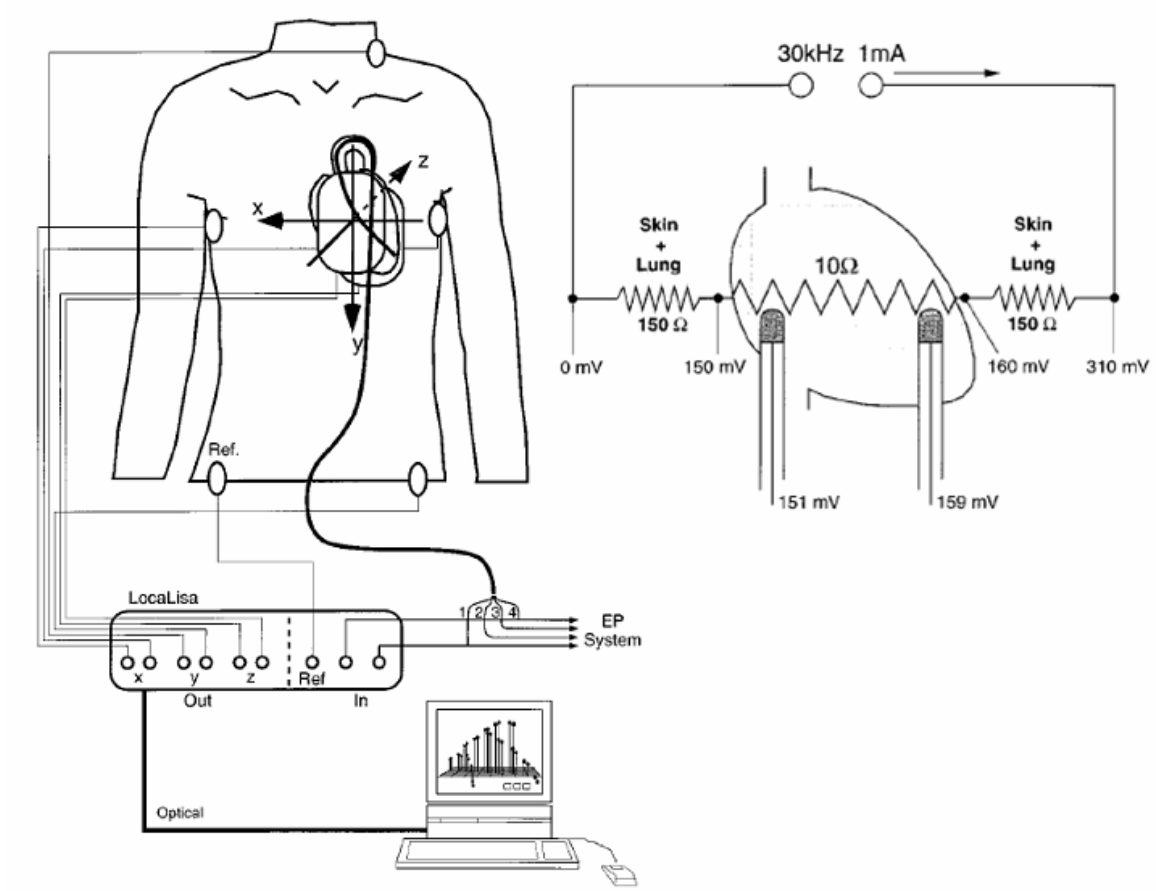

Figure 1.4. One component of the Ensite Nav X (LocaLisa) electroanatomical system. A 30 kHz current is passed between 3 pairs of skin electrodes, depicted on the left, placed orthogonally to each other. When each pair of electrodes is activated the voltage measured by an intracardiac probe at two different locations is proportional to the distance between them. In the schematic on the right a movement of the probe across the cardiac chamber is equal to a voltage drop of 8 mV. Adapted from [5].

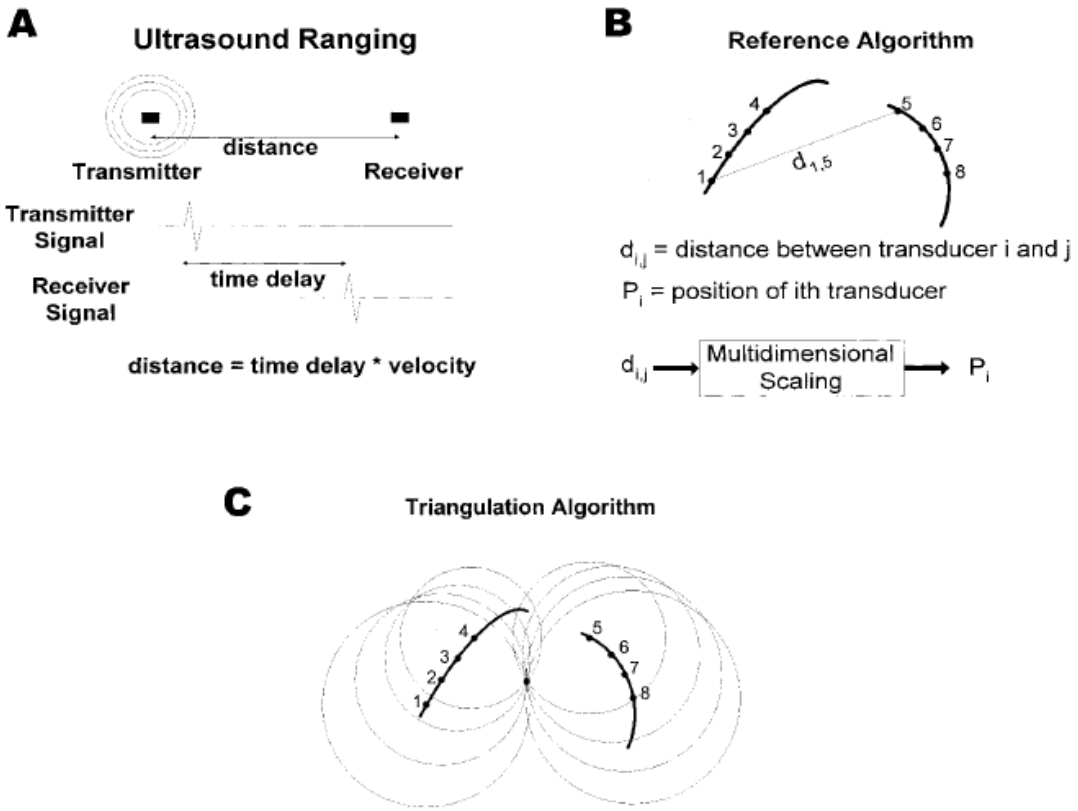

Figure 1.5. Real time Positioning System is based on ultrasound ranging. Two fixed curve catheters depicted in B have each four ultrasound transducers are used as reference for other flexible mapping catheters. The two reference catheters calibrate the position of each other as depicted in B and then they can locate through triangulation a third mapping catheter as depicted in C. Adapted from [6].

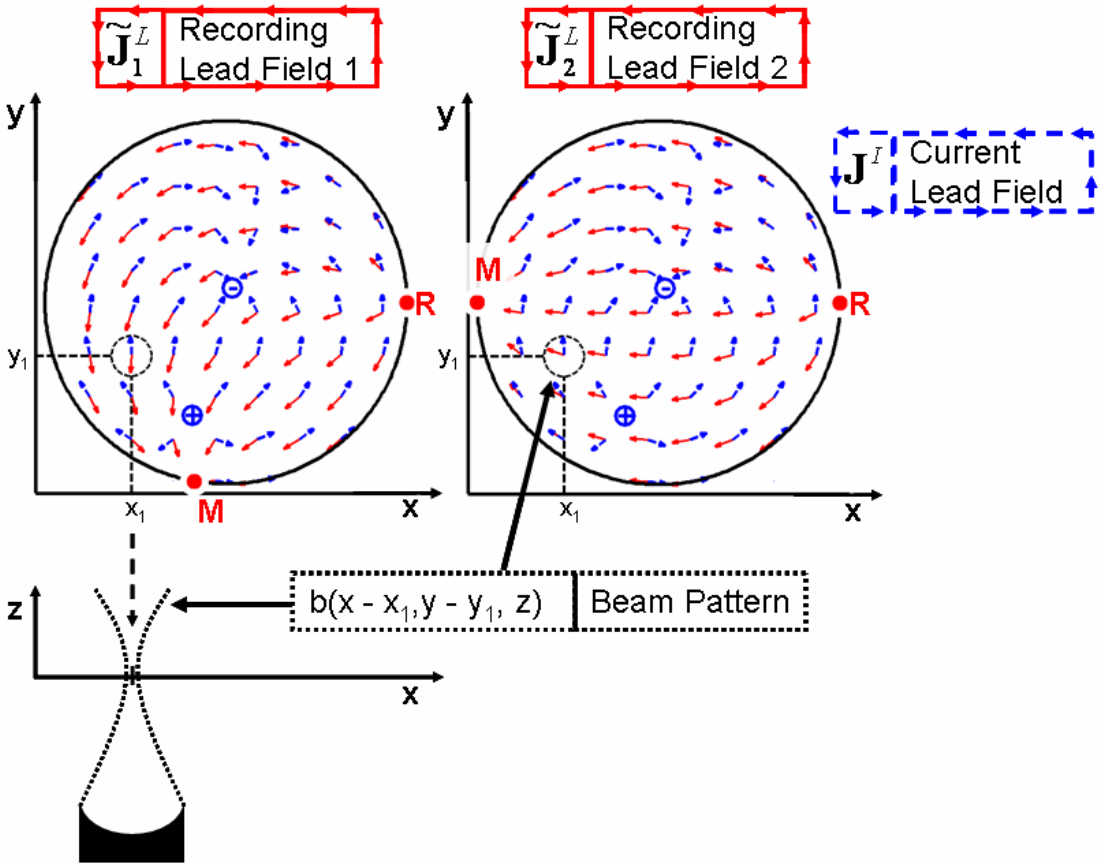

Figure 1.6. Illustration of the different factors in (1.14), the AE signal equation, as well as the sifting property of the ultrasound beam, the basis for UCSDI. The electrodes generating the unknown current distribution $\mathbf{J}^I$ are depicted as blue circles marked as "**+**" and "-". The recording electrodes are labeled R (reference) and M (mobile). Two different configurations of the recording electrodes are shown which produce two distinct recording lead fields $\tilde{\mathbf{J}}_1^L$ and $\tilde{\mathbf{J}}_2^L$. All currents in this simple example are assumed to be 2-D and limited to the x-y plane. An ultrasound transducer is focused on the x-y plane. Its beam axis is parallel to the z-axis and its beam position has been shifted to coordinates (x_1, y_1). The beam spot size is shown as a small dashed circle. As (1.15) shows, the AE voltage signal only depends on the dot product of the lead fields within the beam spot. Consequently, the beam "sifts" the distribution. Notice also that within the beam spot, $\tilde{\mathbf{J}}_1^L$ is anti-parallel to the local current field, while $\tilde{\mathbf{J}}_2^L$ is orthogonal to it. The origin of the coordinate system is at the center of the circular bath.

1.7. References

[1] R. J. Myerburg, K. M. Kessler, and A. Castellanos, "Sudden cardiac death - epidemiology, transient risk, and intervention assessment.," *Annals of Internal Medicine,* vol. 119, pp. 1187-1197, Dec 1993.

[2] J. Sra, A. Dhala, Z. Blanck, S. Deshpande, R. Cooley, and M. Akhtar, "Atrial fibrillation: Epidemiology, mechanisms, and management," *Current Problems in Cardiology,* vol. 25, pp. 413-524, Jul 2000.

[3] V. Markides and D. W. Davies, "New mapping technologies: An overview with a clinical perspective," *Journal of Interventional Cardiac Electrophysiology,* vol. 12, pp. 43-51, Aug 2005.

[4] L. Gepstein, G. Hayam, and S. A. BenHaim, "A novel method for nonfluoroscopic catheter-based electroanatomical mapping of the heart - In vitro and in vivo accuracy results," *Circulation,* vol. 95, pp. 1611-1622, Mar 1997.

[5] F. H. M. Wittkampf, E. F. D. Wever, R. Derksen, A. A. M. Wilde, H. Ramanna, R. N. W. Hauer, and E. O. R. de Medina, "LocaLisa - New technique for real-time 3-dimensional localization of regular intracardiac electrodes," *Circulation,* vol. 99, pp. 1312-1317, Mar 1999.

[6] N. M. De Groot, M. Bootsma, E. T. van der Velde, and M. J. Schalij, "Three-dimensional catheter positioning during radiofrequency ablation in patients: First application of a real-time position management system," *Journal of Cardiovascular Electrophysiology,* vol. 11, pp. 1183-1192, 2000.

[7] R. J. Schilling, N. S. Peters, and W. Davies, "Simultaneous endocardial mapping in the human left ventricle using a noncontact catheter - Comparison of contact and reconstructed electrograms during sinus rhythm," *Circulation,* vol. 98, pp. 887-898, 1998.

[8] F. Greensite, "Heart surface electrocardiographic inverse solutions," in *Modeling and imaging of bioelectrical activity : principles and applications*, B. He, Ed. New York: Kluwer Academic / Plenum Publishers, 2004, pp. 119-160.

[9] T. Berger, G. Fischer, B. Pfeifer, R. Modre, F. Hanser, T. Trieb, F. X. Roithinger, M. Stuehlinger, O. Pachinger, B. Tilg, and F. Hintringer, "Single-beat noninvasive imaging of cardiac electrophysiology of ventricular pre-excitation," *Journal of the American College of Cardiology,* vol. 48, pp. 2045-2052, Nov 21 2006.

[10] T. S. Fahmy, H. Mlcochova, O. M. Wazni, D. Patel, R. Cihak, M. Kanj, S. Beheiry, J. D. Burkhardt, T. Dresing, S. Hao, P. Tchou, J. Kautzner, R. A. Schweikert, M. Arruda, W. Saliba, and A. Natale, "Intracardiac echo-guided image integration: Optimizing strategies for registration," *Journal of Cardiovascular Electrophysiology,* vol. 18, pp. 276-282, Mar 2007.

[11] C. C. Gornick, S. W. Adler, B. Pederson, J. Hauck, J. Budd, and J. Schweitzer, "Validation of a new noncontact catheter system for electroanatomic mapping of left ventricular endocardium," *Circulation,* vol. 99, pp. 829-835, Feb 16 1999.

[12] E. K. Heist, J. Chevalier, G. Holmvang, J. P. Singh, P. T. Ellinor, D. J. Milan, A. D'Avila, T. Mela, J. N. Ruskin, and M. Mansour, "Factors affecting error in integration of electroanatomic mapping with CT and MR imaging during catheter ablation of atrial fibrillation," *Journal of Interventional Cardiac Electrophysiology,* vol. 17, pp. 21-27, Oct 2006.

[13] C. Ramanathan, R. N. Ghanem, P. Jia, K. Ryu, and Y. Rudy, "Noninvasive electrocardiographic imaging for cardiac electrophysiology and arrhythmia," *Nature Medicine,* vol. 10, pp. 422-428, Apr 2004.

[14] L. Y. Rao, R. J. He, C. X. Ding, and D. S. Khoury, "Novel noncontact catheter system for endocardial electrical and anatomical imaging," *Annals of Biomedical Engineering,* vol. 32, pp. 573-584, Apr 2004.

[15] M. Daccarett, N. M. Segerson, J. Gunther, G. Nolker, K. Gutleben, J. Brachmann, and N. F. Marrouche, "Blinded correlation study of three-dimensional electro-anatomical image integration and phased array intra-cardiac echocardiography for left atrial mapping," *Europace,* vol. 9, pp. 923-926, Oct 2007.

[16] Z. J. Malchano, P. Neuzil, R. C. Cury, G. Holmvang, J. Weichet, E. J. Schmidt, J. N. Ruskin, and V. Y. Reddy, "Integration of cardiac CT/MR imaging with three-dimensional electroanatomical mapping to guide catheter manipulation in the left atrium: Implications for catheter ablation of atrial fibrillation," *Journal of Cardiovascular Electrophysiology,* vol. 17, pp. 1221-1229, Nov 2006.

[17] J. Jossinet, B. Lavandier, and D. Cathignol, "Impedance modulation by pulsed ultrasound," *Electrical Bioimpedance Methods: Applications to Medicine and Biotechnology,* vol. 873, pp. 396-407, 1999.

[18] P. R. Malmviou J., "Chapter 19: The Basis of ECG diagnosis," in *Bioelectromagnetism: Principles and applications of bioelectric and biomagnetic fields* New York: Oxford University Press, 1995, pp. 320-335.

[19] P. R. Malmviou J., "Chapter 6: The Heart," in *Bioelectromagnetism: Principles and applications of bioelectric and biomagnetic fields* New York: Oxford University Press, 1995, pp. 148-158.

[20] P. R. Malmviou J., "Chapter 11: Theoretical Methods for Analyzing Volume Sources and Volume Conductors," in *Bioelectromagnetism: Principles and applications of bioelectric and biomagnetic fields* New York: Oxford University Press, 1995, pp. 185-226.

[21] M. O. Sweeney, "Chapter 95: Sinus Node Dysfunction," in *Cardiac Electrophysiology: From Cell to Bedside*, D. P. Zipes, Jalife J., Ed. Philidelphia, Pennsylvania: Saunders, 2004, pp. 879-883.

[22] D. Schwartzman, "Chapter 53: Atrioventricular Block and Atrioventricular Dissocation.," in *Cardiac Electrophysiology: From Cell to Bedside*, D. P. Zipes, Jalife J., Ed. Philidelphia, Pennsylvania: Saunders, 2004, pp. 485-489.

[23] W. Ellenbogen K.A., M.A., "Chapter 55: Atrial Tachycardia," in *Cardiac Electrophysiology: From Cell to Bedside*, D. P. Zipes, Jalife J., Ed. Philidelphia, Pennsylvania: Saunders, 2004, pp. 500-511.

[24] W. J. a. Z. Wu. J., D.P., "Chapter 42: Mechanism of Initiation of Venctricular Tachyarrhytmias," in *Cardiac Electrophysiology: From Cell to Bedside*, D. P. Zipes, Jalife J., Ed. Philidelphia, Pennsylvania: Saunders, 2004, pp. 380-389.

[25] K. P. Anderson, E. B. Stinson, and J. W. Mason, "Surgical exclusion of focal paroxysmal atrial tachycardia," *American Journal of Cardiology,* vol. 49, pp. 869-874, 1982.

[26] M. Haissaguerre, P. Jais, D. C. Shah, A. Takahashi, M. Hocini, G. Quiniou, S. Garrigue, A. Le Mouroux, P. Le Metayer, and J. Clementy, "Spontaneous initiation of atrial fibrillation by ectopic beats originating in the pulmonary veins," *New England Journal of Medicine,* vol. 339, pp. 659-666, Sep 1998.

[27] M. D. Lesh, G. F. Vanhare, L. M. Epstein, A. P. Fitzpatrick, M. M. Scheinman, R. J. Lee, M. A. Kwasman, H. R. Grogin, and J. C. Griffin, "Radiofrequency catheter ablation of atrial arrhythmias - results and mechanisms " *Circulation,* vol. 89, pp. 1074-1089, Mar 1994.

[28] S. M. Pogwizd and P. B. Corr, "Reentrant and nonreentrant mechanisms contribute to arrhythmogenesis during early myocardial-ischemia-results using 3-dimensional mapping. ," *Circulation Research,* vol. 61, pp. 352-371, Sep 1987.

[29] M. J. Janse, F. J. L. Vancapelle, H. Morsink, A. G. Kleber, F. Wilmsschopman, R. Cardinal, C. N. Dalnoncourt, and D. Durrer, "Flow of injury current and patterns of excitation during early ventricular arrhythmias in acute regional myocardial ischemia in insolated porcine and canine hearts-evidence of 2 different arrhythmogenic mechanisms " *Circulation Research,* vol. 47, pp. 151-165, 1980.

[30] R. Kumar and R. W. Joyner, "An experimental-model of the production of early after depolarizations by injury currentg from an ischemic region," *Pflugers Archiv-European Journal of Physiology,* vol. 428, pp. 425-432, Oct 1994.

[31] S. Markides V., O.R., Tondato F., Peters N.S., "Chapter 93: Mapping," in *Cardiac Electrophysiology: From Cell to Bedside*, D. P. Zipes, Jalife J., Ed. Philidelphia, Pennsylvania: Saunders, 2004, pp. 858-868.

[32] H. L. Estner, I. Deisenhofer, A. Luik, G. Ndrepepa, C. von Bary, B. Zrenner, and C. Schmitt, "Electrical isolation of pulmonary veins in patients with atrial fibrillation: reduction of fluoroscopy exposure and procedure duration by the use of a non-fluoroscopic navigation system (NavX (R))," *Europace,* vol. 8, pp. 583-587, Aug 2006.

[33] M. Kesek, N. Wallenius, F. Ronn, N. Hoglund, and S. Jensen, "Reduction of fluoroscopy duration in radiofrequency ablation obtained by the use of a non-fluoroscopic catheter navigation system," *Europace,* vol. 8, pp. 1027-1030, Dec 2006.

[34] P. Kovoor, M. Ricciardello, L. Collins, J. B. Uther, and D. L. Ross, "Risk to patients from radiation associated with radiofrequency ablation for supraventricular tachycardia," *Circulation,* vol. 98, pp. 1534-1540, Oct 1998.

[35] J. L. R. Smeets, S. A. Ben-Haim, L. M. Rodriguez, C. Timmermans, and H. J. J. Wellens, "New method for nonfluoroscopic endocardial mapping in humans - Accuracy assessment and first clinical results," *Circulation,* vol. 97, pp. 2426-2432, 1998.

[36] J. J. Goldberger, "Atrial fibrillation ablation: Location, location, location," *Journal of Cardiovascular Electrophysiology,* vol. 17, pp. 1271-1273, 2006.

[37] B. Taccardi, G. Arisi, E. Macchi, S. Baruffi, and S. Spaggiari, "A new intracavitary probe for detecting the site of origin of ectopic ventricular beats during one cardiac cycle.," *Circulation,* vol. 75, pp. 272-281, 1987.

[38] J. J. M. Cuppen and A. Vanoosterom, "Model studies with the inversely calculated isochrones of ventricular depolarization," *IEEE Transactions on Biomedical Engineering,* vol. 31, pp. 652-659, 1984.
[39] M. P. Nash and A. J. Pullan, "Challenges facing validation of noninvasive electrical imaging of the heart," *Annals of Noninvasive Electrocardiology,* vol. 10, pp. 73-82, 2005.
[40] J. Sra, G. Narayan, D. Krum, and M. Akhtar, "Registration of 3D computed tomographic images with interventional systems: Implications for catheter ablation of atrial fibrillation," *Journal of Interventional Cardiac Electrophysiology,* vol. 16, pp. 141-148, Sep 2006.
[41] P. A. Noseworthy, Z. J. Malchano, J. Ahmed, G. Holmvang, J. N. Ruskin, and V. Y. Reddy, "The impact of respiration on left atrial and pulmonary venous anatomy: Implications for image-guided intervention," *Heart Rhythm,* vol. 2, pp. 1173-1178, Nov 2005.
[42] J. Ector, D. Loeckx, W. Coudijzer, S. De Buck, F. Maes, S. Dymarkowski, J. Bogaert, and H. Heidbuchel, "Changes in left atrial and pulmonary venous anatomy during respiration - A 4-dimensional computed tomography-based assessment and implications for atrial fibrillation ablation," *Circulation,* vol. 115, pp. E617-E619, Jun 2007.
[43] E. Bertaglia, G. Brandolino, F. Zoppo, F. Zerbo, and P. Pascotto, "Integration of three-dimensional left atrial magnetic resonance images into a real-time electroanatomic mapping system: Validation of a registration method," *Pace-Pacing and Clinical Electrophysiology,* vol. 31, pp. 273-282, Mar 2008.
[44] P. M. Kistler, M. J. Earley, S. Harris, D. Abrams, S. Ellis, S. C. Sporton, and R. J. Schilling, "Validation of three-dimensional cardiac image integration: Use of integrated CT image into electroanatomic mapping system to perform catheter ablation of atrial fibrillation," *Journal of Cardiovascular Electrophysiology,* vol. 17, pp. 341-348, Apr 2006.
[45] H. Zhong, J. M. Lacomis, and D. Schwartzman, "On the accuracy of CartoMerge for guiding posterior left atrial ablation in man," *Heart Rhythm,* vol. 4, pp. 595-602, May 2007.
[46] R. Olafsson, R. S. Witte, K. Kim, S. Ashkenazi, and M. O'Donnell, "Electric current mapping using the acousto-electric effect - art. no. 61470O," in *Medical Imaging 2006: Ultrasonic Imaging and Signal Processing*. vol. 6147, S. Y. Emelianov and W. F. Walker, Eds., 2006, pp. O1470-O1470.
[47] R. Witte, R. Olafsson, S. W. Huang, and M. O'Donnell, "Imaging current flow in lobster nerve cord using the acoustoelectric effect," *Applied Physics Letters,* vol. 90, pp. -, Apr 16 2007.
[48] F. E. Fox, K. F. Herzfeld, and G. D. Rock, "The effect of ultrasonic waves on the conductivity of salt solutions," *Physical Review,* vol. 70, pp. 329-339, 1946.
[49] J. Jossinet, B. Lavandier, and D. Cathignol, "The phenomenology of acousto-electric interaction signals in aqueous solutions of electrolytes," *Ultrasonics,* vol. 36, pp. 607-613, Feb 1998.
[50] B. Angelsen, "Chapter 4: Waves in homogeneous tissue," in *Ultrasound Imaging: Waves Signals and Signal Processing,*. vol. I Norway: Emantec, 2000, pp. 5.1-5.97.

[51] B. Lavandier, J. Jossinet, and D. Cathignol, "Experimental measurement of the acousto-electric interaction signal in saline solution," *Ultrasonics,* vol. 38, pp. 929-936, Sep 2000.
[52] S. Finke, R. M. Gulrajani, and L. Gotman, "Conventional and reciprocal approaches to the inverse dipole localization problem of electroencephalography," *IEEE Transactions on Biomedical Engineering,* vol. 50, pp. 657-666, Jun 2003.
[53] B. He and D. S. Wu, "Imaging and visualization of 3-D cardiac electric activity," *IEEE Transactions on Information Technology in Biomedicine,* vol. 5, pp. 181-186, Sep 2001.
[54] B. Angelsen, "Chapter 5: Radiation field from a single element transducers," in *Ultrasound Imaging: Waves Signals and Signal Processing,*. vol. I Norway: Emantec, 2000, pp. 5.1-5.97.
[55] P. R. Malmviou J., "Chapter 8: Source-Field Models " in *Bioelectromagnetism: Principles and applications of bioelectric and biomagnetic fields* New York: Oxford University Press, 1995, pp. 148-158.

CHAPTER 2
VALIDATION OF ULTRASOUND CURRENT SOURCE DENSITY IMAGING

2.1. Introduction

Section 1.5 introduced Ultrasound Current Source Density Imaging (UCSDI) and its theoretical description. In this chapter a validation study of UCSDI is described as well as a new method for reconstructing current densities based on UCSDI. Both UCSDI and a conventional electrode mapped a two-dimensional (2-D) dipole current distribution generated in a thin, circular bath filled with a saline solution (0.9% NaCl). Results of these methods were compared to each other and to the results of custom simulation package. The results of UCSDI reconstruction were compared to the outcome of a conventional dipole locating inverse algorithm. An initial report on this material was given at a conference [1].

2.2. Instrumentation

2.2.1. Acousto-Electric Signal Measurement and Processing

Fig. 2.1 illustrates the experimental setup designed to generate and detect the 2-D current distribution. A low frequency sinusoidal current (arbitrarily chosen to be 500 Hz) with peak amplitude of either 28 mA or 0 mA (control) was injected through a pair of AgCl electrode wires (0.15 mm diameter), marked "+" and "-" into a 1-mm bath of 0.9% NaCl placed in a circular container (38.1 mm diameter). At low frequencies (<1 kHz),

saline and tissue are primarily resistive, and the alternating current reduces polarization at the electrode interface compared to direct current. Also, at 500 Hz the frequency of the injected current is much lower than the ultrasonic frequency of the AE signal, which can be easily filtered from the detected voltage. Stimulating AgCl electrodes were used for their electrochemical stability. The bottom of the container was a thin plastic film acting as an acoustic window. A 5-mm thick layer of mineral oil was placed on top of the saline to insulate the 2-D conductive saline layer. The mineral oil allowed the acoustic wave to pass through the saline window and minimized surface reflections at the saline interface.

Ultrasound was coupled to this container with de-ionized water (DI-H_2O). The current waveform was generated by a signal generator (33120A, Agilent, Santa Clara, CA), amplified (MDT694, Thorlabs, Newton, NJ) and AC coupled to the electrodes. The current was monitored using a multimeter (Toolkit 2707A, BK Precision, Yorba Linda, CA), as well as a differential amplifier, which measured the voltage across a 1-ohm resistor placed in series with the current injecting electrodes.

An AgCl electrode fixed at 0^o was used as the recording reference, while a mobile tungsten electrode was rotated around the boundary in 20^o steps from -60^o to 260^o (N = 17). A 7.5 MHz single element ultrasound transducer with a diameter of 1.27 cm and focal length of 5.08 cm was focused on the membrane from below, as illustrated in Fig. 2.2. The transducer was moved in a raster scan pattern in the xy-plane covering a 16 x 17 pixel grid with a step size of 2.2 mm in each direction. The current generator (33120A, Agilent) provided the master trigger for the experiment at the start of each cycle. It was fed into an Field-Programmable Gate Array (FPGA) (ezFPGA, Dallas Logic, Plano, TX), which issued a trigger to an ultrasonic pulser/receiver (5077PR, Panametrics Inc.,

Waltham, MA) and a digital acquisition board (PDA12, Signatec, Newport Beach, CA) at either the maximum or minimum of the current waveform. At each location, the transducer was pulsed 128 times on both the maximum and minimum of the current waveform. The AE signals corresponding to the positive peak were averaged, as well as those corresponding to the negative peak. The triggering diagram is shown in Fig. 2.2 to the left. The average AE signal from the positive current peak was subtracted from the AE signal of the negative peak to remove common-mode noise, such as transducer ringing.

To measure the AE signal, each electrode was connected via an analog high pass filter (single pole, 480 kHz cut off frequency) to a differential amplifier (1855A, LeCroy, Chestnut Ridge, NY) with a gain of 20 dB and bandwidth of 20 MHz. The output was further amplified by an additional 29 dB (5072PR, Panametrics Inc.). The AE signal and pulse echo were sampled concurrently at 50 MHz and digitized with 12-bit precision. All data were processed in Matlab (MathWorks Inc, Natick, MA). Signals were bandpass filtered between 1 and 3 MHz and converted to analytical form in Matlab. Since the phantom was a saline bath bounded on one side by a plastic membrane and mineral oil on the other, the conductivity profile along the beam axis was approximately rectangular. As the membrane was not perfectly flat, the timing of the pulse echo of the membrane was used to shift the AE signals to align them to the same time index. The signals must be aligned, as the correlation scheme, described below, assumes that signals are identical in shape, differing only in magnitude and sign.

To assign values to the 2-D grid, a representative AE template waveform [one with good signal to noise ratio (SNR)] was chosen and correlated with all other AE

waveforms. Under the assumption that the AE signals were perfectly aligned, the value at zero lag in the cross correlation sequence was chosen as the representative measured value at each grid point. Correlation detection was used to filter out noise spikes within the bandwidth of the AE signal. This resulted in 17 UCSD images arranged in a 16 x 17 pixel grid, one image per angle of the recording electrode. As shown below, each UCSD image was the result of the dot product of the unknown current field and the lead field of the recording electrodes. The next section explains decoupling of recording lead fields from the measured AE signal.

2.2.2. Conventional Low Frequency Mapping of the Field

The dipole current field was independently measured using conventional methods to compare results of UCSDI reconstruction and simulation. The potential distribution in the bath was mapped with a mobile tungsten electrode, mounted on a motorized 2-D translation stage and scanned across a 25 x 24 step grid in steps of $\Delta x = \Delta y = 1.5$ mm. The potential was measured with respect to a fixed reference placed on the boundary of the circle at angle 0^o using a differential amplifier (1855A LeCroy). The geometry is illustrated in Fig. 2.1 to the right. The output of the amplifier was sampled and digitized using an oscilloscope (TDS1002, Tektronix, Beaverton, OR) and transferred to a computer for storage. The magnitude and sign of the trace corresponding to each pixel were measured. In addition, boundary voltages were measured using the same instrumentation and signal processing except that the mobile electrode was rotated around the boundary of the saline bath in 32 steps of 10^o from -60^o to 250^o.

2.3. Current Source Reconstruction

2.3.1. The Forward Problem of a Single Dipole

The forward problem relevant to this method is finding the measured boundary voltage distribution produced by a point dipole current source. Rewriting (1.8) in two dimensions yields

$$V_i = \iint \rho(\widetilde{\mathbf{J}}_i^L \bullet \mathbf{J}^I)dxdy\,, \tag{2.1}$$

with $\mathbf{J}^I = \mathbf{J}^I(x,y)$, $\widetilde{\mathbf{J}}_i^L = \widetilde{\mathbf{J}}_i^L(x,y)$ and $\rho = \rho(x,y)$. A single point dipole source $\mathbf{J}_0^{\mathrm{I}}$ at location (x_1, y_1) gives

$$\mathbf{J}^I(x,y) = \mathbf{J}_0^I \delta_2(x-x_1, y-y_1)\,, \tag{2.2}$$

with δ_2(x,y) the 2-D Dirac delta function, which produces the lead voltage

$$V_i = \rho(x_1,y_1)(\widetilde{\mathbf{J}}_i^L(x_1,y_1) \bullet \mathbf{J}_0^I)\,. \tag{2.3}$$

If we have N leads, the vector of boundary voltages

$$\mathbf{V} = [V_1 \quad V_2 \quad \ldots \quad V_N]^T \tag{2.4}$$

(where $[*]^{\mathrm{T}}$ indicates transpose) is related to $\mathbf{J}_0^I$ at (x_1,y_1) by a N x 2 transfer matrix **T**

$$\mathbf{T}(x_1,y_1) = [\widetilde{\mathbf{J}}_1^L(x_1,y_1) \quad \widetilde{\mathbf{J}}_2^L(x_1,y_1) \quad \cdots \quad \widetilde{\mathbf{J}}_N^L(x_1,y_1)]^T \tag{2.5}$$

by

$$\mathbf{V} = \rho(x_1,y_1)\mathbf{T}(x_1,y_1)\mathbf{J}_0^I\,. \tag{2.6}$$

Equation (2.6) is the solution to the forward problem. That is, the relationship between the source $\mathbf{J}_0^{\mathrm{I}}$ and the boundary voltage is determined [2]. Some inverse algorithms solve this forward problem for all points (x,y) and calculate the normalized sum squared error (NSSE) between the measured and estimated boundary voltage distribution for each point. The normalization factor is the maximum error. The algorithm

ranks the pixels in terms of likelihood (1- NSSE). The pixel likeliest to contain the dipole is the one that minimizes the sum of squares error between the measured and calculated boundary voltage distribution [2]. We compare this algorithm with USCDI.

2.3.2. UCSDI Reconstruction

To derive the reconstruction algorithm, the signal equation (1.14) is rewritten and simplified. In the special case of an infinite saline film of thickness *h* and uniform resistivity ρ', the 3-D resistivity distribution is

$$\rho(z) = \rho'(u(z) - u(z-h)), \tag{2.7}$$

where *u(z)* is the step function. We further assume that the thickness *h* is small enough such that the recording lead field $\tilde{\mathbf{J}}^L$ and unknown current field $\mathbf{J}^I$ are primarily 2-D and the beam pattern *b*(x,y,z) has a constant cross section across the thickness of the bath

$$b(x,y,z) = b(x,y), \;\; 0 \le z \le h. \tag{2.8}$$

With the ultrasound focus at (x_1, y_1), the voltage measured between the fixed reference and the mobile electrode at angle $\theta_i = i\,\Delta\theta$, i=1,..,N is

$$V_i^{AE}(x_1,y_1,t) = -K_I P_0 \rho' \underbrace{\iint \left(\tilde{\mathbf{J}}_i^L(x,y) \bullet \mathbf{J}^I(x,y)\right) b(x-x_1, y-y_1)\,dxdy}_{A} \underbrace{\int_0^h a\left(t - \frac{z}{c}\right) dz}_{B}. \tag{2.9}$$

Based on these assumptions, *A* and *B* in (2.9) are convolutions. In convolution *A*, *b*(x,y) sifts out the value of the dot product at (x_1,y_1), whereas *B* describes the generation of the high frequency component of the signal as the acoustic pulse traverses the saline bath.

For the development of the algorithm, we assume the beam is narrow, that is,

$$b(x,y) \approx b_0 \delta_2(x,y). \tag{2.10}$$

By defining

$$A(t) = \int_0^h a\left(t - \frac{z}{c}\right) dz \text{ and } K_a = -K_I P_0 \rho' b_0, \tag{2.11}$$

(2.9) becomes

$$V_i^{AE}(x_1, y_1, t) \approx K_a \left(\tilde{\mathbf{J}}_i^L(x_1, y_1) \bullet \mathbf{J}^I(x_1, y_1)\right) A(t). \tag{2.12}$$

From (2.12), it is clear that the exact time point of *A(t)* does not affect the reconstruction, so for the sake of argument we choose here the maximum, $A_0 = \max\{A(t)\}$.

$$V_i^{AE}(x_1, y_1) \approx K_a A_0 \left(\tilde{\mathbf{J}}_i^L(x_1, y_1) \bullet \mathbf{J}^I(x_1, y_1)\right). \tag{2.13}$$

Now, (2.13) has the same form as (2.6) except that the boundary voltage V_i^{AE} is also a function of space. Dropping the superscript on V_i^{AE}, (2.13) becomes

$$\mathbf{V}(x_1, y_1) \approx K_a A_0 \mathbf{T}(x_1, y_1) \mathbf{J}^I(x_1, y_1). \tag{2.14}$$

The minimum norm estimate of the dipole, $\mathbf{J}^I(x_1, y_1)$, given $\mathbf{V}(x_1, y_1)$ is

$$\mathbf{J}^I(x_1, y_1) = \frac{1}{K_a A_0} (\mathbf{T}(x_1, y_1))^+ \mathbf{V}(x_1, y_1), \tag{2.15}$$

where $(*)^+$ denotes a Moore-Penrose pseudo inverse (i.e., $T^+ = (T^T T)^{-1} T^T$) [2].

2.3.3. Simulation of Lead Fields and Current Distribution

All lead fields ($\tilde{\mathbf{J}}_i^L$ and $\mathbf{J}^I$) were computed using a 2-D *QuasiStaticSmallCurrents* simulation in Femlab (Comsol AB, Stockholm, Sweden). These fields were simulated to calculate the transfer matrices **T**(x,y) in (2.15) and verify the measurements and

reconstructions in two steps. First, simulations were compared to conventional low frequency measurements and, second, actual UCSDI reconstructions were compared with simulations.

The bath was modeled as a circular base domain (diameter = 38.1 mm) with the electrodes modeled as two 0.2-mm diameter circular inner boundaries of the base domain. Each lead field was simulated separately such that there were three boundaries: one exterior and two interior. Boundary conditions prevented flow across the exterior boundary, while assuring inward flow at one interior boundary and outward flow at the other. To simulate the recording lead field the positions of the recording electrodes were identical to the experimental setup. For the simulations, the injected current lead field (cathode) was placed at (x,y) = (-1.7, -10.8) mm, while the anode was placed at (x,y) = (0.7, -5.3) mm, based on their actual positions during the experiment.

To determine the transfer coefficients, the lead fields $\tilde{\mathbf{J}}_i^L(x_1, y_1)$ were calculated for each angle on the same 16 x 17 pixel grid used in the experiment. The AE data were simulated by calculating the lead fields and the current distribution $\mathbf{J}^I(x, y)$ on a high density 241 x 257 grid with $\Delta x = \Delta y = 0.137$ mm and then calculating their dot product. From (2.9), the AE signal measures the dot product $\tilde{\mathbf{J}}_i^L(x_1, y_1) \bullet \mathbf{J}^I(x_1, y_1)$ with low pass filtering by the ultrasound beam. Therefore, to simulate the effect of the ultrasound beam pattern, a Gaussian filter with a 3-mm diameter at -3dB was applied to the high density dot product data. The result was then downsampled to the same 16 x 17 pixel grid used in the experiment. For the low frequency simulation, this upsampling/downsampling was not used, and no filtering was applied. The potential distribution was simulated and

sampled on a 25 x 24 grid with 1.5- mm step size. The low frequency boundary voltage was sampled at 10^o intervals, along the boundary of the domain.

2.3.4. Processing of Reconstructed Images

The measured and simulated reconstructed vector fields were smoothed with a 2-D Gaussian filter (-3dB = 1.5 mm) and interpolated to a 300x300 grid. The source density of the current field I_{CSD} was calculated by taking the divergence of the interpolated data [3]:

$$\nabla \bullet \mathbf{J}^I(x,y) = -I_{csd}(x,y) \ . \tag{2.16}$$

2.4. Results

Both UCSDI and low frequency measurements agreed well with simulation. The 2-D current field was successfully reconstructed by UCSDI with the current source and sink located to within 1 mm of their actual locations.

A map of the potential distribution measured with conventional methods is contrasted with the simulated field in Fig. 2.3. Current injecting electrodes extending above the saline bath prevented the entire region to be mapped, as illustrated in Fig. 2.1. Nonetheless, the correlation coefficient between measured data and the simulated distribution for the remaining pixels (88% of total) was 0.996.

A comparison between boundary voltage measurements and simulations is shown in Fig. 2.4. Measurement closely matched simulation with a correlation coefficient of 0.999. The position of the stimulating electrodes prevented measurements between $\Theta = 260^o$ and 300^o. Fig. 2.5 presents a typical high frequency trace at a single pixel location and single

lead (Θ=260^o). The relevant experimental geometry is shown on the right. The resistivity profile along the beam axis was rectangular. The polarity of the AE signal follows the sign of current injection (plot 2.5B). Plot 2.5C denotes the subtraction of the "-" trace in 2.5B from the "+" trace, eliminating common-mode noise. Note that the AE signal is shifted down in frequency to approximately 2 MHz from the incoming acoustic pulse. This is consistent with convolution *B* in equation (2.9) stating that the AE signal is a convolution between the acoustic pulse and an averaging (low pass) filter with a rectangular shaped impulse response.

Fig. 2.6 shows an example of a detected UCSD image for a single angle (Θ=260^o). It corresponds to (2.13). Even for a single lead of two electrodes, the location of the source is highly resolved. There were 16 other similar UCSD images--one for each position of the mobile electrode. All 17 UCSD images were used to reconstruct the current density as described by (2.14) and (2.15). The results of the reconstruction are displayed in Fig. 2.7 (left). Reconstruction based on experimental results (top row) is consistent with simulated reconstructions (bottom row). The x and y component of the current density, as well as the divergence, are also shown in Fig. 2.7. Results using a conventional inverse algorithm (i.e., the likelihood as a function of space) are illustrated to the far right [2]. This conventional algorithm, described at the end of Section 2.3.1, finds the most likely location of a single dipole given the boundary voltage distribution displayed in Fig. 2.4.

The divergence of the current density is related to the current source density by (2.16). Reconstructions were quantified by locating the current sources and sinks based on the extrema of the divergence distribution of the simulated and measured data. The estimated and actual positions are summarized in table 2.1. Simulations agreed well with

UCSDI and low frequency measurements. The reconstructed current field by UCSDI located the current source and sink to within 1 mm of the actual locations. Note that in this case the full-width-half-maximum (FWHM) values of UCSDI were dominated by the lateral dimensions of the -3dB focal spot of the ultrasound transducer, which was approximately 3 mm, based on its f number (f/#=4) and the center frequency of the AE signal (2 MHz).

2.5. Discussion

We have described UCSDI, a new method to map current densities based on the AE effect with improved spatial resolution. In this initial study under controlled conditions, UCSDI accurately located a 2-D current source to within 1 mm of its actual position, without making prior assumptions about the nature of the source, other than the resistivity distribution. The accuracy was within one sampling interval of the grid step size (2.2 mm).

The spatial resolution of UCSDI according to the simplified AE signal equation (2.9) is dominated by the ultrasound beam, due to its sifting property in UCSDI. The thin current injecting electrodes (diameter = 0.2 mm) can be considered point sources. The average FWHM of 4-mm for both simulated and measured data was consistent with the beamwidth of the transducer (3 mm) and the applied smoothing filter. The lateral resolution can be improved by choosing a transducer with a tighter focus than the f/4 used for this study. The beam spot size of a narrow band transducer is roughly equal to the product of the wavelength and f/number, where f/number is the ratio of the transducer's focal length to its diameter. For example, a tightly focused transducer with

f/1 at the same frequency would have a -3dB focal diameter of approximately 0.75 mm [4].

The conventional inverse algorithm produced the broad likelihood distribution shown in Fig. 2.7 (FWHM = 15 mm). The chosen inverse method represents the best-case scenario for conventional algorithms. The dipole source geometry dovetails with the explicit single-dipole assumption, and the algorithm uses multiple measurements with high SNR. In contrast, our method directly resolves the location of the dipole's source and sink with only the assumption of the resistivity distribution, (in this case, homogenous) which is a necessary assumption of most inverse algorithms. Furthermore, in Fig. 2.7 a map of the entire 2-D current field is illustrated as an image of the x and y-components of the field. Direct estimates of the current field would not normally be possible using conventional electrical mapping methods.

Although we demonstrate that UCSDI reconstructs both the magnitude and direction of the current from a synthetic array of 18 electrodes, as few as *two* electrodes provide detailed information on the actual location of the current dipole (Fig. 2.6). Conventional dipole localization would require a large number of electrodes to approach similar results, as Fig. 2.7 demonstrates.

Although these initial results are promising, the approach has limitations. The small AE signal must be conditioned appropriately (filtering, etc), such as that shown in Fig. 2.5. The effect of the small signal can be seen in the noise ripples in the upper left quadrant of the detected UCSD image in Fig. 2.6. This affected the reconstruction of $\mathbf{J}_X$ and $\mathbf{J}_Y$ as illustrated in Fig. 2.7. However, the SNR of the reconstructed image was still

sufficient to accurately estimate the current source and sinks to within 1 mm. Further investigations will be aimed at increasing signal size, while reducing sources of noise.

In this work, a simple 2-D current system was used, for the sake of clarity, to directly compare UCSDI with other methods for mapping biopotentials. However, it is clear from the AE signal equation (1.14) that this method can be extended to three dimensions and more complicated source geometries. Reconstruction using three dimensions will probably be not as straightforward as in the 2-D case for which (1.14) could be separated into two factors in (2.9), one that depends only on x and y and the other on z. In a 3-D reconstruction, the dependence of the beam pattern b(x,y,z) on z needs to be taken into account. If the ultrasound transducer and electrode array are fixed in position with respect to each other, a known electrical source can be used to self-calibrate the system.

Although this Chapter focuses on applications of UCSDI to electrocardiography, the technique could also be used for current density analysis in the exposed brain or other neural structures. If this technique were applied to intracardiac electrocardiography, it could potentially generate 3-D current maps of the cardiac activation wave with high spatial resolution. High frame rate UCSDI is possible via electronic ultrasound beam steering. Although existing catheters that integrate electrodes with ultrasound are limited to 2-D imaging, technology exists to steer 60^{o}x60^{o} sectors in 3-D, which might be used to generate 3-D images of current flow co-registered with pulse-echo images illustrating structure [5-7]. The relative motion of the catheter might not be a significant problem, since the heart is quasi-stationary during the spread of the activation wave. Motion-

compensation algorithms could be used to reduce artifacts associated with heart motion [8].

USCDI has unique advantages over other methods because there is no registration error between anatomical images and maps of electrical activity. This is superior to conventional inverse localization methods that use pre-surgical CT or MRI images for anatomical mapping fused with an electroanatomical map for catheter guidance. MRI and CT provide pre-surgical, static images of the heart and typically provide no functional information. Registration error between the CT/MRI images and the electro-anatomical map has been reported to be in the range of 2-10 mm [9-12]. Preliminary studies have shown that a combined electrode and ultrasound catheter can be used for anatomical mapping and guidance [6, 7]. If such a device is made compatible for UCSDI, pulse-echo ultrasound images showing myocardial anatomy and kinematics can be simultaneously integrated with electrical mapping. Such automatic real-time co-registration is currently not found in typical cardiac imaging and would dramatically facilitate guidance during corrective heart surgery.

Table 2.1. Location estimates of current source and sink. Actual locations refer to independent measurements of the positions of the current-injecting electrodes. The FWHM is defined as twice the mean distance from a given extrema of the divergence to the half maximum contour. FWHM = Full Width at Half Maximum

Current Source/Sink	Name	x [mm]	y [mm]	FWHM [mm]
Source	Simulated AE	-2.2	-10.3	3.8
Source	Measured AE	-2.3	-10.3	3.8
Source	Actual	-1.7	-10.8	
Sink	Simulated AE	0.3	-5.4	3.8
Sink	Measured AE	-0.05	-3.7	4.2
Sink	Actual	0.7	-5.3	

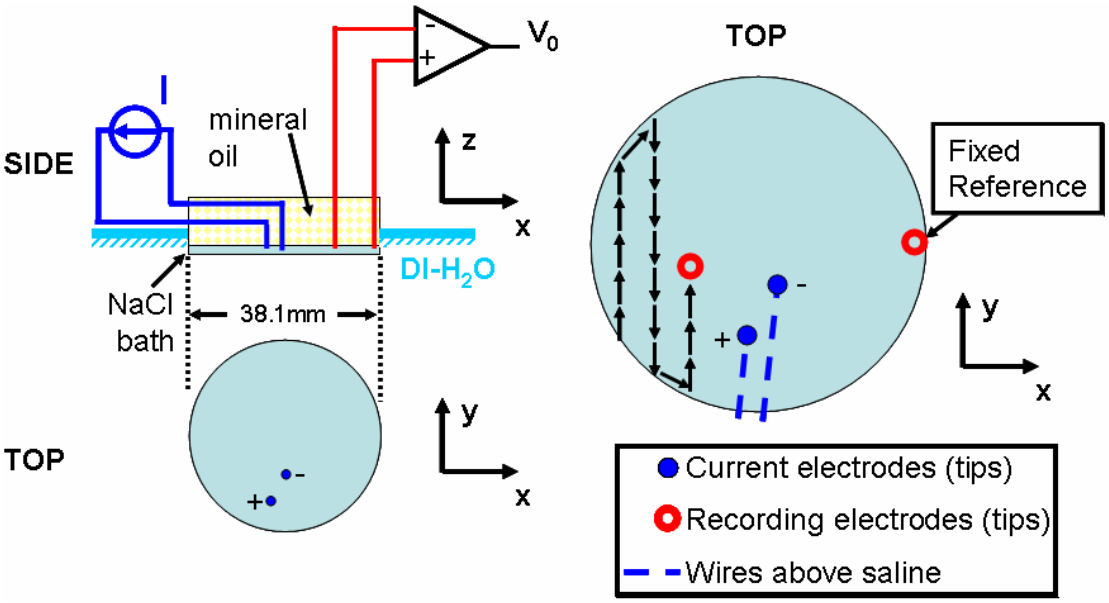

Figure. 2.1. Experimental setup for conventional low frequency measurement. A current distribution was generated by injecting current I through two AgCl electrodes "+" and "-" into a 1-mm thick 0.9% NaCl saline bath. The bath was in a circular container with a 38.1 mm inner diameter. The potential V_0 was measured between a fixed reference AgCl electrode and a mobile tungsten electrode. The tungsten electrode was moved in discrete steps across the entire bath to map the potential distribution. The presence of current injection wires above the saline prevented complete mapping of the potential distribution close to these wires. The origin of the coordinate system is at the center of the circular bath.

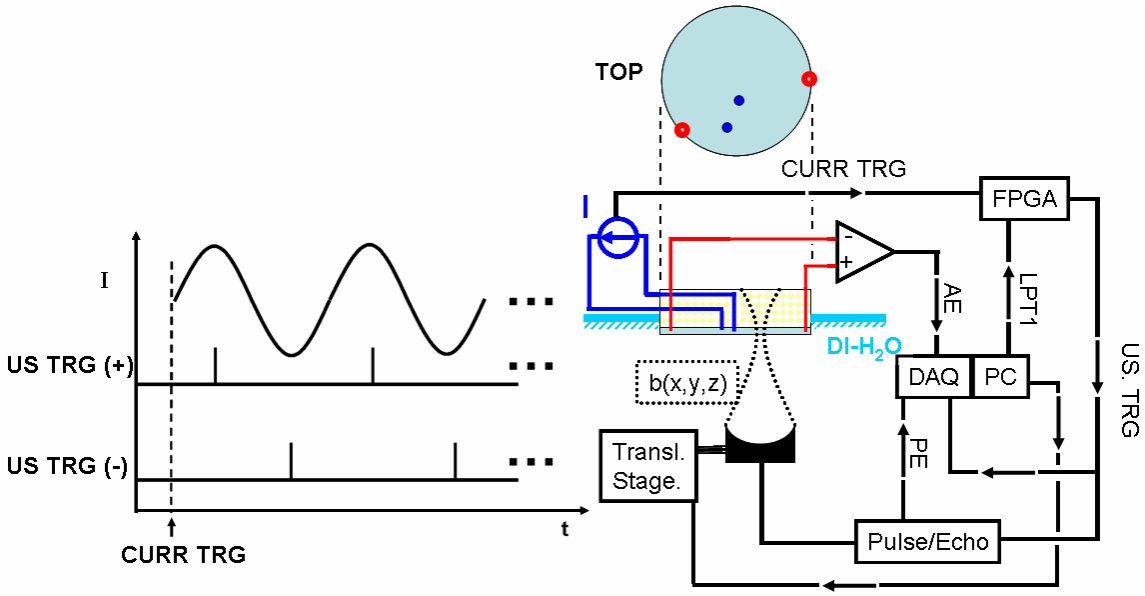

Figure. 2.2. Right: Experimental setup for the AE measurement. Left: Experimental timing. The current waveform I(t) was generated using an Agilent 33120A. Its sync output (CURR TRG) was fed into an FPGA which sent a trigger (US TRG) to the pulse-receiver and data acquisition board (DAQ). The AE and pulse-echo signals were acquired after each US TRG. The FPGA triggered the ultrasound transducer on either the positive or negative peak of the current waveform. The top view of the bath and the layout of the electrodes is shown on top.

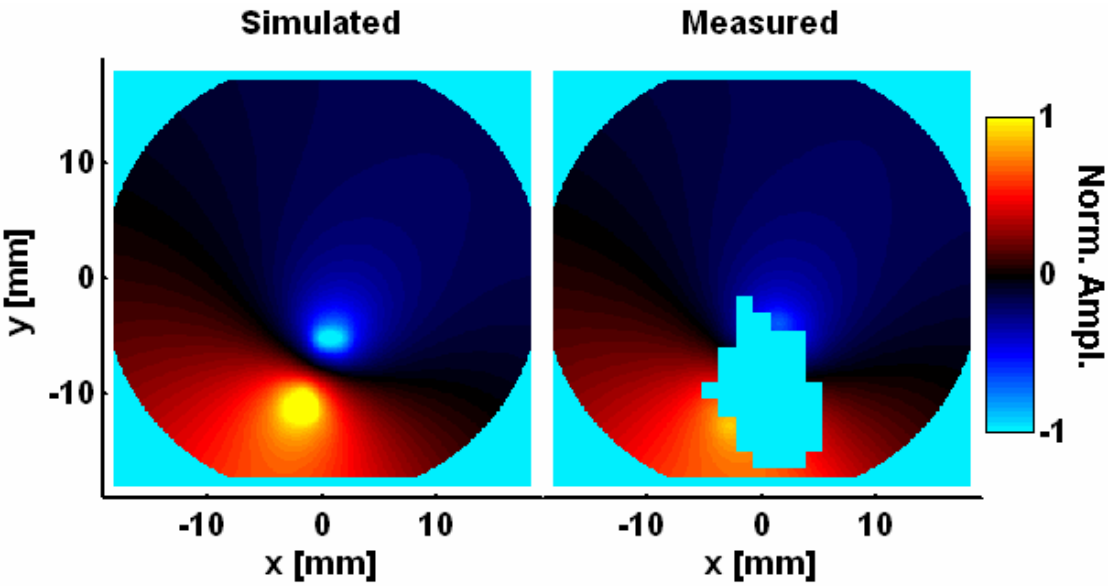

Figure. 2.3. Left: A simulation of the potential distribution generated by the current injected into the bath. Right: The potential distribution measured directly between the roving tungsten electrode and the fixed AgCl reference electrode. The presence of the current injecting wires over the bath (illustrated in Fig. 2.1) precluded the mapping of the field close to the electrodes. The color scale is linear. Pixel dimensions for all plots are 127 x 127 μm^2.

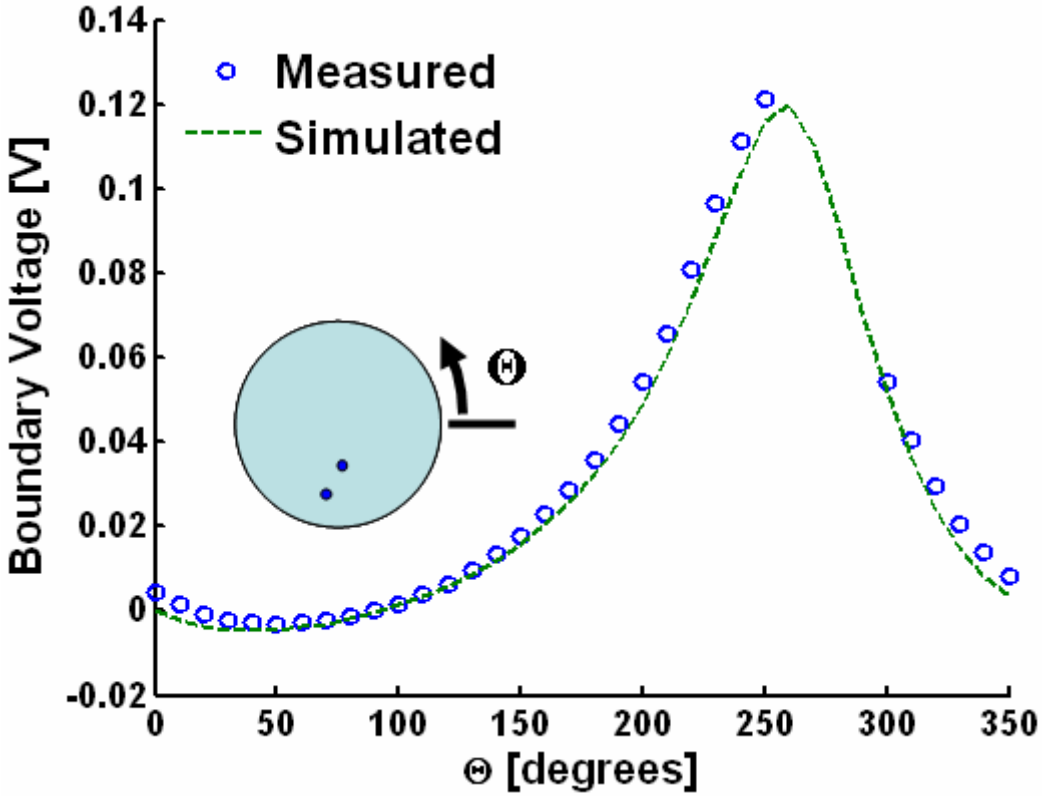

Figure. 2.4. Conventional measurement (open blue circles) and simulation (dashed green line) of the potential distribution at the boundary of the bath generated by the current injected through the stimulation electrodes. Θ is the location at the boundary of the roving tungsten electrode. The inset illustrates the measurement geometry. The current-injecting wires over the bath (illustrated in Fig. 2.1) prevented measurement between $\Theta = 260^{o}$-300^{o}.

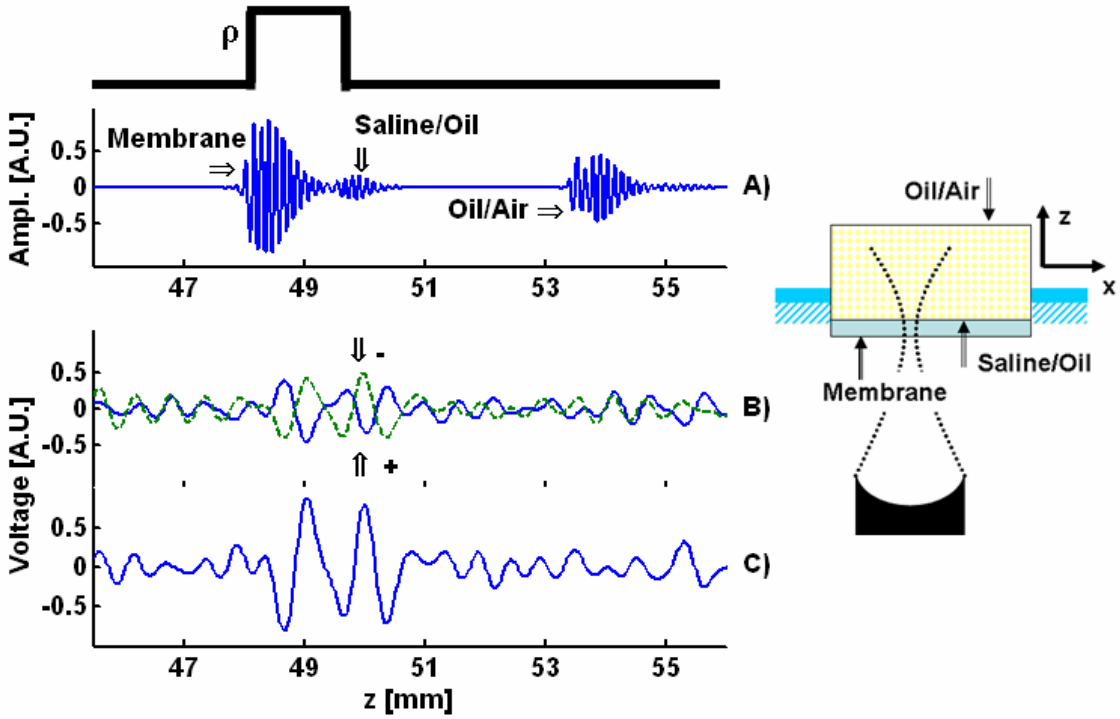

Figure 2.5. Sample traces for a single pixel of a single lead. Geometry is illustrated on the right. Trace A) is the pulse echo with the echoes from different features in the picture to the right. Trace B) has two AE traces, one captured when ultrasound is triggered on the positive peak of the current waveform (+) and the other when ultrasound is triggered on the negative peak (-). As expected the "+" waveform is 180^{o} out of phase with the "-" waveform. Trace C) is the subtraction of the "-" waveform from the "+" waveform to minimize common-mode interference. On top is illustrated graphically the rectangular resistivity distribution along the z-axis.

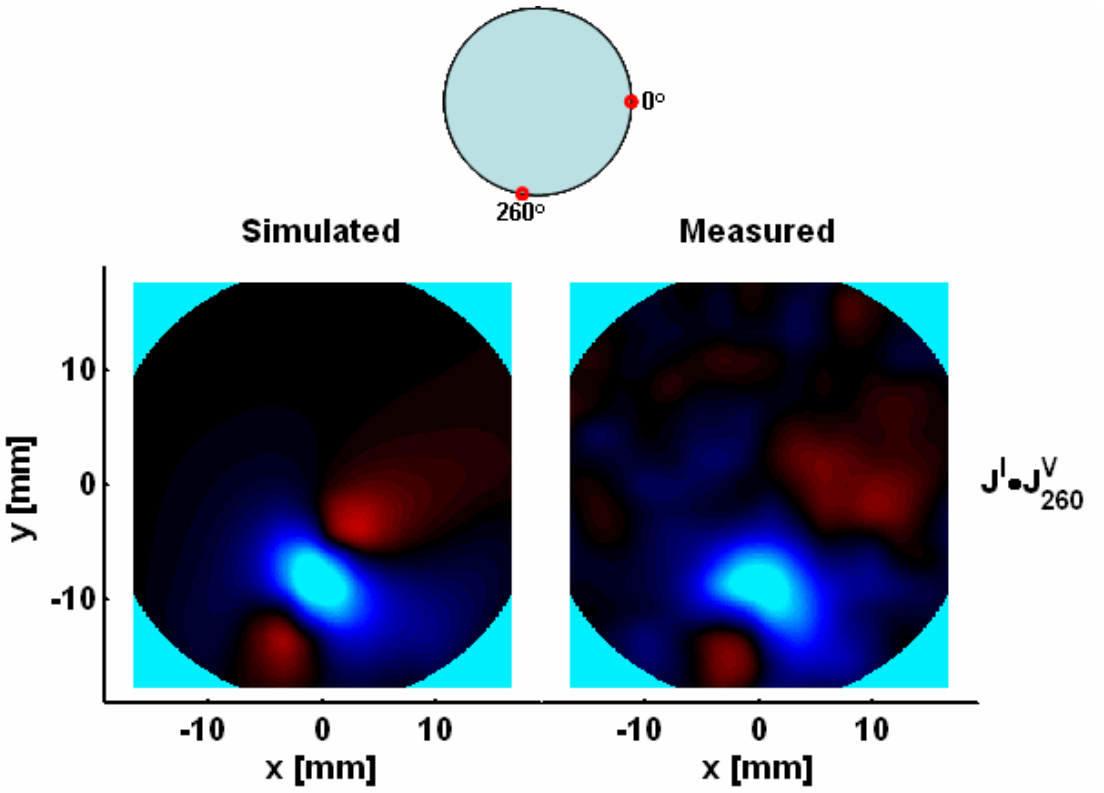

Figure 2.6. UCSDI for a single lead when the roving electrode is at Θ = 260°, while the reference electrode is still at Θ = 0°, as illustrated with the cartoon above and center. The figure on the right is the actual measurement, while the figure on the left is the theoretical prediction.

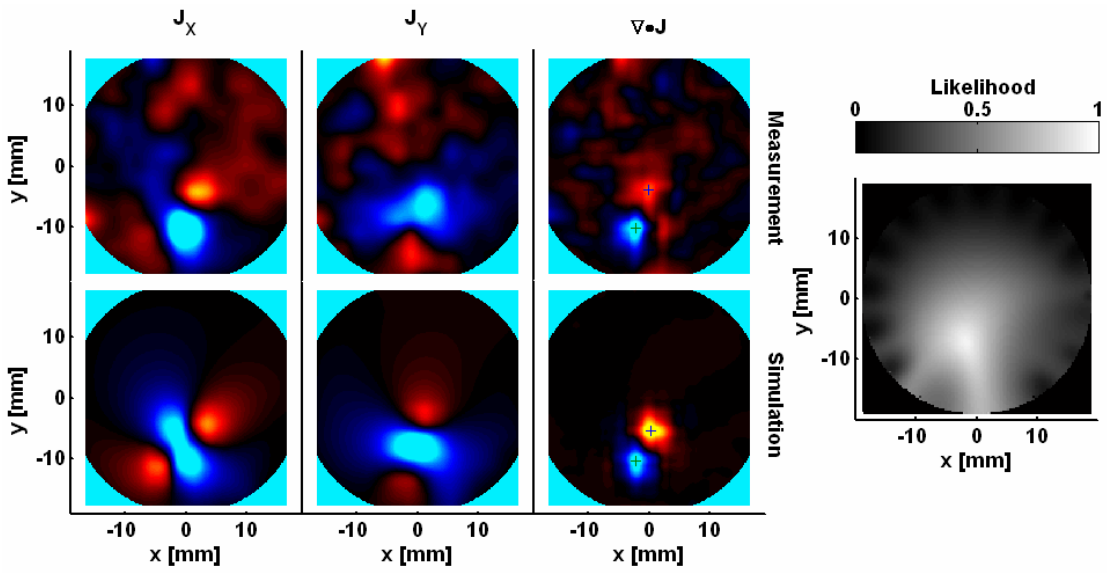

Figure 2.7. Left*:* Reconstruction results for both measured (top row) and simulated (bottom row) data. The left, middle, and right columns correspond to the x-component, y-component, and divergence of the current density, respectively. The "+" signs illustrate extrema positions. Right*:* Results of a conventional algorithm that finds the most likely position of a single dipole given the low frequency boundary voltage distribution shown in Fig. 2.4.

2.6. References

[1] R. Olafsson, R. S. Witte, and M. O'Donnell, "Measurement of a 2D electric dipole field using the acousto-electric effect - art. no. 65130S," in *Medical Imaging 2007: Ultrasonic Imaging and Signal Processing*. vol. 6513, S. Y. Emelianov and S. A. McAleavey, Eds., 2007, pp. S5130-S5130.

[2] S. Finke, R. M. Gulrajani, and L. Gotman, "Conventional and reciprocal approaches to the inverse dipole localization problem of electroencephalography," *IEEE Transactions on Biomedical Engineering,* vol. 50, pp. 657-666, Jun 2003.

[3] N. N. Rao, "Fundamentals of engineering electromagnetics revisited," in *Fundamentals of engineering electromagnetics*, R. Bansal, Ed. Boca Raton, FL: CRC/Taylor & Francis, 2006, pp. 1-53.

[4] B. Angelsen, "Chapter 5: Radiation field from a single element transducers," in *Ultrasound Imaging: Waves Signals and Signal Processing,*. vol. I Norway: Emantec, 2000, pp. 5.1-5.97.

[5] W. Lee, S. F. Idriss, P. D. Wolf, and S. W. Smith, "A miniaturized catheter 2-D array for real-time, 3-D intracardiac echo cardiography," *IEEE Transactions on Ultrasonics Ferroelectrics and Frequency Control,* vol. 51, pp. 1334-1346, Oct 2004.

[6] L. Y. Rao, R. J. He, C. X. Ding, and D. S. Khoury, "Novel noncontact catheter system for endocardial electrical and anatomical imaging," *Annals of Biomedical Engineering,* vol. 32, pp. 573-584, Apr 2004.

[7] D. N. Stephens, J. Cannata, R. Liu, K. K. Shung, O. Oralkan, A. Nikoozadeh, P. Khuri-Yakub, H. Nguyen, R. Chia, A. Dentinger, D. Wildes, K. E. Thomenius, A. Mahajan, K. Shivkumar, K. Kim, M. O'Donnell, and a. D. J. Sahn, "Forward looking intracardiac imaging catheters for electrophysiology," in *2006 IEEE Ultrasonics Symposium*. vol. 06CH37777C Vancouver, BC, Canada, 2006, pp. 702-705.

[8] Y. Shi, F. J. de Ana, S. J. Chetcuti, and M. O'Donnell, "Motion artifact reduction for IVUS-based thermal strain imaging," *IEEE Transactions on Ultrasonics Ferroelectrics and Frequency Control,* vol. 52, pp. 1312-1319, Aug 2005.

[9] T. S. Fahmy, H. Mlcochova, O. M. Wazni, D. Patel, R. Cihak, M. Kanj, S. Beheiry, J. D. Burkhardt, T. Dresing, S. Hao, P. Tchou, J. Kautzner, R. A. Schweikert, M. Arruda, W. Saliba, and A. Natale, "Intracardiac echo-guided image integration: Optimizing strategies for registration," *Journal of Cardiovascular Electrophysiology,* vol. 18, pp. 276-282, Mar 2007.

[10] E. K. Heist, J. Chevalier, G. Holmvang, J. P. Singh, P. T. Ellinor, D. J. Milan, A. D'Avila, T. Mela, J. N. Ruskin, and M. Mansour, "Factors affecting error in integration of electroanatomic mapping with CT and MR imaging during catheter ablation of atrial fibrillation," *Journal of Interventional Cardiac Electrophysiology,* vol. 17, pp. 21-27, Oct 2006.

[11] P. M. Kistler, K. Rajappan, M. Jahngir, M. J. Earley, S. Harris, D. Abrams, D. Gupta, R. Liew, S. Ellis, S. C. Sporton, and R. J. Schilling, "The impact of CT image integration into an electroanatomic mapping system on clinical outcomes

of catheter ablation of atrial fibrillation," *Journal of Cardiovascular Electrophysiology,* vol. 17, pp. 1093-1101, Oct 2006.

[12] V. Y. Reddy, Z. J. Malchano, G. Holmvang, E. J. Schmidt, A. d'Avila, C. Houghtaling, R. C. Chan, and J. N. Ruskin, "Integration of cardiac magnetic resonance imaging with three-dimensional electroanatomic mapping to guide left ventricular catheter manipulation - Feasibility in a porcine model of healed myocardial infarction," *Journal of the American College of Cardiology,* vol. 44, pp. 2202-2213, Dec 7 2004.

CHAPTER 3
CARDIAC ACTIVATION MAPPING USING UCSDI

3.1. Introduction

Chapter 2 described the validation of UCSDI by mapping an artificially generated two-dimensional current distribution using UCSDI. In previous *in vitro* experiments UCSDI has been shown to have sufficient sensitivity to detect and map biological currents [1-3]. In this chapter, the first application of UCSDI for mapping cardiac activation currents in an isolated rabbit heart will be described.

The heart was perfused with an excitation-contraction decoupler to reduce motion while retaining electrical function. This reduced the risk of motion artifacts and facilitated analysis of results. The heart was alternatively paced from the apex and the right atrium while AE and ECG were collected simultaneously from tungsten electrodes embedded in the left ventricle. A focused 540 kHz transducer, scanned across the heart from apex to base, was used as the ultrasound modulation source. The spatial pattern of UCSDI was compared to the disposition of the electrodes and its timing to ECG. Preliminary results from this study were presented at a conference [4].

3.2. Methods

3.2.1. Langendorff Isolated Rabbit Heart Setup

Two hearts were excised from white New Zealand rabbits. They were used in separate experiments and will be referred to as hearts A and B. Each was placed in a Langendorff setup and retroperfused through the aorta with a modified Kreps-Henseleit (K-H) buffer (In mM: NaCl 117, KCl 4, $MgCl_2$ 1.2, KH_2PO_4 1.1, glucose 5, $NaHCO_3$ 25, $CaCl_2$ 2.6, pH 7.44, 37^0C) oxygenated with a mix of 95% O_2 and 5% CO_2 [5]. To eliminate motion artifacts, 15 mM of an excitation-contraction decoupler (2,3-butane dione monoxime (BDM)) was mixed into the K-H buffer. BDM reduces mechanical contraction, yet preserves the electrical cardiac wave [6]. All protocols were approved by the University Committee on the Use and Care of Animals at the University of Michigan.

3.2.2. Instrumentation

The experimental geometry is shown in Fig. 3.1. Each heart was placed in a small tank inside a larger outer tank. The outer tank was filled with de-ionized water and a single element 540 kHz f/1 ultrasound transducer with 90 mm focal length (Etalon, Indianapolis, IN) was placed in the water underneath the small tank. The heart was placed in a custom made holder in the inner tank such that the long axis of the heart was horizontal and the left ventricle facing down. In Fig. 3.1 the long axis of the heart coincides with the x-axis of the imaging coordinate system.

Eight teflon coated tungsten electrodes were inserted into the heart, four recording electrodes (1, 2, 3, 4) and four stimulating electrodes (S1, S2, S3, S4). The tip of each electrode was stripped and bent into a hook such that the electrode, once inserted, would

have better purchase. One pair of stimulating electrodes (S1, S2) were inserted 1 mm part into the apex of the heart while the other (S3, S4) were inserted 2 mm apart into the right atrium. The recording electrodes were inserted into the left ventricle in a row approximately parallel to the long axis of the heart. The electrodes were placed sequentially such that 1 was closest to the apex of the heart while 4 was closest to the base of the heart. The spacing between electrode pairs 1-2, 2-3 and 3-4 was 4, 6 and 3 mm in heart A and 3, 4, 3 mm in heart B as measured after the conclusion of the experiment. A large ground electrode was placed beside the heart in the small tank.

The pacing signal was a 5V high and 500 μs wide rectangular pulse emitted by a function generator (33120, Agilent, Santa Clara CA). The heart was paced either from the apex (with electrodes S1 and S2) or from the right atrium (with electrodes S3 and S4).

Each recording electrode was connected to a low frequency amplifier with a gain of 100 and bandwidth 0.1 Hz to 3000 Hz. Each amplifier measured the voltage between the corresponding electrode and the ground electrode. Electrodes 1 and 2 were connected to an AM502 differential amplifier (Tektronix, Beaverton, OR), while electrodes 3 and 4 were connected to a SRS560 differential amplifier (Stanford Research Systems, Sunnyvale, CA). These amplifiers recorded the normal low frequency electrocardiograms (ECG) corresponding to V_i^{LF} in (1.12) and their outputs were connected to two digital oscilloscopes (TDS1002, Tektronix). The oscilloscopes digitized the signals and sent them via General-Purpose-Interface-Bus (GPIB) to the computer. The sync output of the stimulation function generator was used to trigger data acquisition.

To measure the high frequency AE signal (corresponding to V_i^{AE} in (1.12 and 1.14)), two electrodes were connected via an analog high pass filter (single pole, 200 kHz, -3 dB frequency.) to a differential amplifier (DA1855A, LeCroy, Chestnut Ridge, NY) with a gain of 10 and a 1MHz bandwidth. The AE signal was measured with a pair of electrodes, either 1-2, 2-3, or 3-4. In every case the electrode with the lower number was connected to the positive terminal of the amplifier. The AE signal was further amplified by 45 dB (5072, Panametrics, Waltham, MA.) and filtered at 2MHz (BLP-1.9, Mini-Circuits, Brooklyn, NY). The experimental timing (illustrated in Fig. 3.2) was controlled by a field-programmable-gate-array (FPGA) chip (ezFPGA, Dallas Logic, Plano, TX). The FPGA sent out two trigger signals, a 3Hz signal to pace the heart and 500 trigger burst to an ultrasound pulser/receiver (5077PR, Panametrics). Each burst was sent to coincide with the pacing signal such that 20 triggers were sent before the heart was paced and 480 afterwards in one heart cycle. The interval between ultrasound triggers was 625 μs (1600Hz).

The pulser-receiver excited the ultrasound transducer which was focused on the left ventricle. For each trigger, AE and pulse echo (PE) traces were acquired concurrently and sampled at 12.5 MHz by a digital acquisition (DAQ) board (PDA12, Signatec, Newport Beach, CA). Each trace was 2048 samples long. Consequently, data acquired with each trigger burst were two 2048 x 500 matrices, an AE matrix and a PE matrix. The first dimension of each data matrix will be hereafter referred to as the fast-time axis and the second dimension will be referred to as the slow-time axis.

3.2.3. Experimental Procedure

The AE and PE data were acquired in an XZ-slice by moving the transducer in 20 1 mm steps along a line parallel to the x-axis. At each step AE and PE matrices were averaged over 64 heart cycles (trigger bursts). For each pair of electrodes (1-2, 2-3, 3-4), an XZ-slice was captured for each pacing location, right atrium or apex. After every XZ-slice was captured, two control experiments were performed. One (FOAM) repeated the experiment unchanged except the path of the ultrasound was blocked with a piece of polystyrene. In the other control (US off), the ultrasound path was clear but the ultrasound transducer was disconnected from the pulser. In the control experiment only the A-line corresponding to x=0.54 mm was captured. An XZ-slice corresponding to a single slow-time index will be referred to as a frame in the remainder of the Chapter.

3.2.4. Data Processing

To reduce noise each data matrix (AE or PE) was band pass filtered along its fast-time axis (0.4-0.8 MHz) and AE data were further band pass filtered in slow time (pass band = 15-80 Hz). The AE signals were converted to complex analytical form, basebanded and low-pass filtered in the xz-plane where z is the fast time axis. The 2D filter was Gaussian in the frequency domain with a full width at half maximum (FWHM) = 0.36 mm^{-1}. For fair comparison, low frequency ECG data were filtered with the same slow-time filter as AE signals.

To gauge the imaging capabilities of the AE measurement system we estimated its point spread function (PSF). The inherent PSF of the acoustic system was estimated from FWHM of the autocorrelation of the PE data as being 6.24 mm axially and 7.07 mm laterally (one-way). The FWHM of the PSF of the fast-time bandpass filter was 3.87 mm

and the FWHM of the PSF of the 2D filter was 2.45 mm. Assuming perfectly Gaussian envelopes the total PSF of the AE measurement was therefore 7.74 mm axially and 7.42 mm laterally.

A number of parameters of the ECG and AE signal envelopes were measured to facilitate comparison, onset latency (t_e), time to peak signal (t_p) and the -3dB width of the signal envelope (w_{-3dB}). The signal-to-noise ratio (SNR) of the AE signal was also measured for each data set. The envelope of the AE signal was found by choosing the peak magnitude of each frame as representative of the AE signal at that slow-time index. The envelope of the ECG signal was similarly obtained by finding the analytic signal along the slow-time axis.

The timing measurements used are illustrated in Fig. 3.3. The ECG signal was normalized by subtracting the minimum envelope and dividing by the peak signal and the AE signal envelope was normalized by subtracting minimum envelope magnitude and dividing the result with the peak envelope. The normalized envelopes of AE and ECG signals were otherwise treated the same.

Although the ECG signals were acquired on all electrodes in each acquisition, the AE signals were acquired on only one pair at a time. As a result of the finite time to complete each AE acquisition and because physiological signals are not strictly deterministic there were slight differences in timing between each AE acquisition which were reflected equally in ECG and AE signals. To calibrate, the time to peak of the ECG signal on electrodes 1-2 for each acquisition was measured. Any inter-acquisition delay was corrected by shifting all ECG and AE signals by the measured delay.

The onset latency (t_e) was defined as the delay between the stimulation (t = 0) and the time when the envelope first crossed 0.707 (-3dB point). The -3dB point was chosen instead of 0.5 because there were some AE signals with poor SNR where that point would not have been meaningful. The uncertainty of t_e, Δt_e, was estimated by fitting a line along the envelope at t_e and finding how much t_e varied with a 10% change in the envelope magnitude. The time to peak signal (t_p) was the time between the stimulation and peak envelope and the -3dB width (w_{-3dB}) was the time between the first and last time the envelope crossed the 0.707. The AE-SNR was measured as the ratio of the peak AE signal and the baseline AE signal, in dB. The baseline AE signal was the root mean square (RMS) value of the AE data matrix corresponding to the 20 pre-stimulus triggers.

3.2.5. Displacement Estimation

Correlation-based phase-sensitive 2-D speckle tracking [7] was used to estimate residual motion using PE frames. The tracking algorithm calculated the complex cross-correlation coefficient between speckle-sized blocks in a reference frame and every other frame. Correlation coefficient functions were filtered to reduce tracking error. Axial and lateral dimensions of the correlation kernel were estimated from the FWHM of the magnitude of the autocorrelation function to be 3.1 mm x 5 mm(52 x 5 samples) and the correlation filter was chosen as 7.8 mm x 7 mm (130 x 7 samples).

Coarse estimate of both axial and lateral displacements were computed by finding the peak position of the magnitude of the correlation coefficient function using a parabolic fit. The axial displacement was further refined by calculating the position of the phase zero-crossing around the peak correlation coefficient [7]. The spatial resolution of the displacement estimate was 8.4 mm x 7.4 mm. Due to the small displacement being

estimated and to the relatively large variance in lateral speckle tracking only axial tracking results were considered [8].

The choice of reference frame was derived from low frequency ECG data. The differential signal between the three pairs of electrodes (1-2, 2-3 and 3-4) was calculated. The slow-time segment corresponding to the peak of each differential signal (peak-time) was found. The mean peak-time of the three differential signals was used as the reference time.

3.3. Results

We report for the first time mapping of biological current in the live rabbit heart using ultrasound. Three UCSDI movies are associated with this Chapter--two from heart A (Movies 3.1 and 3.2) and one from heart B (Movie 3.3). A screen shot from Movie 3.1 is depicted in Fig. 3.4 and explained below. The figures 3.4, 3.5, and 3.6 correspond with heart A.

Figure 3.4 demonstrates the ultrasound dependence of the AE signal. A single frame from Movie 3.1 corresponding to slow-time=170 ms is shown in Fig. 3.4 on the left. Each frame is a B-mode PE image (30dB dynamic range, grayscale) superimposed on which is an UCSD image of current flow (hot/cold scale). An UCSD images is bipolar (signed) but its amplitude is logarithmically compressed such that the positive and the negative amplitude have 10 dB of dynamic range. The boundary of the heart in the pulse-echo image is depicted by the dashed white lines and the location of the acoustic window of the chamber is noted with a white arrow.

The radio frequency (RF)-traces shown on the right correspond to the vertical dotted white line in the image on the left. In the plot at the bottom right is the PE RF-trace and a black dashed line that marks the interior of the heart. The RF-traces in the top right are RF- traces were measured with the electrodes where the solid blue line is the AE signal, the black dashed line corresponds to a control where the acoustic path was blocked by a block of polystyrene and the red dotted line is the control where the ultrasound transducer was disconnected. In these plots as well as the image to the left the fast-time axis (z-axis) has been converted to spatial dimension. The z-axis of the AE plots was converted based on one-way propagation while the z-axis of the PE plots was converted based on two-way propagation. The peak amplitude of the blue curve is 0.71 μV while the RMS values of the black dashed and red dotted curves are 0.09 and 0.15 μV, respectively. If we assume that the controls are a good estimate of the noise, the maximum SNR is 18 and 14 dB after filtering, respectively.

Figs. 3.5 and 3.6 show that the AE signal has spatial and temporal patterns consistent with the spreading cardiac activation wave. In Fig. 3.5 on the right is an illustration of the heart showing both the layout of the recording electrodes with respect to the x-axis as well as the location of the stimulation electrodes. On the left are measured results, where each column represents a pair of electrodes 1-2, 2-3 or 3-4. The bottom row presents the low frequency ECG traces while the images in the top row are bipolar UCSD M-mode images measured with the same pair of electrodes in which the magnitude of the AE signal is logarithmically compressed and then given the sign of the real part. The magnitude is symmetrically cut just above the noise level. The time scale is short (0.1-0.2 sec) to highlight the disposition of AE signals along x axis. That is, the signal measured

with electrodes 1 and 2 is around x=0 mm while the signal measured with electrodes 3-4 is at around x=7 mm with the signal measured with electrodes 2 and 3 between the two. The small dispersion of signals in slow-time is related to the propagation paths of the electrical stimulation. When the heart is stimulated from the right atrium, the activation signal travels along the natural pathways throughout the ventricle and the activation wave travels both from the apex to base as well as transmurally [9]. The long delay from the stimulation to the peak of the signals (0.15 sec) was due to propagation delays in the atrium as well as in the atrio-ventricular node [10].

Fig. 3.6 shows that the AE signal propagated in slow-time and demonstrates the lack of motion during the generation of the AE signal. The geometry of the heart and the disposition of the electrodes are shown on the right. Note that the heart was stimulated at the apex as a result the delay between stimulation and the appearance of electrical signals was less than that when the heart was stimulated at the right atrium, as depicted in Fig. 3.5. The top two images on the left are bipolar AE M-mode images corresponding to the lateral line z = 100 mm, shown as a horizontal white dotted line in Fig. 3.4. The top image was measured using electrode 1 and 2 while the image below it was measured with electrodes 2 and 3. In these images the magnitude is logarithmically compressed and given the sign of the real part. Notice that the image corresponding to electrodes 2-3 is both shifted in slow-time and space with respect to the image measured with electrodes 1 and 2. By drawing a line through AE signal (slanted white dotted line in Fig. 3.6) we estimate from the slope the propagation speed along z=100mm to be 0.25±0.05 mm/ms. This line was chosen visually and the uncertainty reflects that this choice is not unique. For comparison, the velocity estimate from the three differential low frequency signals

captured simultaneously was 0.31±0.05 mm. The plot second to bottom shows the low frequency ECG signal measured concurrently with the data shown in the top two images. The solid blue line was measured with electrodes 1 and 2 and the green dotted line was measured with electrodes 2 and 3.

The plot at the bottom is the axial displacement along line x= 0.54 mm estimated using speckle tracking. The peak displacement was 10 μm which demonstrates that the BDM has greatly reduced the motion of the heart. This plot also shows that during the AE signal there was little motion (<5 μm) and that the main motion occurred 160 ms after the stimulation. Here the reference point in the displacement curve is the positive displacement peak.

The results of the timing and SNR measurements from both heart A and B are tabulated in table 3.1 where they are sorted by stimulation location (AT, AP) and electrode pairs (1-2, 2-3 and 3-4). The measured uncertainty in the onset latency of both AE and ECG was relatively small typically 1-3 ms while the width at -3dB, a measure of the uncertainty in the peak position was relatively large at 10-15 ms. The onset latency and the time-to-peak of AE and ECG signals are compared graphically in the scatter plots in Fig. 3.7. The upper and lower groups in the scatter plots correspond to measurements with atrial and apical stimulation, respectively. A linear fit through the data points was highly significant, R^2=0.987 and R^2=0.992 for onset latency and time-to-peak measurement, respectively. The unity slopes of the fitted lines tell us that t_e and t_p of AE and ECG have a fixed delay between them and the intercepts, -0.8 ms for t_e and -1.04 ms for t_p show that this delay is very small.

3.4. Discussion

In this chapter we have described the first mapping of bioelectric current in a live rabbit heart using UCSDI. This demonstrates that UCSDI is a potentially viable cardiac mapping technique which could significantly improve intracardiac procedures.

Experimental results indicate that UCSDI provides spatial and temporal patterns of the propagating cardiac activation wave. Moreover, measurements were repeatable, dependent on the presence of ultrasound, and consistent with the simultaneously-recorded ECG signals. The results of the control experiments in Fig. 3.4 indicate that the AE signal disappeared in the absence of ultrasound and was spatially localized to the correct anatomical location based on one-way acoustic propagation. In addition Fig 3.4 demonstrates that the AE signal occurred within the heart wall at the side facing the transducer, consistent with both the electrode placement and the orientation of the heart illustrated in Fig. 3.1.

The motion of the heart was suppressed with the excitation-contraction de-coupler BDM, as demonstrated by the plot at the bottom of Fig. 3.6, showing axial displacement. Not only was the maximum absolute displacement miniscule (10 μm), but it occurred >100 ms after the electric signals. Motion during the electric signals was very small (<5 μm), which means that it is highly unlikely that the AE signal was a motion artifact.

According to the timing measurements illustrated in Fig. 3.7 there was good correlation of the onset time and time-to-peak between AE and ECG signals. The unity slope and the small intercept value of the fitted lines of these plots means there was minimal delay between the AE and ECG. The consistent timing between the AE and ECG signals further supports the electrophysiological origin of UCSDI.

Atrial and apical stimulation result in different propagation patterns. When the heart is stimulated at the apex, propagation of the activation wave is mostly parallel to the long axis of the heart whereas when the heart is stimulated from the right atrium the wave propagates mostly from the endocardium outward [9]. In Fig. 3.5 the low frequency and AE signals occur at approximately the same slow-time yet the AE signals occur at different x-positions. Since the recording electrodes were arrayed in the left ventricle parallel to the x-axis, this is consistent with what one would expect from a wave propagating from the endocardium outwards.

Since the wave was propagating parallel to the x-axis for data presented in Fig. 3.6, AE signals should be delayed in slow-time. Not only was there a delay between the signal measured with electrodes 1-2 and 2-3, but in the M-mode measured with 2-3 we see that the signal spreads along a line at an angle with the slow-time axis. This strongly suggests that the AE signal captured wave propagating along the x-axis in slow-time. The propagation velocity estimated from the slope of that line, 0.25±0.05 mm/ms, is comparable to both that measured with low frequency ECG signals as well as to what others have observed [11].

The morphology of the AE signals shown in Fig. 3.5 and 3.6 are of two types: A signal with a single zero crossing (electrodes 1-2 in Fig. 3.5 and 3.6) or two zero-crossings (electrodes 2-3 in Fig. 3.6 and electrodes 3-4 in Fig. 3.5). The recording lead fields have the highest spatial frequencies close to the electrodes and so after a convolution by the PSF of the AE measurement system we would expect the highest signal closest to the electrodes. The zero-crossings in the AE signal could be interpreted as the time the wave passes a single electrode. A single zero crossing signal means one

electrode was out of the imaging plane but a signal with two zero crossings had both electrodes in plane. Notice also from the signal equation (1.14) that the PSF of the ultrasound system will filter the signal along the slow-time axis. The extent of that filtering will be studied further.

The large PSF (7mm x 7 mm) of the AE system was mainly due to the low frequency transducer used. As a result of this large PSF and the relative proximity of the electrodes (3-6 mm), the maximum mapping distance away from the electrodes was within the width of the PSF. For reference the lead field strength of a monopolar electrode goes down 12 dB per doubling of distance from the electrode. The system used in this proof-of-principle study is far from optimal. In future studies using transducers with higher center frequency, we explore techniques that provide better electronic noise management with enhanced spatial resolution and sensitivity.

Another limitation of this study is that it was not possible to acquire AE signals on all of the electrodes simultaneously because of equipment limitations. There were subtle changes in the heart between acquisitions which were reflected in the small inter-acquisition delays. However, these changes were small since the low frequency signals, acquired simultaneously for all acquisition, did not exhibit significant change in signal morphology.

From the AE traces shown in Fig. 3.4 the sensitivity of the method can be roughly estimated. The blue curve shows the maximum AE signal acquired while the control curves are appropriate estimates of system noise. According to the signal equation (1.14) the AE signal is a spatial sum that depends on a number of geometric factors. Assuming that the current source had constant magnitude and direction and was perfectly parallel to

the electrode lead field within a resolution cell of the AE measurement system we can extract the current source from the spatial sum. The spatial sum after extraction is a constant representing the sensitivity and is equal to the ratio of the maximum signal amplitude and maximum current density. From [12, 13] and chapter 1.2.2 the current density of the activation wave is ~5 mA/cm^2 therefore the sensitivity was 0.141 $\mu V/(mA/cm^2)$. Accordingly, the noise level, or the smallest detectible signal with this setup, was 0.3-0.5 mA/cm^2.

We have described for the first time the detection and mapping of biological current using UCSDI. UCSDI has great potential advantages as a tool to map arrhythmias during interventional cardiac procedures in which an ultrasound array and a sparse array of recording electrodes are integrated into an intracardiac catheter. The spatial resolution of UCSDI is determined by the focusing characteristics of the ultrasound beam. Electronic steering of the ultrasound beam would provide real-time electrical mapping of the heart. As the accompanying movies demonstrate, UCSDI images are automatically registered to the B-mode ultrasound, which suggests the possibility of dynamic feedback of mechanical and electrical cardiac events during ablation procedures and pacemaker insertion.

Table 3.1 Timing characteristics measured from the envelope of the AE and ECG signals. The parameters are illustrated in Fig. 3.7. The acronyms are: H=Heart, SL= stimulation location, AT=right atrium, AP=apex, EL=electrode pair, t_p = time-to-peak, t_e=onset latency, w_{-3dB}= the -3dB with of the signal. AE= acousto-electric, ECG=low frequency electrocardiograms, SNR = signal-to-noise ratio.

H	SL	EL	t_e AE [ms]	t_e ECG [ms]	t_p AE [ms]	w_{-3dB} AE [ms]	t_p ECG [ms]	w_{-3dB} ECG [ms]	SNR-AE [dB]
A	AT	1-2	168.8 ± 0.7	162.4 ± 0.9	171.3	6.8	167.8	16.6	15.7
		2-3	165.4 ± 0.6	151.6 ± 2.0	169.1	9.9	160.4	19.6	13.5
		3-4	145.4 ± 0.8	144.2 ± 12.0	149.1	9.2	150.2	11.0	11.1
	AP	1-2	12.9 ± 1.1	14.4 ± 1.5	16.6	6.8	21.2	12.8	14.7
		2-3	22.4 ± 1.0	30.2 ± 1.8	49.8	6.2	49.8	13.2	10.2
B	AT	1-2	157.7 ± 0.8	135.0 ± 12.0	160.8	5.5	143.6	14.6	11.9
		2-3	135.5 ± 0.4	133.0 ± 0.8	137.6	6.2	137.6	12.0	10.2
	AP	1-2	28.3 ± 0.5	18.8 ± 1.7	31.4	8.0	25.4	14.0	13.4
		2-3	29.5 ± 0.8	28.3 ± 1.2	33.8	6.2	34.1	12.0	13.4

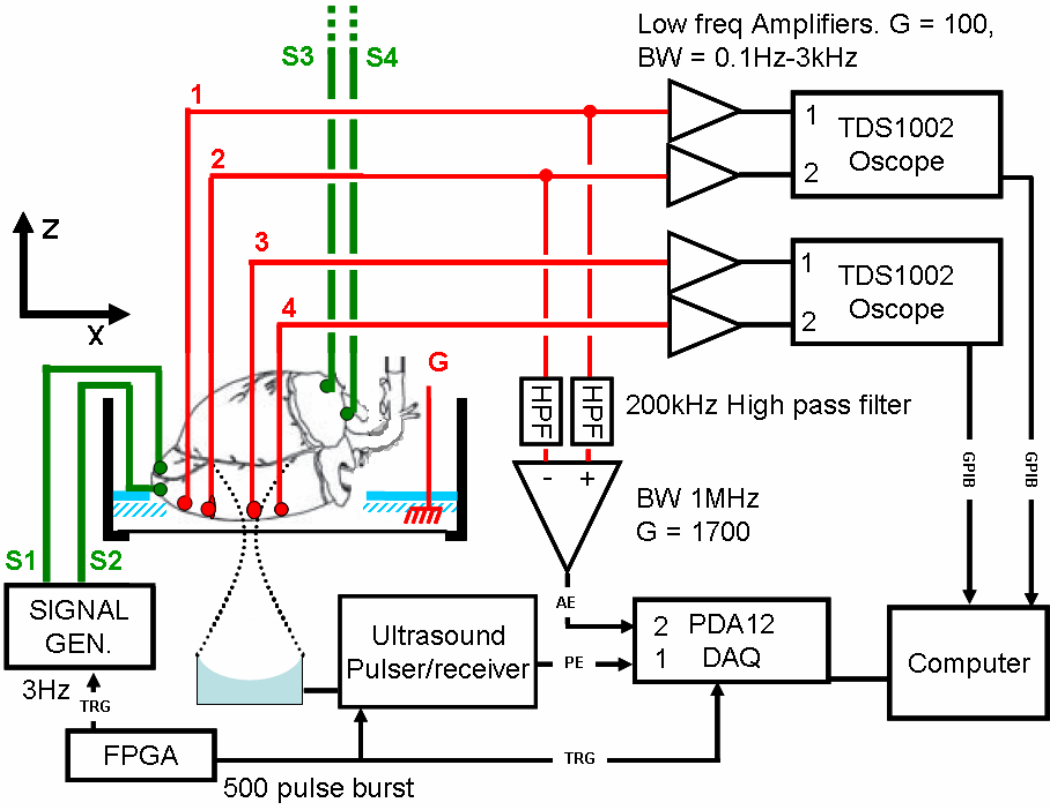

Figure 3.1. Experimental setup. Four tungsten stimulating electrodes (S1, S2, S3 and S4) and four recording electrodes (1, 2, 3 and 4) were inserted into the heart. S1 and S2 were inserted in the apex and S3 and S4 were inserted into the right atrium. The recording electrodes were inserted in a line parallel to the long axis of the heart. The voltage on each electrode with respect to ground (G) was amplified with a low frequency amplifier and digitized with an oscilloscope (TDS 1002). In addition, two of the recording electrodes (here electrodes 1 and 2) were connected via an analog high pass filter to a differential amplifier. The high frequency voltage (AE) was sampled and digitized concurrently with the pulse-echo (PE) signal by a digital acquisition board (DAQ). A field-programmable-gate-array (FPGA) controlled the experimental timing. It sent a trigger to the signal generator that paced the heart as well as the ultrasound pulser-receiver. The heart was paced from the apex if the signal generator was connected to electrodes S1 and S2. If the signal generator was connected to electrodes S3 and S4, the heart was paced from the right atrium.

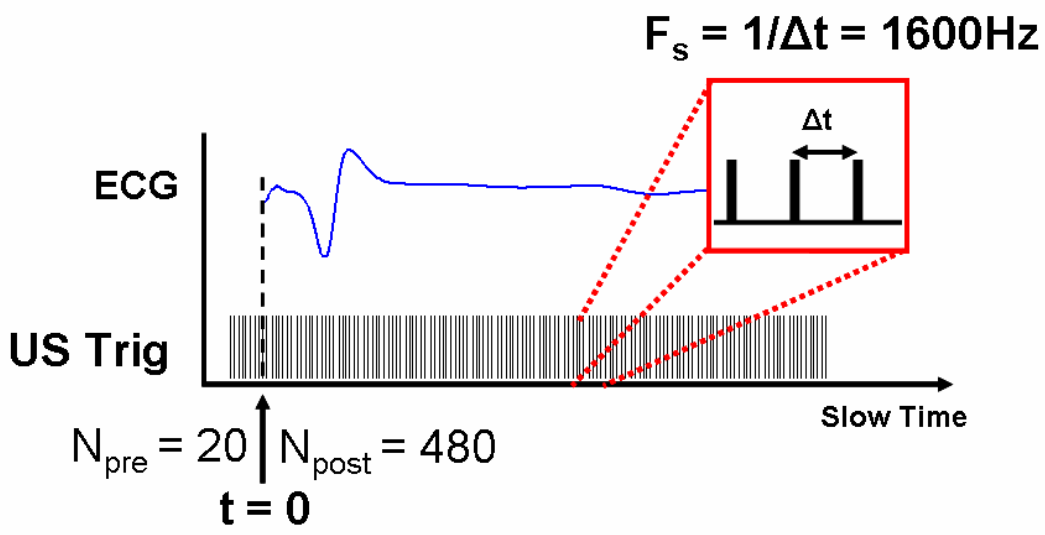

Figure 3.2. Experimental timing. The heart was paced by the FPGA at a 3-Hz rate. Prior to the heart stimulus, the ultrasound (US Trig) transducer was given 20 pre-triggers (N_{pre}). After the stimulus ultrasound was triggered (N_{post}) 480 times at a pulse repetition frequency of 1600 Hz.

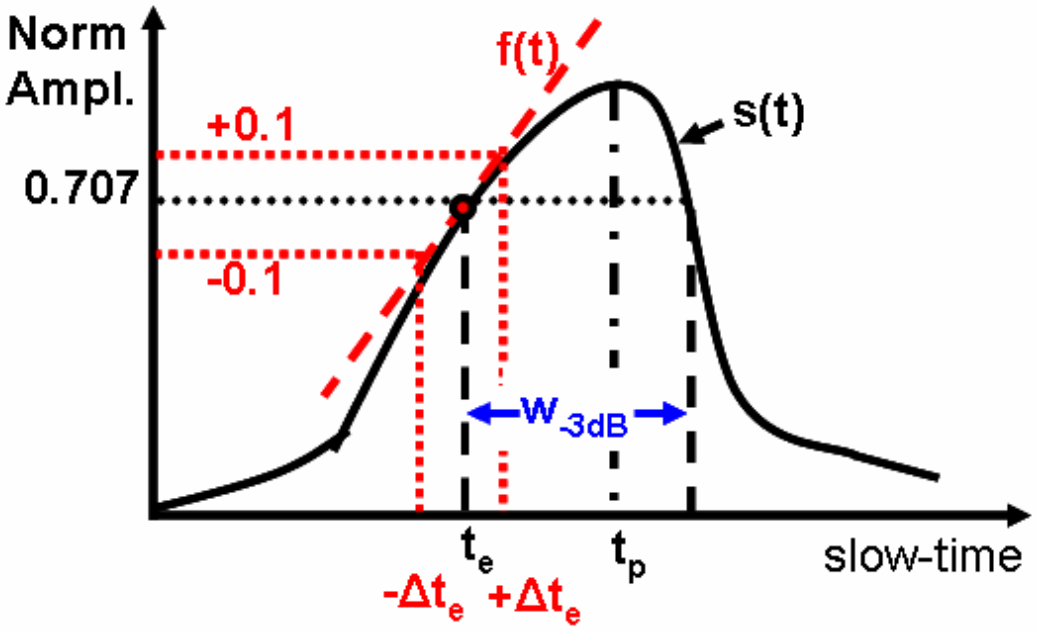

Figure 3.3. Diagram to illustrate measurement of onset latency (t_e), peak time (t_p) and width of the peak at -3dB (w_{-3dB}). The solid black line is a normalized signal envelope s(t) in slow-time. The onset latency corresponded to the first time the envelope crossed s(t) = 0.707 (-3dB). The uncertainty in t_e, Δt_e, was estimated by fitting a line f(t) through (t_e, s(te)) and finding the Δt_e such that $f(t_e \pm \Delta t_e) = s(t_e) \pm 0.1$. The width w_{-3dB} was defined as the first and last time the AE signal passed through s(t) = 0.707.

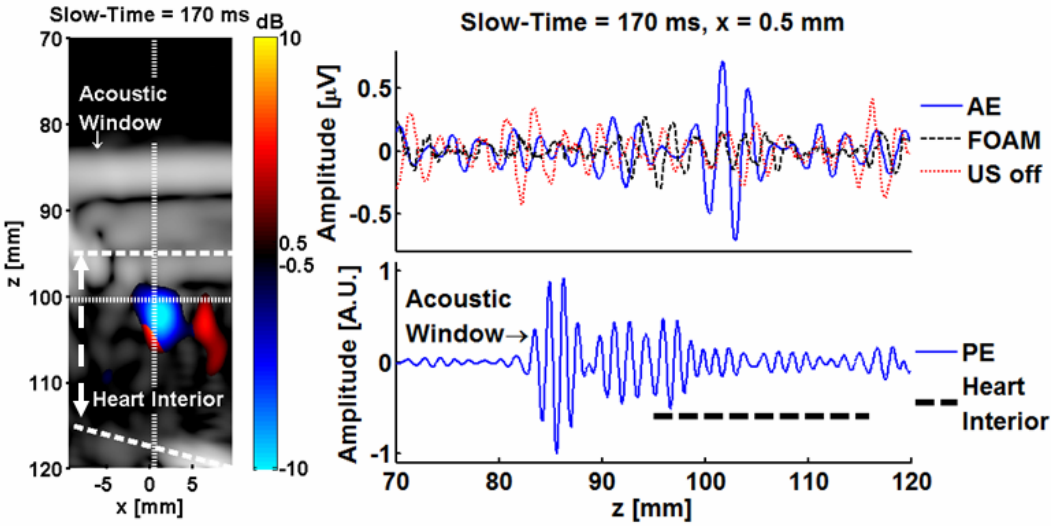

Figure 3.4. Example RF-traces. Left: A screen shot from Movie 3.1, representing data from heart A measured with electrodes 1-2 and paced at the atrium. The bipolar acousto-electric (AE) image is superimposed on top of the B-mode pulse-echo image (dynamic range=30 dB) shown in grayscale. The magnitude of the AE image is logarithmically compressed while keeping the sign of its real part. The white horizontal dotted line is the image line used in the bipolar m-mode displays in Figs. 3.5 and 3.6. Right Top: Radio frequency (RF) traces corresponding to the dotted white vertical line (x=0.5 mm) in the figure on the left. The blue solid line is the AE RF trace, the black dashed line corresponds to the control where the ultrasound path is blocked with polystyrene. The red dotted line corresponds to the control where the ultrasound transducer was disconnected from the ultrasound pulser. Right Bottom: The PE RF trace acquired concurrently at the same A-line. The black dashed horizontal line marks the interior of the heart.

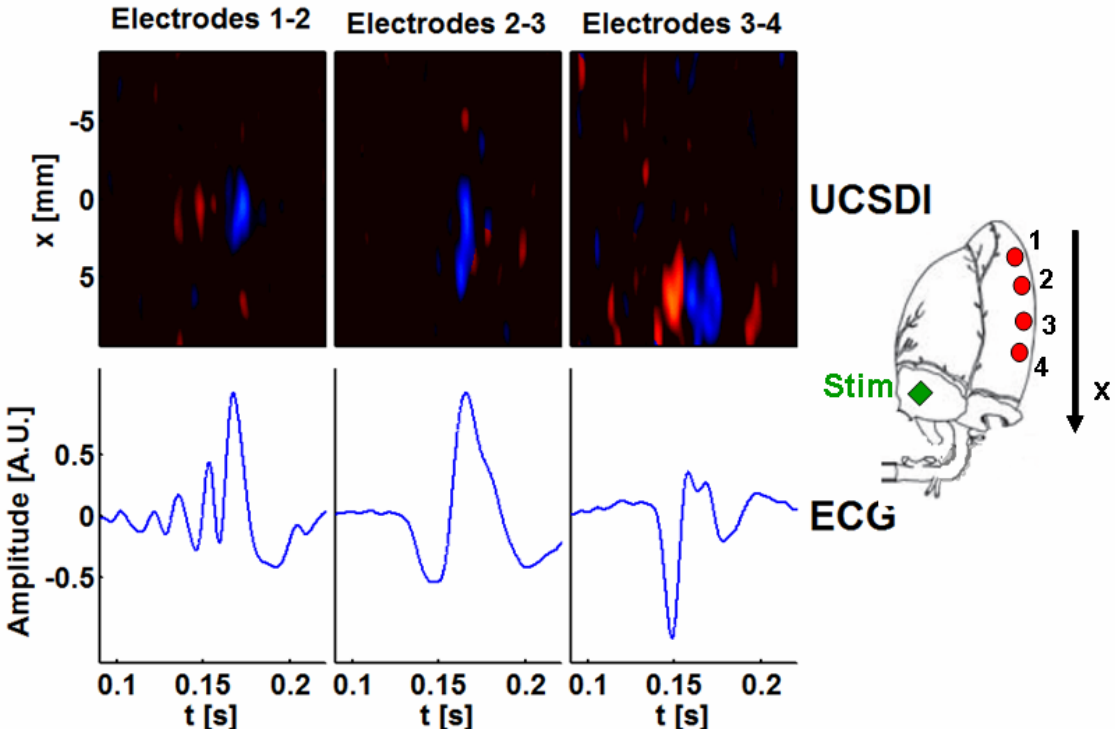

Figure 3.5. Top row on the left: Lateral bipolar M-mode electrical traces corresponding to z= 100 mm in Fig. 3.4 where each column is the signal measured by a different electrode pair. In these images the magnitude of the AE signal is logarithmically compressed and given the sign of the real part. Bottom row: The plot in each column is the low frequency ECG signal measured on the same pair of electrodes as the M-mode plot above it. The figure on the right illustrates the geometric arrangement of the recording electrodes (numbered red dots) and stimulation location (green diamond) in the heart with respect to the x-axis. Note that AE signals occur at roughly the same time as the low frequency signal yet they are spatially separated along the x-axis.

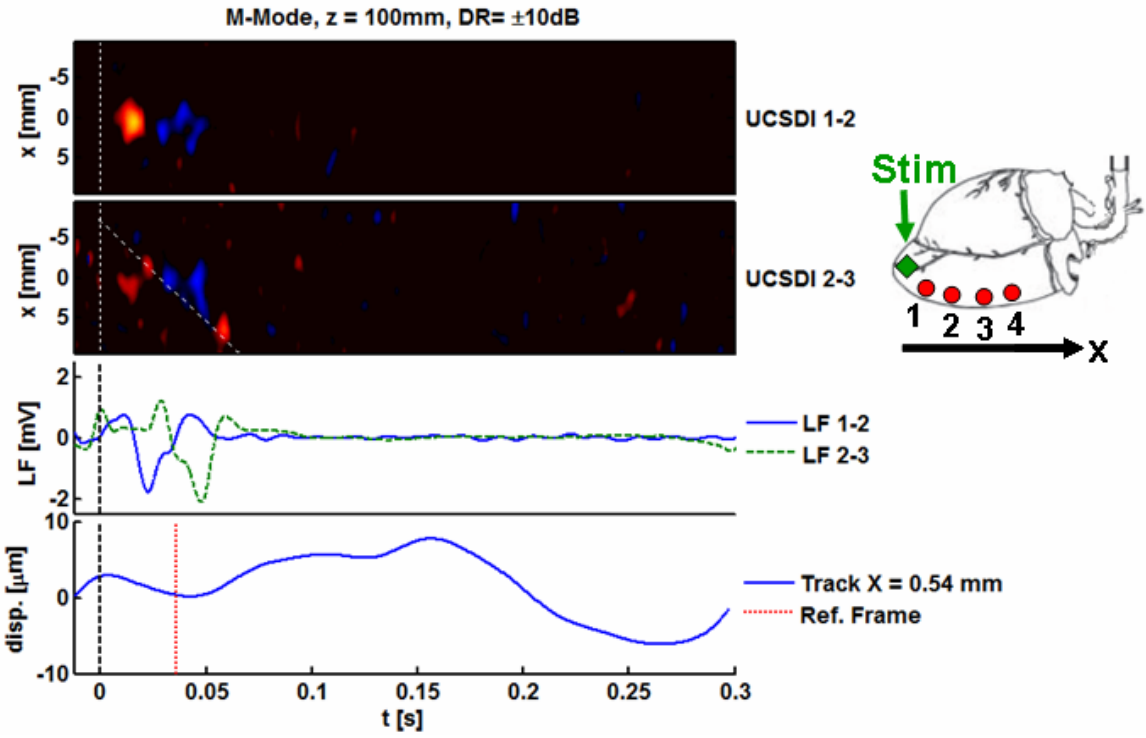

Figure 3.6. Right: An illustration of the heart showing the disposition of the recording electrodes (numbered red dots) and the stimulation electrode (green diamond) along the x-axis. Left: The top two images are AE bipolar M-mode plots corresponding to the lateral line z=100mm. The image at the top was measured on electrodes 1 and 2 while the image below it was measured with electrodes 2 and 3. In the plot second to bottom are the low frequency ECG plots measured concurrently on the same electrodes. The solid blue line was measured with electrodes 1 and 2 while the green dashed line was measured with electrodes 2 and 3. At the bottom are the tracking results corresponding to x=0.54 mm in the top M-mode image. The vertical dashed line in all of the images mark t= 0. While the slanted dashed white line in the figure next to top was used to estimate the velocity of the activation wave.

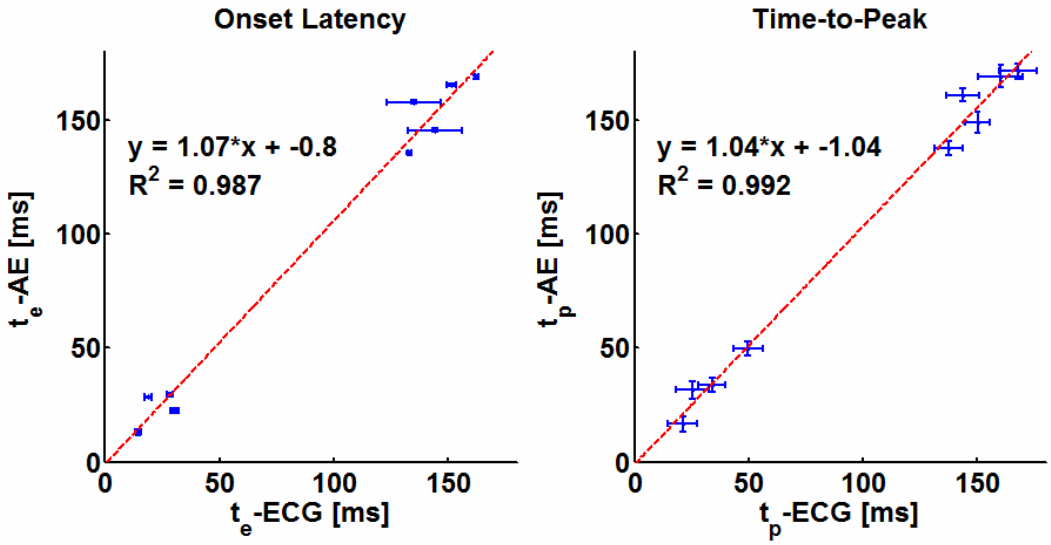

Figure 3.7. Plots of the timing measurements tabulated in table 3.1 demonstrating the relationship between the low frequency ECG signals and the AE signals. These plots combine measurements from hearts A and B. In the plot on the left the error bars are the measured uncertainty, while in the plot on the right the horizontal and vertical error bars are the w_{-3dB} of the ECG and AE signals respectively.

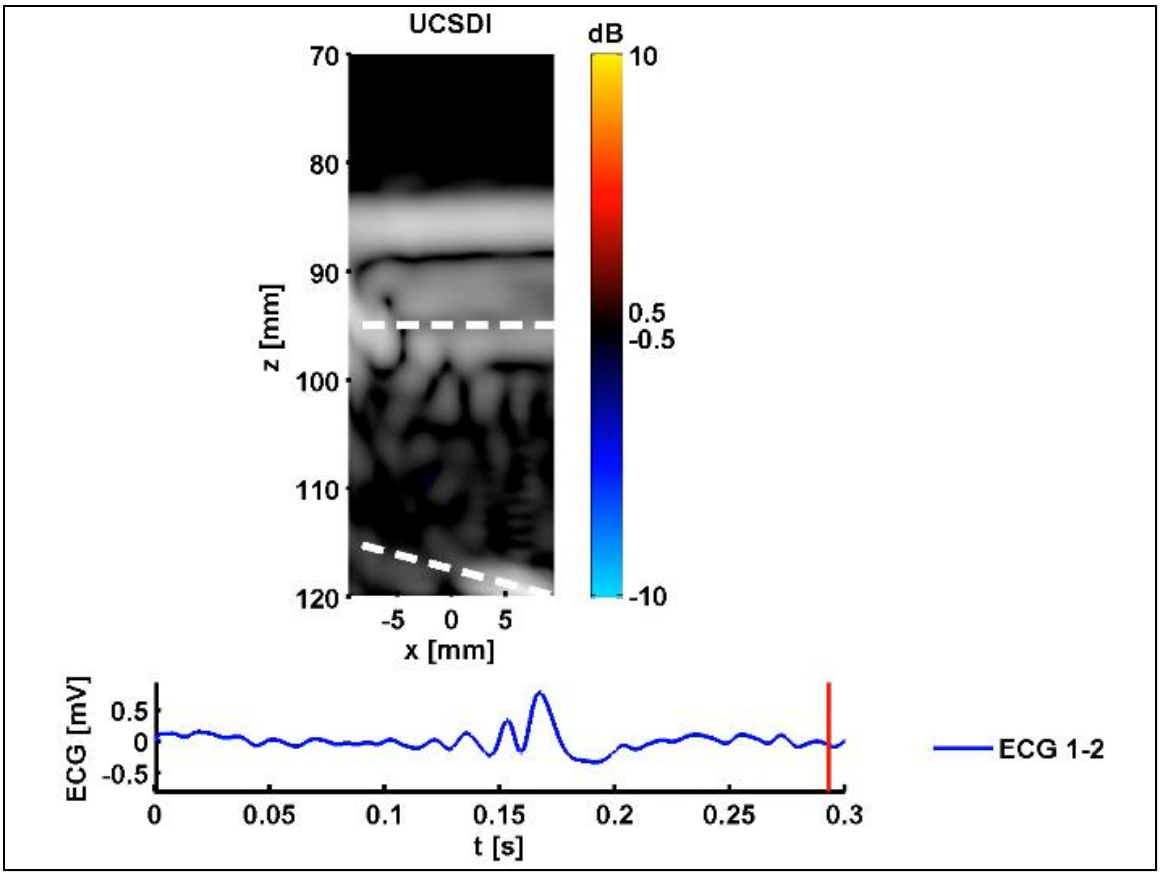

Movie 3.1. This is a movie of heart A, UCSDI and ECG are measured from electrodes 1-2 and the heart is stimulated at the right atrium.

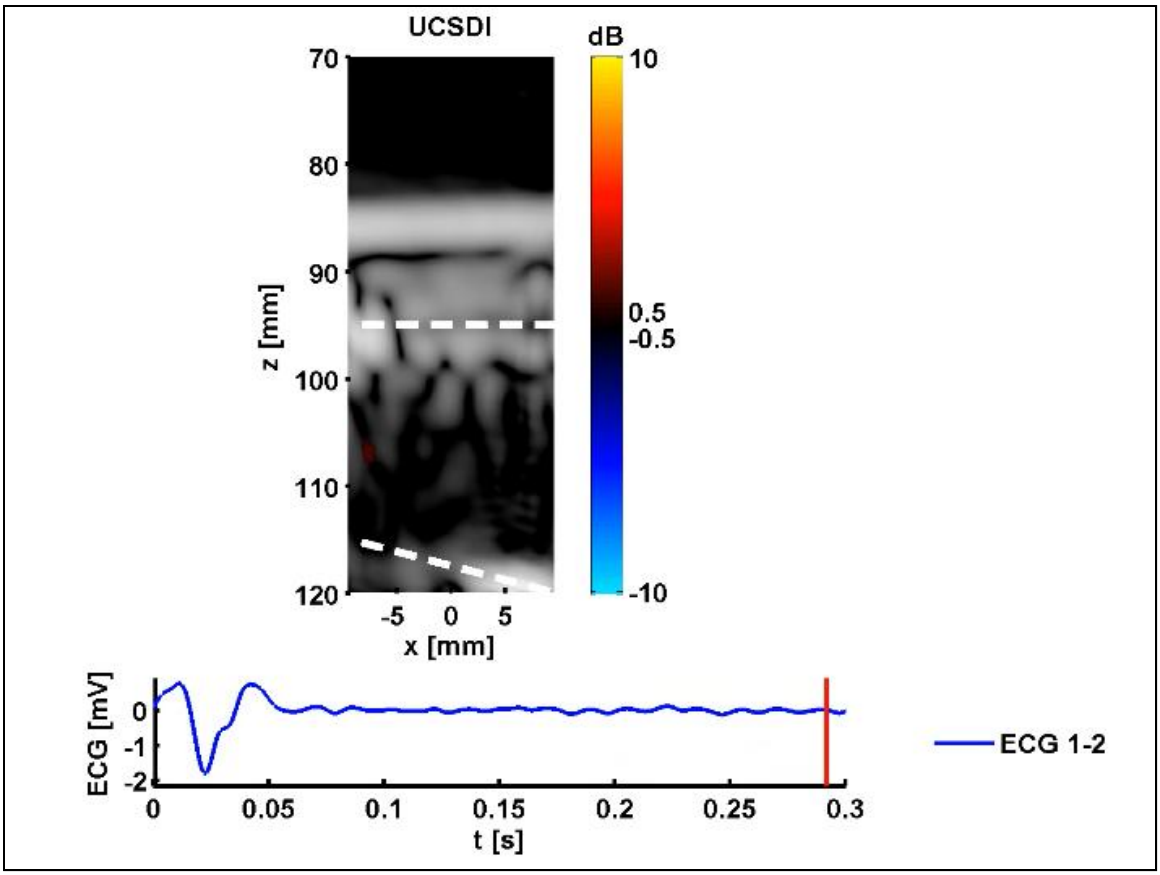

Movie 3.2. This is a movie of heart A, UCSDI and ECG are measured from electrodes 1-2 and the heart is stimulated at the apex.

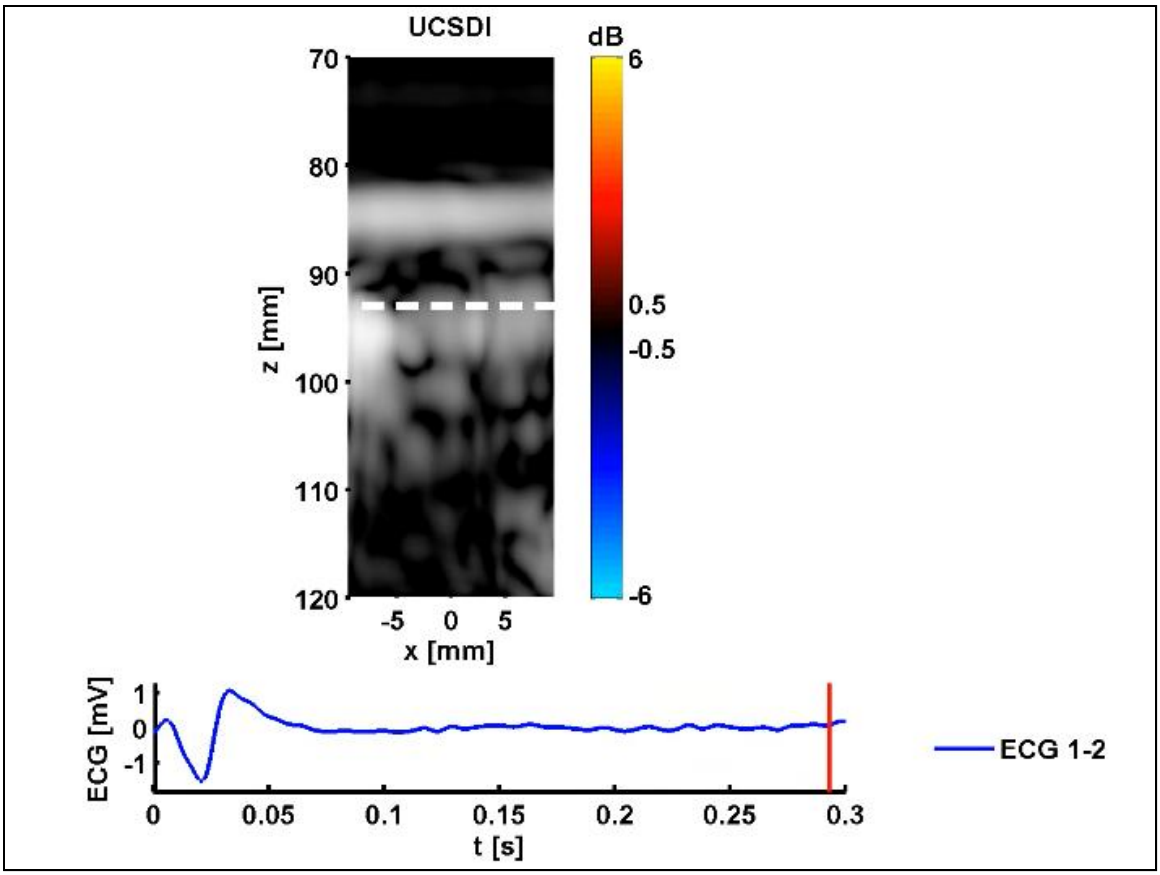

Movie 3.3. This is a movie of heart B, UCSDI and ECG are measured from electrodes 1-2 and the heart is stimulated at the apex.

3.5. References

[1] R. Olafsson, R. S. Witte, K. Kim, S. Ashkenazi, and M. O'Donnell, "Electric current mapping using the acousto-electric effect - art. no. 61470O," in *Medical Imaging 2006: Ultrasonic Imaging and Signal Processing*. vol. 6147, S. Y. Emelianov and W. F. Walker, Eds., 2006, pp. O1470-O1470.

[2] R. Witte, S., Olafsson, Ragnar and O'Donnell, Matthew, "Acousto-electric detection of current flow in a neural recording chamber," in *2006 IEEE International Ultrasonics Symposium*, Vancouver, BC, Canada, 2006, pp. 5-8.

[3] R. Witte, R. Olafsson, S. W. Huang, and M. O'Donnell, "Imaging current flow in lobster nerve cord using the acoustoelectric effect," *Applied Physics Letters,* vol. 90, pp. -, Apr 16 2007.

[4] R. Olafsson, C. Jia, S.-W. Huang, R. S. Witte, and M. O'Donnell, "Detection of Electrical Current in a Live Rabbit Heart using Ultrasound," in *2007 IEEE Ultrasonics Symposium*, New York, NY, 2007, pp. 989-992.

[5] E. J. Tanhehco, K. Yasojima, P. L. McGeer, R. A. Washington, and B. R. Lucchesi, "Free radicals upregulate complement expression in rabbit isolated heart," *American Journal of Physiology-Heart and Circulatory Physiology,* vol. 279, pp. H195-H201, Jul 2000.

[6] S. Kettlewell, N. L. Walker, S. M. Cobbe, F. L. Burton, and G. L. Smith, "The electrophysiological and mechanical effects of 2,3-butane-dione monoxime and cytochalasin-D in the Langendorff perfused rabbit heart," *Experimental Physiology,* vol. 89, pp. 163-172, Mar 2004.

[7] M. A. Lubinski, S. Y. Emelianov, and M. O'Donnell, "Speckle Tracking Methods for Ultrasonic Elasticity Imaging Using Short Time Correlation," *IEEE Transactions on Ultrasonics, Ferroelectrics, and Frequency Control,* vol. 46, pp. 82-96, 1999.

[8] M. A. Lubinski, S. Y. Emelianov, K. R. Raghavan, A. E. Yagle, A. R. Skovoroda, and M. O'Donnell, "Lateral Displacement Estimation using Tissue Incompressibility," *IEEE Transactions on Ultrasonics, Ferroelectrics, and Frequency Control,* vol. 43, pp. 234-246, 1996.

[9] D. Durrer, R. T. Vandam, G. E. Freud, M. J. Janse, F. L. Meijler, and Arzbaech.Rc, "Total excitation of isolated human heart," *Circulation,* vol. 41, pp. 899-&, 1970.

[10] J. Malmivuo and R. Plonsey, *Bioelectromagnetism : principles and applications of bioelectric and biomagnetic fields*. New York: Oxford University Press, 1995.

[11] D. Sung, J. H. Omens, and A. D. McCulloch, "Model-based analysis of optically mapped epicardial activation patterns and conduction velocity," *Annals of Biomedical Engineering,* vol. 28, pp. 1085-1092, Sep 2000.

[12] P. R. Malmviou J., "Chapter 8: Source-Field Models " in *Bioelectromagnetism: Principles and applications of bioelectric and biomagnetic fields* New York: Oxford University Press, 1995, pp. 148-158.

[13] Z. M. Liu, C. G. Liu, and B. He, "Noninvasive reconstruction of three-dimensional ventricular activation sequence from the inverse solution of

distributed equivalent current density," *IEEE Transactions on Medical Imaging,* vol. 25, pp. 1307-1318, Oct 2006.

CHAPTER 4
ELECTROMECHANICAL IMAGING

4.1. Introduction

Advanced heart failure can lead to electromechanical delay either within each ventricle or between the left and right ventricle. As a result, the heart does not contract uniformly and its efficiency or ejection fraction is reduced. Cardiac resynchronization therapy (CRT) using either uni- or bi-ventricular pacing is an established procedure for patients not responding to drug treatment [1-3]. Clinical studies have shown, however, that 30% of patients do not respond to this treatment. The two primary cited reasons for failure are improper placement of left ventricular pacing leads and poor selection of patients for the treatment [3].

The traditional selection criterion for CRT in heart failure is the presence of a wide QRS-complex in surface electrocardiograms (ECG). The QRS-complex is produced during ventricular activation; therefore, a long QRS-complex can indicate asynchronous spread of the activation wave throughout the ventricles [3, 4]. It has been demonstrated, however, that a wide QRS-complex is a poor indicator of electromechanical delay and mechanical asynchrony [5, 6]. As a result, echocardiographic techniques such as Tissue Doppler Imaging (TDI) and M-mode ultrasonography are used in conjunction with ECG analysis for diagnosis and patient selection [7].

Given the high rate of non-responders, the electrical and mechanical nature of the problem and the high cost of the procedure (up to $100,000 including both device and procedure [2]), there is a need for an imaging technique that combines both electrical and mechanical imaging. Some have proposed such a modality using MRI mechanical imaging with epicardial electrode mapping [8], sequential electroanatomical mapping [9] and intracardiac ultrasound with non-contact endocardial mapping [10]. These methods either are time consuming or require a non-trivial registration between the mechanical and electrical maps.

In this chapter, a new technique for cardiac electromechanical imaging that combines UCSDI and ultrasonic strain imaging is described and the first measurements reported. Phase sensitive ultrasonic speckle tracking is an established method for characterizing the contractile properties of cardiac tissue [11-14], and in Chapter 3 the ability of UCSDI to map cardiac activation currents was demonstrated.

The advantage of this combined method is that both the electrical and mechanical images are automatically co-registered to each other. The absence of any extra registration step will both save time during the procedure and increase confidence in the electromechanical delay measurements.

4.2. Methods

4.2.1. Instrumentation and Experimental Procedure

All results reported here used the same Langendorff setup presented in the previous chapter. In particular, the instrumentation used was described in Sections 3.2.1, 3.2.2, and 3.2.3. The data analyzed below are the same as collected for Chapter 3. The BDM

excitation contraction decoupler used in this study reduced the motion considerably but did not eliminate it. There was sufficient contraction remaining to be detected using phase-sensitive speckle tracking.

4.2.2. Displacement and Strain Estimation

Correlation-based phase-sensitive 2-D speckle tracking [15] was used to estimate the displacement from pulse-echo (PE) images. The tracking algorithm calculated the complex cross-correlation coefficient between speckle-sized blocks in a reference frame and every other frame. The analytic (i.e., complex) representation of the recorded RF ultrasonic signal was used in all calculations. Correlation coefficient functions were filtered to reduce tracking error. Axial and lateral dimensions of the correlation kernel were estimated from the FWHM of the magnitude of the autocorrelation function of a PE image to be 3.1 mm x 5 mm (52 x 5 samples) and the correlation filter was chosen as 7.8 mm x 7 mm (130 x 7 samples).

Coarse axial and lateral displacements were computed by finding the peak position of the magnitude of the correlation coefficient function using a parabolic fit. The axial displacement was further refined by calculating the position of the phase zero-crossing around the peak correlation coefficient. The spatial resolution of the displacement estimate was 8.4 mm x 7.4 mm. Due to the small displacement being estimated, and to the relatively large variance in lateral speckle tracking, only axial tracking results were considered here. [16]. The axial strain was estimated as the axial spatial derivative of the axial displacement and was calculated by finding the slope of a sliding linear fit to the displacement along the length of the kernel [15, 17].

The choice of reference frame was derived from low frequency ECG data. The differential signal between the three electrode pairs (1-2, 2-3 and 3-4) was calculated. The slow-time segment corresponding to the peak of each differential signal (peak-time) was found. The mean peak-time of the three differential signals was used as the reference time.

4.2.3. Data Processing

The processing and filtering of AE and PE data is described in Section 3.2.4. The electromechanical delay was estimated for every electrode pair (1-2, 2-3, 3-4) and stimulation location (right atrium, apex) for both hearts A and B. For each dataset the pixel which contained the largest UCSDI signal for any frame across slow-time was chosen as the point of comparison. To estimate the delay between UCSDI and both displacement and strain in the pixel, the onset latency (t_e) of the slow-time envelopes of the AE signal, the displacement and strain were measured. Strain and displacement envelopes were estimated by computing the analytic representation of these variables along the slow-time axis and taking the magnitude of the complex representation. These envelopes were normalized by subtracting the minimum envelope value and then dividing by the maximum value. For strain and displacement envelopes extending beyond a single cycle (333 ms), they were extended assuming periodicity.

Although the ECG signals were acquired on all electrodes in each acquisition, the AE signals were acquired on only one pair at a time. As a result of the finite time needed to complete each UCSDI acquisition and because physiological signals are not strictly time-invariant there was slight difference in timing between each UCSDI acquisition,

reflected equally in ECG and AE signals. To calibrate, the time to peak of the ECG signal on electrodes 1-2 for each acquisition was measured. Any inter-acquisition delay was corrected by shifting all ECG, AE, displacement, and strain signals by the measured delay.

The timing measurements are illustrated in Figure 4.1. The onset latency (t_e) was defined as the delay between the stimulation (t = 0) and time when the envelope first crossed 0.707 (-3dB point). The -3dB point was chosen instead of 0.5 because there were some UCSDI images with poor SNR where that point would not have been meaningful. The uncertainty of t_e, Δt_e, was estimated by fitting a line to the envelope at t_e and finding how much t_e varied with a 10% change in the envelope magnitude.

4.3. Results

The first localized measurements of electromechanical delay in a live heart using the new technique combining UCSDI and phase-sensitive ultrasonic speckle-tracking are shown here.

Figures 4.2 and 4.3 show screen shots from Movie 4.1 corresponding to frames at 170 ms and 264 ms, respectively. Each frame presents UCSD, axial displacement, and axial strain images (hot and cold color scale) superimposed on top of B-mode ultrasound (30 dB, gray color scale). The axial displacement and strain are shown on a linear scale while the UCSD image is bipolar, where the magnitude has been logarithmically compressed but the sign of the real part is retained. In these images both the UCSDI and the ECG signal were measured with electrodes 1-2. Finally the interior of the heart is delineated between the two white dashed lines.

Figure 4.4 shows example radio frequency (RF) AE and PE traces corresponding to a single A-line in Fig. 4.2 where it is depicted as a vertical dotted line. The interior of the heart corresponds to the extent of the horizontal black dashed line.

Figure 4.5 shows an example M-mode images of UCSDI, displacement, and strain corresponding to the A-line x=0.5 mm from heart A when stimulated at the apex. Both UCSDI data and the ECG were measured with electrodes 1-2. The black dotted vertical line in the ECG plot is the slow-time index that corresponds to the reference PE frame used for speckle-tracking. In this figure we see that the displacement and strain are small and peak after the UCSDI.

The results of the timing measurements are tabulated in table 4.1 and are graphically shown in Fig. 4.6. They are the first localized electromechanical measurements of electromechanical delay. In these plots the red dashed line corresponds to t_e-U = t_e-D and t_e-U = t_e-S for the plots on the left and right respectively. Subtracting that line from the measurement, we can estimate the mean and standard deviation of the delay between UCSDI and displacement as 139.7± 68.3 ms and the delay between UCSDI and strain as 109.7 ± 70.2 ms.

4.4. Discussion

We have demonstrated a new method for electromechanical imaging of the heart which combines UCSDI and phase-sensitive ultrasonic speckle tracking.

From the movie and the screenshots in Fig. 4.2 and 4.3 it is possible to appreciate the potential advantages that this method could have in guiding lead placement for

resynchronization therapy. Standard B-mode ultrasound is **automatically** registered to a UCSDI of the electrical activity as well as maps of displacement and strain. B-mode ultrasound not only provides the geometrical context for the electrical and mechanical measurement, but can also be used for acute evaluation of hemodynamic parameters such as ejection fraction to gauge the success of resynchronization [18]. In these screenshots we see that the motion and strain are small and are greatest at the top surface of the heart. The bottom surface of the heart did not move as much because it was constrained by the sample holder.

It is hard to conclude much from the localized measurements of the electromechanical delays shown in Fig. 4.6 other than that UCSDI precedes both local displacement and strain. There was great variability in the measured values as reflected in the relatively large standard deviation in the mean delay of both strain and displacement. This variability can be explained by a number of factors. First, this was not a normally functioning heart. It was perfused with a high concentration of an excitation-contraction decoupler designed to disrupt the linkage between electrical and mechanical functioning of the heart. As a result of the BDM, the maximum displacement in the region of electrical activity was on the order of 10 μm and the strain less than 1%. Others have shown that strain SNR is small for very small strain [15].

Another limitation of this study is the large point spread function of the ultrasound system because of the low center frequency (540 kHz) of the transducer used. After filtering, the PSF of the AE measurement is 7-mm both axially and laterally whereas the PSF of the displacement and strain estimates were 8.4 mm x 7.4-mm axially and laterally. Given that a typical rabbit heart is approximately ovoid with long and short axis

dimensions of 30-mm and 20-mm respectively, it is possible that the motion within each resolution cell was not uniform.

In spite of these experimental limitations, the data presented here are the first measurements of both the electrical and mechanical activity of the heart with a new method combining UCSDI and phase-sensitive speckle tracking. The main advantage of this approach is that electrical and mechanical measurements are automatically registered to each other without the use of sophisticated mathematical algorithms. This potentially could be a valuable tool for the cardiac electrophysiologist.

Table 4.1. Timing characteristics measured from the envelope of the AE signal, Strain and displacement. The parameters are illustrated in Fig. 4.1. The acronyms are: SL=stimulation location, AT=right atrium, AP=apex, EL=electrode pair, t_e=onset latency. U=UCSDI, D=displacement, S=strain. All values are in milliseconds.

		Heart A					**Heart B**			
	SL	**AT**			**AP**		**AT**		**AP**	
	EL	**1-2**	**2-3**	**3-4**	**1-2**	**2-3**	**1-2**	**2-3**	**1-2**	**2-3**
U	t_e	167.6	165.4	144.8	12.3	23.1	157.1	135.5	27.7	27.6
	Δt_e	0.7	0.5	0.8	1.2	1.0	1.5	0.7	0.6	0.5
D	t_e	219.4	285.6	265.0	135.6	234.4	275.4	202.6	205.3	295.1
	Δt_e	3.6	5.9	1.7	5.6	1.5	5.0	12.5	6.3	1.4
S	t_e	258.8	260.3	275.4	109.7	182.6	200.3	221.7	49.9	289.5
	Δt_e	8.3	8.8	5.1	42.0	3.5	6.0	14.8	6.1	2.7

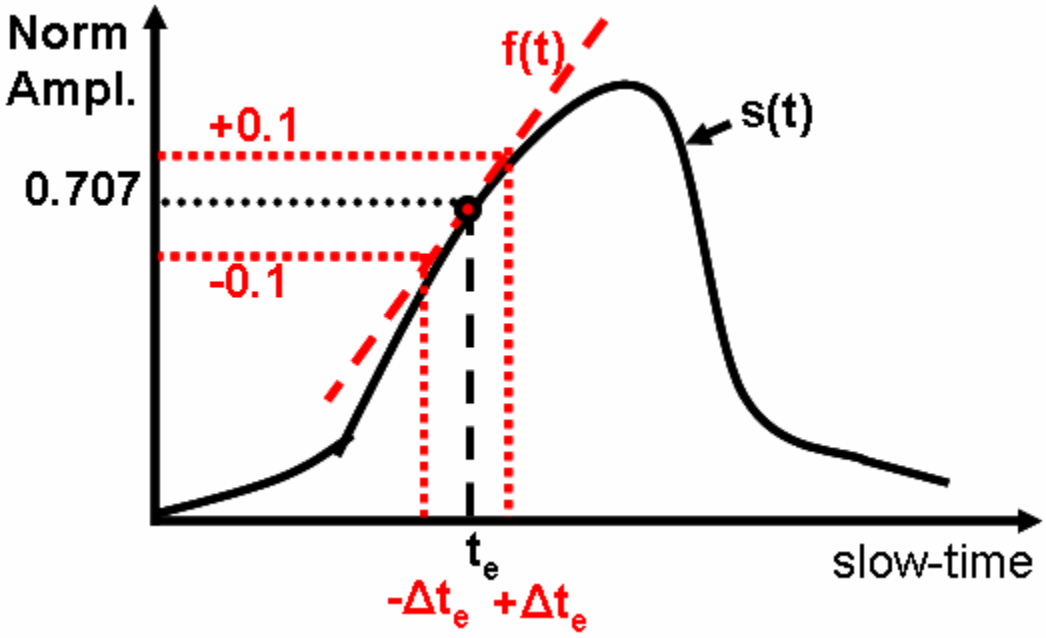

Figure 4.1. Diagram to illustrate measurement of onset latency (t_e). The solid black line is a normalized signal envelope s(t) in slow-time. The onset latency corresponded to the first time the envelope crossed s(t) = 0.707 (-3dB). The uncertainty in t_e, Δt_e, was estimated by fitting a line f(t) through (t_e ,s(t_e)) and finding the Δt_e such that f($t_e \pm \Delta t_e$) = s(t_e) ± 0.1.

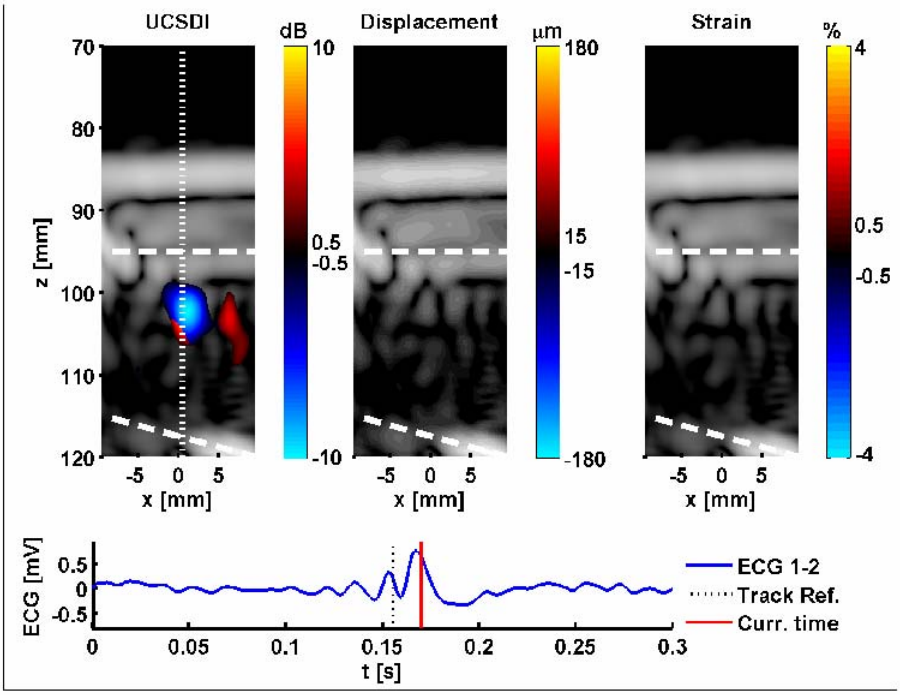

Figure 4.2. A screen shot, corresponding to t=170ms, from the movie Movie 4.1, when heart A was stimulated from the right atrium. Bottom: For reference is shown the low frequency ECG signal measured with electrodes 1-2. In the images on top from left to right: UCSDI, axial displacement, and axial strain are superimposed on top of B-mode ultrasound (dynamic range=30dB, grayscale). The magnitude of the UCSD image has been logarithmically compressed and given the sign of the real part.

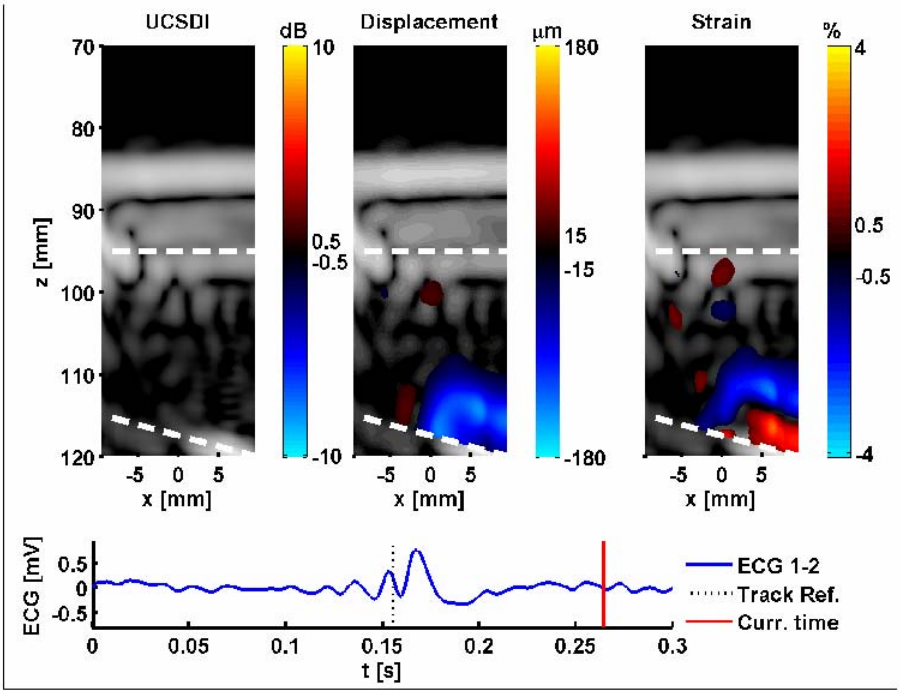

Figure 4.3. A screen shot, corresponding to t=264ms, from the movie Movie 4.1, when heart A was stimulated from the right atrium. Bottom: For reference is shown the low frequency ECG signal measured with electrodes 1-2. In the images on top from left to right: UCSDI, axial displacement, and axial strain are superimposed on top of B-mode ultrasound (dynamic range=30dB, grayscale). The magnitude of the UCSDI image has been logarithmically compressed and given the sign of the real part.

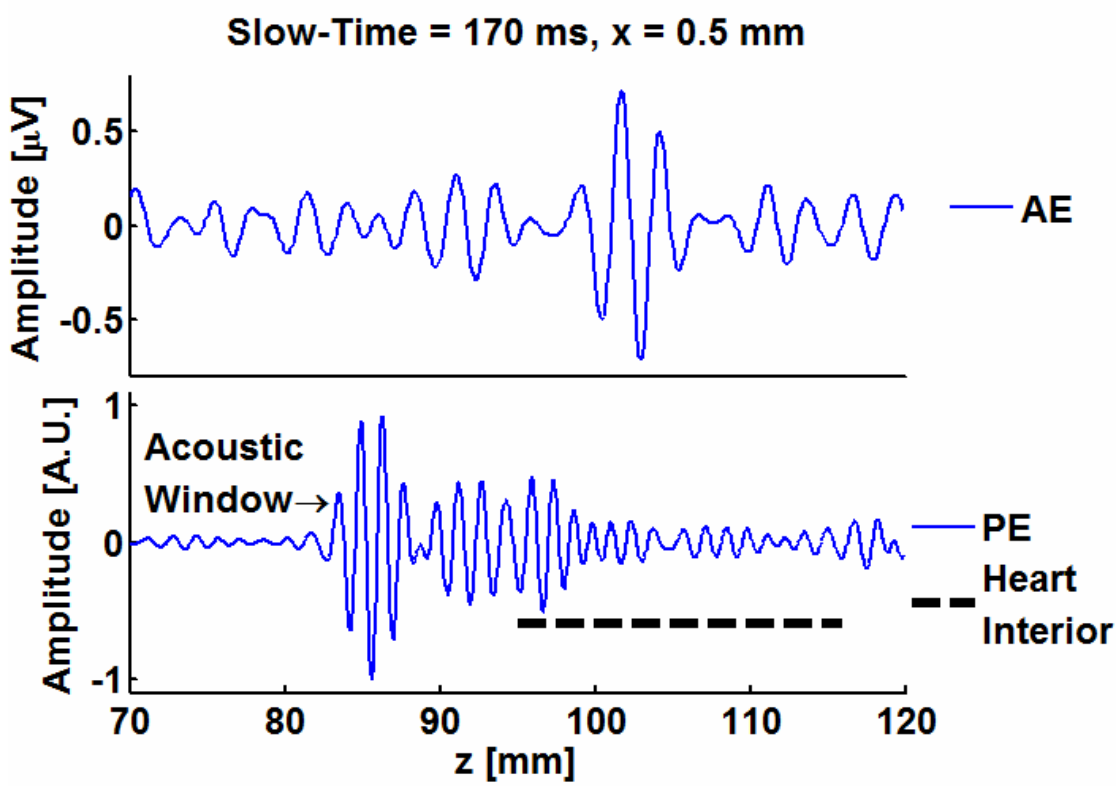

Figure 4.4. Example radio frequency traces corresponding to the white dotted vertical line in Fig. 4.2. The plot on the top is the AE trace while the plot on the bottom is the PE RF trace acquired concurrently at the same A-line. The black dashed horizontal line marks the interior of the heart.

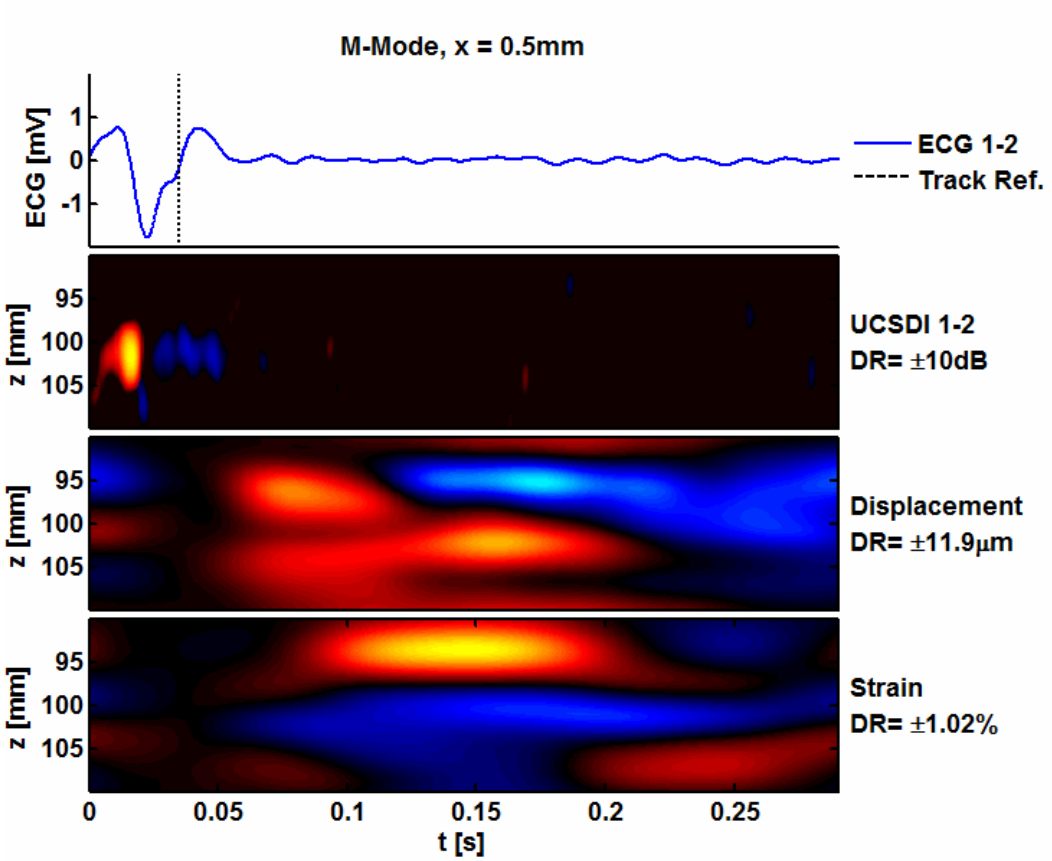

Figure 4.5. The bottom three panels are M-mode images corresponding to the line x= 0.5 mm. The dynamic range (DR) for each image is shown on the side of each image. Top: Conventional low frequency ECG measured with electrodes 1-2. The vertical dotted line corresponds to the reference frame for speckle tracking. Second to top: A bipolar UCSD image measured with electrodes 1-2 where the magnitude of the AE signal has been logarithmically compressed and given the sign of the real part. Second to bottom: Axial displacement estimate. Bottom: Axial strain estimate.

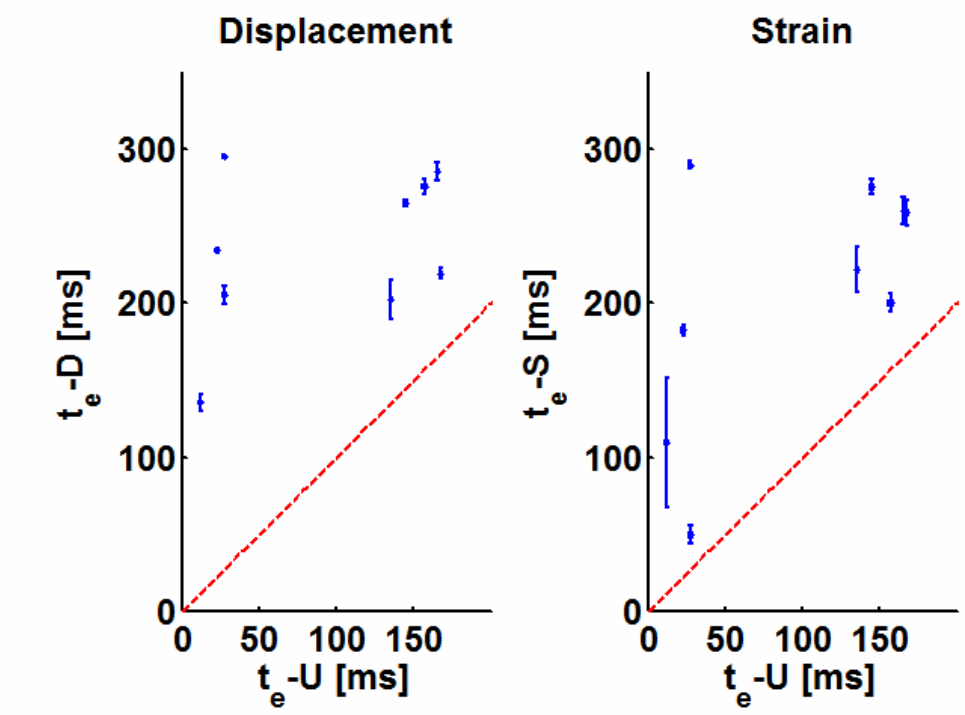

Figure 4.6. Scatter plots of the timing measurements tabulated in table 4.1. They combine measurements from hearts A and B. On the left, the onset time of the displacement (t_e-D) is plotted against the onset time of the UCSDI measurements (t_e-U). On the right the onset time of the displacement (t_e-S) is plotted against the onset time of the UCSDI measurements (t_e-U). In both plots the red dashed line represents where the two corresponding parameters are equal. We see that the UCSDI signal precedes both displacement and strain.

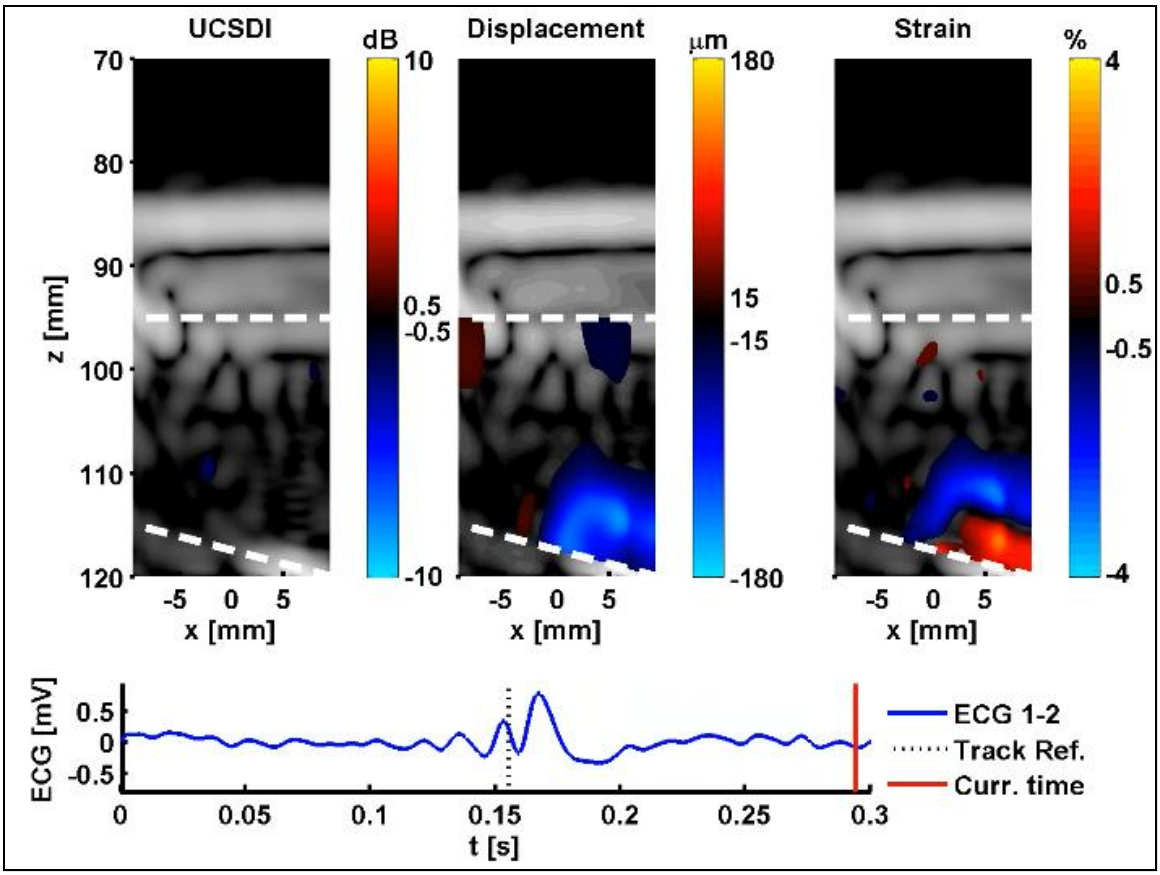

Movie 4.1. This is a movie of heart B, UCSDI and ECG are measured from electrodes 1-2 and the heart is stimulated at the apex.

4.5. References

[1] A. Auricchio and W. T. Abraham, "Cardiac resynchronization therapy: Current state of the art - Cost versus benefit," *Circulation,* vol. 109, pp. 300-307, Jan 2004.

[2] C. Leclercq and J. M. Hare, "Ventricular resynchronization - Current state of the art," *Circulation,* vol. 109, pp. 296-299, Jan 2004.

[3] C. M. Yu, J. W. H. Fung, Q. Zhang, and J. E. Sanderson, "Understanding nonresponders of cardiac resynchronization therapy - Current and future perspectives," *Journal of Cardiovascular Electrophysiology,* vol. 16, pp. 1117-1124, Oct 2005.

[4] P. R. Malmviou J., "Chapter 19: The Basis of ECG diagnosis," in *Bioelectromagnetism: Principles and applications of bioelectric and biomagnetic fields* New York: Oxford University Press, 1995, pp. 320-335.

[5] S. Ghio, C. Constantin, C. Klersy, A. Serio, A. Fontana, C. Campana, and L. Tavazzi, "Interventricular and intraventricular dyssynchrony are common in heart failure patients, regardless of QRS duration," *European Heart Journal,* vol. 25, pp. 571-578, Apr 2004.

[6] C. M. Yu, H. Yang, C. P. Lau, Q. O. Wang, S. Wang, L. Lam, and J. E. Sanderson, "Regional left ventricle mechanical asynchrony in patients with heart disease and normal QRS duration: Implication for biventricular pacing therapy," *Pace-Pacing and Clinical Electrophysiology,* vol. 26, pp. 562-570, Feb 2003.

[7] J. Gorcsan, T. Abraham, D. A. Agler, J. J. Bax, G. Derumeaux, R. A. Grimm, R. Martin, J. S. Steinberg, M. S. J. Sutton, and C. M. Yu, "Echocardiography for cardiac resynchronization therapy: Recommendations for performance and reporting - A report from the American Society of Echocardiography Dyssynchrony writing group - Endorsed by the Heart Rhythm Society," *Journal of the American Society of Echocardiography,* vol. 21, pp. 191-213, Mar 2008.

[8] E. McVeigh, O. Faris, D. Ennis, P. Helm, and F. Evans, "Electromechanical mapping with MRI tagging and epicardial sock electrodes," *Journal of Electrocardiology,* vol. 35, pp. 61-64, 2002.

[9] L. Gepstein, G. Hayam, S. Shpun, and S. A. BenHaim, "Hemodynamic evaluation of the heart with a nonfluoroscopic electromechanical mapping technique," *Circulation,* vol. 96, pp. 3672-3680, Nov 1997.

[10] L. Y. Rao, R. J. He, C. X. Ding, and D. S. Khoury, "Novel noncontact catheter system for endocardial electrical and anatomical imaging," *Annals of Biomedical Engineering,* vol. 32, pp. 573-584, Apr 2004.

[11] K. Kaluzynski, X. C. Chen, S. Y. Emelianov, A. R. Skovoroda, and M. O'Donnell, "Strain rate imaging using two-dimensional speckle tracking," *IEEE Transactions on Ultrasonics Ferroelectrics and Frequency Control,* vol. 48, pp. 1111-1123, Jul 2001.

[12] W.-N. Lee, C. M. Ingrassia, S. D. Fung-Kee-Fung, K. D. Costa, J. W. Holmes, and E. E. Konofagou, "Theoretical Quality Assessment of Myocardial Elastography with In Vivo Validation," *IEEE Trans. Ultrason. Ferroelectr. Freq. Control,* vol. 54, pp. 2233-2245, 2007.

[13] Y. Notomi, P. Lysyansky, R. M. Setser, T. Shiota, Z. B. Popović, M. G. Martin-Miklovic, J. A. Weaver RT, S. J. Oryszak, N. L. Greenberg, R. D. White, and J. D. Thomas, "Measurement of Ventricular Torsion by Two-Dimensional Ultrasound Speckle Tracking Imaging " *Journal of the American College of Cardiology* vol. 45, pp. 2034-2041, 2005.

[14] C. Jia, R. Olafsson, K. Kim, T. J. Kolias, J. M. Rubin, W. F. Weitzel, R. S. Witte, S.-W. Huang, M. S. Richards, C. X. Deng, and M. O'Donnell, "2D Cardiac Elasticity Imaging on a Controlled Isolated Rabbit Heart," *Ultrasound in Medicine & Biology,* vol. In submission, 2008.

[15] M. A. Lubinski, S. Y. Emelianov, and M. O'Donnell, "Speckle tracking methods for ultrasonic elasticity imaging using short-time correlation," *IEEE Transactions on Ultrasonics Ferroelectrics and Frequency Control,* vol. 46, pp. 82-96, Jan 1999.

[16] M. A. Lubinski, S. Y. Emelianov, K. R. Raghavan, A. E. Yagle, A. R. Skovoroda, and M. O'Donnell, "Lateral Displacement Estimation using Tissue Incompressibility," *IEEE Transactions on Ultrasonics, Ferroelectrics, and Frequency Control,* vol. 43, pp. 234-246, 1996.

[17] M. A. Lubinski, S. Y. Emelianov, and M. O'Donnell, "Speckle Tracking Methods for Ultrasonic Elasticity Imaging Using Short Time Correlation," *IEEE Transactions on Ultrasonics, Ferroelectrics, and Frequency Control,* vol. 46, pp. 82-96, 1999.

[18] P. Sogaard, H. Egeblad, W. Y. Kim, H. K. Jensen, A. K. Pedersen, B. O. Kristensen, and P. T. Mortensen, "Tissue Doppler imaging predicts improved systolic performance and reversed left ventricular remodeling during long-term cardiac resynchronization therapy," *Journal of the American College of Cardiology,* vol. 40, pp. 723-730, Aug 2002.

CHAPTER 5
CONCLUSIONS AND FUTURE WORK

5.1. Conclusions and Contribution of This Work

The primary goal of this dissertation was to develop a method (UCSDI) to detect and map cardiac currents using ultrasound through the acousto-electric effect. Existing methods are time consuming and produce coarse and static activation maps. The promise of UCSDI is that it potentially achieves high spatial resolution determined by the ultrasonic point spread function, fast 3D imaging with electronic beam steering, and is automatically registered to B-mode ultrasound. UCSDI is potentially a powerful diagnostic visualization technique that could combine electrical mapping with quantitative ultrasound volume and strain measurements.

In Chapter 1 the theoretical basis for AE measurements and UCSDI was presented, the AE signal equation derived, and the sifting property of the ultrasonic beam in UCSDI illustrated. A validation study of UCSDI was described in Chapter 2. A two dimensional (2D) current distribution was generated and mapped independently with UCSDI and conventional methods. Both measurements were validated with a finite element simulation. The ability of UCSDI to significantly characterize the current source and its location with only a single pair of electrodes was demonstrated. By combining UCSD images from a number of electrodes, it was possible to reconstruct the current density and

locate monopolar sources to within 1 mm of their true location without making prior assumptions regarding the source.

The ability of UCSDI to map biological currents was demonstrated in Chapter 3. In these experiments electrocardiograms (ECG) and AE signals were measured using tungsten electrodes embedded in the left ventricle of an isolated rabbit heart. The heart was perfused with an excitation contraction decoupler to reduce motion. The resulting UCSD images had spatial and temporal patterns consistent with the spreading activation wave and coincided temporally with ECG signals acquired simultaneously. With comparison to B-mode ultrasound images, AE signals appeared to originate in the heart wall. Control experiments revealed the dependence of AE signals on the presence of ultrasound.

A new method for electromechanical imaging combining UCSDI and ultrasonic strain imaging was introduced in Chapter 4. This chapter presented the first movies of both UCSDI and displacement images automatically registered to B-mode ultrasound, as well as the first localized measurements of electromechanical delay.

The main contributions of the work presented in this thesis are summarized below

- The acousto-electric signal equation was rewritten into a more useful form for imaging.
- An imaging technique, Ultrasound Current Source Density Imaging (UCSDI), was developed. It was tested by mapping a 2D current distribution, which was independently measured with other methods.
- A method to reconstruct current densities based on UCSDI was developed.

- Cardiac activation currents were detected and mapped for the first time using UCSDI in an isolated rabbit.
- The first electromechanical ultrasound images were formed by combining UCSDI and phase-sensitive speckle tracking.

The work of Chapter 2 was presented at the 2007 SPIE Medical Imaging Conference and published in the IEEE Transactions on Biomedical Engineering, with citations given below.

- R. Olafsson, R. S. Witte, and M. O'Donnell, "Measurement of a 2D electric dipole field using the acousto-electric effect - art. no. 65130S," in *Medical Imaging 2007: Ultrasonic Imaging and Signal Processing*. vol. 6513, S. Y. Emelianov and S. A. McAleavey, Eds., 2007, pp. S5130-S5130.
- R Olafsson, RS Witte, S-W Huang and M. O'Donnell. "Ultrasound Current Density Imaging" *IEEE Transactions on Biomedical Engineering*, in press (Jul 2007).

The work of Chapter 3 was presented at the 2006 SPIE Medical Imaging Conference, 2007 IEEE International Ultrasonics Symposium, and has been submitted to the IEEE Transactions on Ultrasonics, Ferroelectrics and Frequency Control.

- R. Olafsson, R. S. Witte, K. Kim, S. Ashkenazi, and M. O'Donnell, "Electric current mapping using the acousto-electric effect - art. no. 61470O," in *Medical Imaging 2006: Ultrasonic Imaging and Signal Processing*. vol. 6147, S. Y. Emelianov and W. F. Walker, Eds., 2006, pp. O1470-O1470
- R. Olafsson, C. Jia, S.-W. Huang, R. S. Witte, and M. O'Donnell, "Detection of Electrical Current in a Live Rabbit Heart using Ultrasound," in *2007 IEEE Ultrasonics Symposium*, New York, NY, 2007, pp. 989-992.
- R Olafsson, R.S. Witte, C. Jia, S-W. Huang, K. Kim and M O'Donnell, "Cardiac Activation Mapping Using Ultrasound Current Source Density

Imaging (UCSDI)", submitted to *IEEE Transactions on Ultrasonics, Ferroelectrics, and Frequency Control.*

5.2. Future Experiments

5.2.1. Increase Acquisition Speed and Spatial Resolution with a Clinical Phased Array

The experiments described in Chapters 3 and 4 mapped the activation currents of a live heart by mechanically scanning a low frequency single element transducer. That transducer was chosen to maximize sensitivity. For UCSDI to be competitive as a cardiac mapping method, spatial resolution must be improved and data acquisition must be done more rapidly. A way to achieve both is to use a phased array.

To test this idea, a clinical ultrasound scanner was used to create the ultrasound modulation for an UCSDI experiment. In this preliminary test an artificial current distribution in a cadaver rabbit heart was mapped. The experimental geometry is illustrated in Fig. 5.1. Four electrodes were inserted into the left ventricle of a heart immersed in mineral oil for electrical insulation. A clinical phased array (PA4-20/20, Ultrasonix Medical Corporation, Richmond, BC, Canada) was aimed at the heart from below such that the long axis of the heart was within the imaging plane. The phased array was connected to a fully programmable clinical scanner (Sonix RP, Ultrasonix Medical Corporation, Richmond, BC, Canada). Each frame was composed of 63 A-lines with 1^0 spacing. The pulse sent along each A-line was 10 cycles long with a center frequency of 2.5 MHz.

A 200 Hz square wave current was injected by a signal generator (33120A, Agilent, Santa Clara, CA) through the outer electrodes, which were made of silver. The inner electrodes, made of tungsten, were connected through an analog high pass filter (-3dB cutoff frequency = 500kHz) to a differential amplifier (1855A, LeCroy, Chestnut Ridge, NY). The signal was further amplified 30 dB (5077PR, Panametrics Inc., Waltham, MA) and then sampled and digitized with a data acquisition (DAQ) board.

Experimental timing was controlled by a Field-Programmable Gate Array (FPGA) (ezFPGA, Dallas Logic, Plano, TX) and is is illustrated in Fig. 5.2. At the center of each current peak, the FPGA sent out an A-line trigger to both the Sonix RP and the DAQ board.

The current injected through the silver electrodes was varied from 0, 3, 8, 16, 24 mA. The results are shown in Fig. 5.3 where AE data corresponding to different current levels are superimposed on top of B-mode ultrasound images. The figure shows two rows. In the top row are uncorrected data while the bottom row has corrected data. We see that for the uncorrected data, there is a detected signal without any current injection. This artifact is due to the so called Debye effect or separation by pressure of ions with equal charge, opposite polarity, and unequal mass. Since this signal does not depend on external current density the data can be corrected as others have shown [1] by subtracting the 0 mA image from the other images. After subtracting the control, we see a progression in the corrected UCSDI signal magnitude with the magnitude of the injected current.

Although these results are preliminary, they suggest that sufficient sensitivity can be realized for high resolution UCSDI using a conventional diagnostic imaging system.

5.2.2. Measurement of UCSDI Detection Volume

It would be desirable to gauge how far away from the electrode the activation wave can be detected with UCSDI. In the experiments presented in Chapter 3, the exact location of the electrodes within the imaging plane was not known. As a result, it is difficult to make a clear conclusion about this issue from that data. An experimental setup that could address this question is described below.

One way to measure the position of electrodes is an electro-anatomical system based on electric field measurements, such as Ensite^{TM} (LocaLisa component) as described in Chapter 1 [2, 3] and depicted in Fig. 1.4. By doing a cross-calibration between the ultrasonic field of view and the electro-anatomic system, it is possible to know the location of each electrode within the imaging field.

A schematic of a potential experimental setup is depicted in Figs. 5.4 and 5.5. The description of the setup will be 2D but extension to 3D is trivial. The experimental chamber will be rectangular of side length d with a large plate-electrode on each side. The sides of the chamber will be parallel to the x- and y-axis. At the bottom, there will be an acoustic window through which an ultrasonic phased array (PA) is pointed. If the chamber is filled with saline and the plate electrodes parallel to the x-axis connected to a voltage source V_0, an electrode (red dot in Fig. 5.4) placed at coordinate (x,y) will measure voltage V_y. Similarly, if the voltage source is connected to the plates parallel to the y-axis, the electrode measures voltage V_y. In an ideal system the relationship between (V_x,V_y) and (x, y) is simply

$$(x, y) = (V_x, V_y)\frac{d}{V_0}. \tag{5.1}$$

To calibrate the coordinate system of the imaging plane of the phased array with the electro-anatomical system, a thin insulated wire with an exposed tip can be moved with a translation stage in discrete steps in a rectangular pattern encompassing the imaging field. The thin wire will register in the ultrasound image as a point, and the electro-anatomical system can track the tip of the electrode. At each node of the rectangular pattern, an ultrasound image is taken and an electro-anatomical measurement is acquired. In post-processing it is possible to get a mathematical transformation between the two coordinate systems. A wire target allows an accurate measurement of the ultrasound point spread function at each point in the imaging field, further facilitating analysis.

After calibration, an isolated heart is placed in an epicardial sock electrode array as depicted in Fig. 5.5. Because of the calibration, the location of each electrode in the array can be measured. From the measured acoustic point spread function at each point in space, and from the knowledge of each electrode within the imaging plane, it is possible to estimate how far away from the electrodes it is possible to detect the activation wave using UCSDI.

5.2.3. Effect of Motion on UCSDI

The UCSDI images in Chapter 3 were made in an isolated heart perfused with the excitation contraction decoupler BDM to significantly reduce motion. This was done to ensure that the detected signals were not motion artifacts. Chapter 4 demonstrated that the absolute maximum displacement was miniscule (0.2 mm). It has been shown that BDM

reduces heart contractions in a dose dependent manner and, thus, is convenient for gauging motion artifacts and assessing speckle tracking algorithms [4, 5].

The plan would be to measure UCSDI in an isolated heart perfused with progressively smaller doses of BDM from a maximum (15 mM) to no BDM (0 mM) and to see if there is any detectable change in the morphology and timing of the detected UCSDI signal.

If motion artifacts are significant, it is possible to investigate possible compensation techniques. For example, ultrasound speckle tracking can be used to measure the timing of local contractions relative to other signals or potential artifacts.

5.2.4. Spatial Error of UCSDI Activation Map

A common method to evaluate the accuracy of activation wave mapping is to measure its spatial error that is, how well a method can locate a single pacing electrode [6]. The spatial error is the difference between the actual location of the electrode and the location estimated from the activation map.

The setup, shown in Figs. 5.4 and 5.5 and described in Section 5.2.2., can be used to perform these experiments. A single electrode in the epicardial sock can be picked at random to stimulate and the remaining electrodes can be used to record. Both UCSDI and normal epicardial mapping can image the activation wave because the actual location of the stimulating electrode is known from the calibration step; it is possible to calculate the spatial error for both methods. For each heart, it is possible to repeat this experiment many times.

5.2.5. Extend Reconstruction of Current Density to Three Dimensions.

The reconstruction algorithm introduced in Chapter 3 is only valid for 2D current distributions under the assumptions that for slabs, thin along the beam axis, it is possible to separate the beam pattern into independent lateral and axial components. This method could possibly be applied to 3D problems if the point spread function is assumed to be space-invariant. In actuality, the point spread function varies with space due to the non-trivial 3D shape of acoustic beams [7]. This question could be addressed in simulation studies using a combination of the Field II™ package [8, 9] to simulate the acoustics and Comsol™ (Comsol AB, Stockholm, Sweden) finite element software to simulate the lead fields and activation wave. In Chapter 2 we used Comsol to simulate lead fields, and we have previously used Field II™ to simulate a simple UCSDI image [10].

5.2.6. Effect of Electrode Position on Current Source Density Reconstruction

In Chapter 2, it was shown that UCSDI can significantly determine source geometry of distributed current sources using just a single pair of electrodes. A current source distribution could be reconstructed with a simple algorithm when using UCSDI with multiple electrodes. Although this reconstruction algorithm is less sensitive to geometrical errors than traditional inverse algorithms, it nevertheless makes some assumptions about the conductivity distributions in calculating the transfer matrices. The sensitivity of this reconstruction algorithm could be explored through the simulation scheme outlined in Section 5.2.5. The inverse algorithm assumes that the recording

electrodes are in a certain location. To test the sensitivity of the outcome of the algorithm to this assumption, the location of the electrodes could be varied in a simulation protocol.

5.3. Potential Clinical Application

In Section 5.2.1 the ability of a clinical, transthoracic phased array to generate UCSDI was shown. Applying a transthoracic transducer with intracardiac electrodes would be a straightforward extension of UCSDI. However this approach has two disadvantages. The first, transthoracic echocardiography offers limited views of the heart as compared to intracardiac ultrasound due to the presence of the ribcage [11]. Second, in this approach, the relative geometry of the ultrasound imaging field relative to the electrodes would not be known. As a result, combining measurements from multiple electrodes might be difficult, such as in the reconstruction algorithm presented in Section 2.3.2, for example. In the ideal system the relative geometry between electrodes and transducer would be fixed and known. A practical implementation of this ideal would be a catheter with both a high density ultrasound array and sparse electrode array. Such a device has been created and reported elsewhere [12, 13]. However these devices have high frequency transducers that might be unsuitable for use with UCSDI, given the small signal size of UCSDI and because of the spatial filtering effects that can occur during the measurement process (see Fig. 2.5 for an example). A conceptual first generation catheter for use with UCSDI is depicted in Figure 5.7. In this figure, a "hockey stick" style ultrasound phased array catheter (center frequency < 5MHz) is encased in an inflatable balloon. Attached to the balloon is an array of electrodes similar to the Ensite^{TM} array, depicted in Figure 5.7 on the right [14]. Unlike the Ensite^{TM} array, the wires would not

surround the entire surface of the balloon; they would radiate, like the pedals of a flower, from either side of the array, leaving a gap through which the ultrasound beams could be less impeded. A side firing array can have a sizeable aperture at a low frequency and thus decent lateral resolution. The inflatable balloon array would also allow the electrodes to be in close proximity to the heart wall. This would increase the sensitivity of the electrical measurement. Even this first generation device could have a great impact in the clinic. An operator with this device would not only have at his disposal UCSDI images of the electrical activity within the ultrasonic field of view and local strain maps, he would also be able to see the ablation catheter or pacemaker lead in the image. Navigation of an ablation catheter or a pacemaker lead to an optimal position could, therefore, be made much simpler and intuitive.

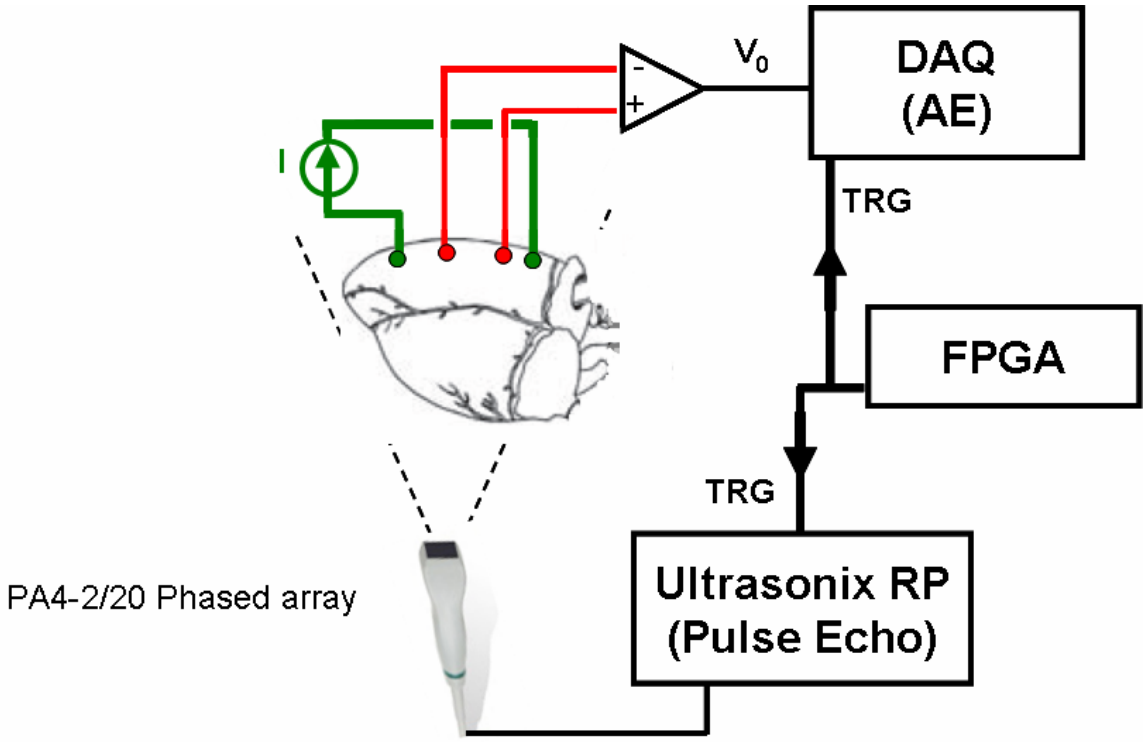

Figure 5.1. Experimental geometry. A dead rabbit heart was placed in a tank of oil with the Ultrasonix PA4-2/20 Phase Array pointed from below. The timing was controlled by an FPGA which simultaneously triggered the Ultrasonix A-line trigger and a DAQ board that acquired AE signals.

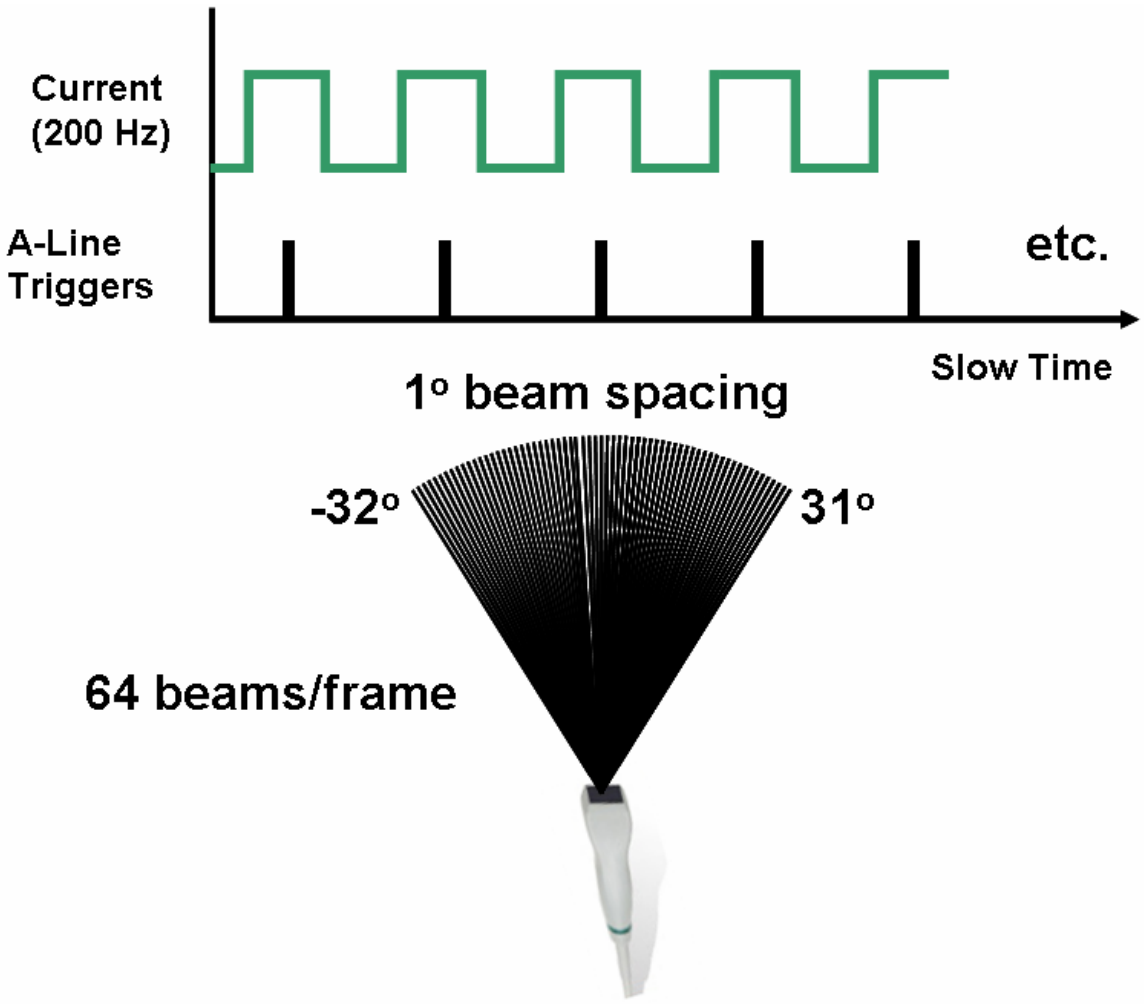

Figure 5.2. Experimental timing. There were 64 beams fired per frame with 1^0 spacing from -32 to 31^0. Each A-line is triggered to fire at the peak of the 200 Hz square wave current.

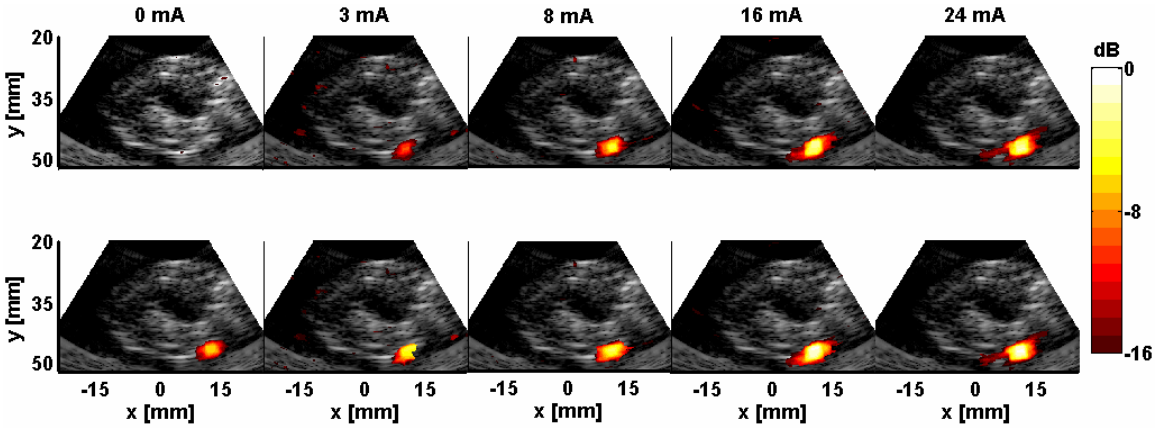

Figure 5.3. UCSDI images of current injected into a rabbit heart, shown left to right as a function of the magnitude of the current. The bottom row shows the actual measurements while the top row show the measurement with the vibration potential artifact measured for 0 mA subtracted.

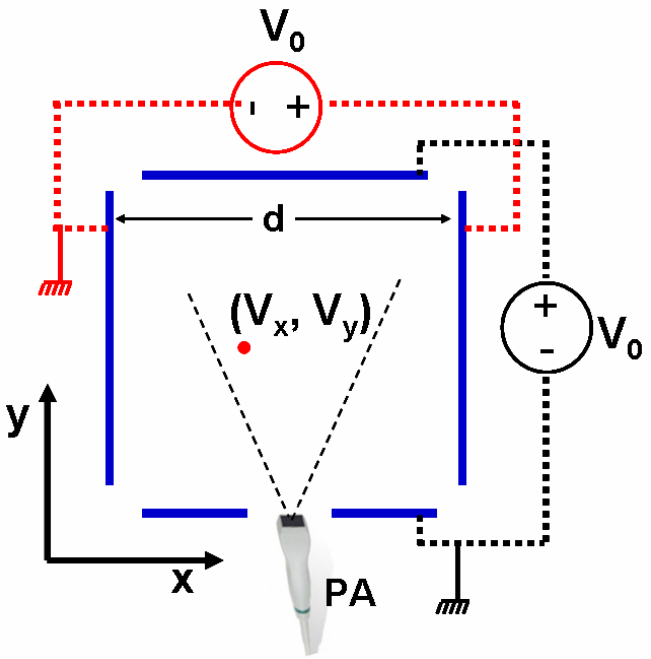

Figure 5.4. A schematic of a calibration between the imaging plane of a phased array and an electro-anatomical system. The calibration is accomplished by moving a electrode (red dot) in a rectangular grid which encompasses the imaging plane of the phased array. At each location (x,y) the electrode measures voltages (V_x,V_y) due to electric fields produced by two pairs of orthogonally placed plate electrodes with voltage V_0. If the plates are large enough and the distance (d) between them is known it is possible to measure the location (x,y) from the voltages (V_x,V_y). At each point in the rectangular grid an ultrasound image is collected in which the wire electrode will register as a point.

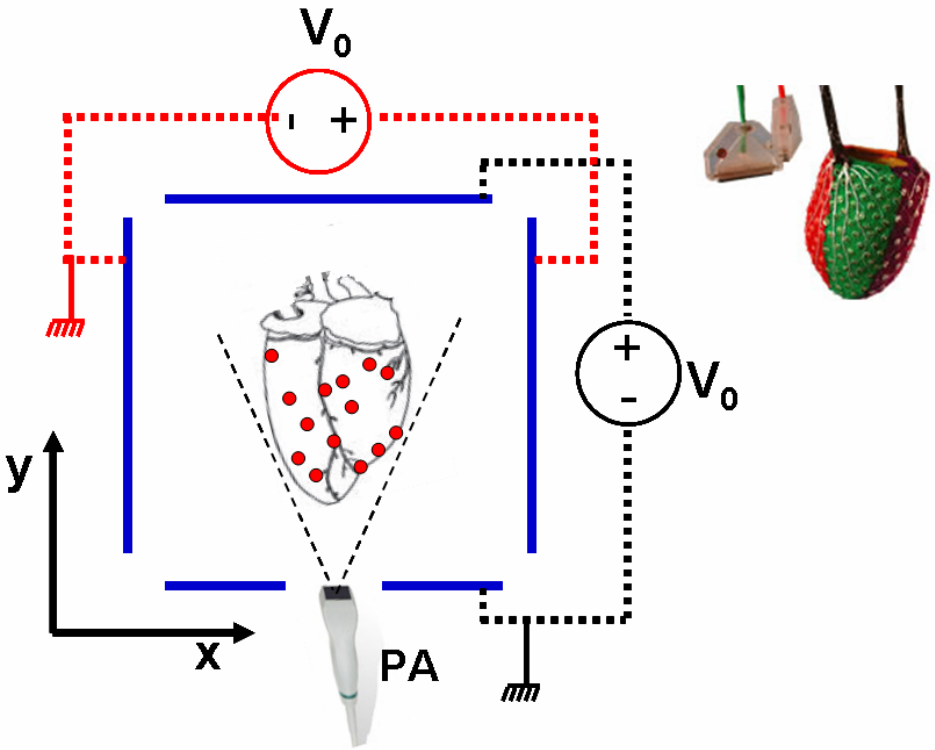

Figure 5.5. An isolated heart is placed inside an epicardial sock with an array of electrodes (shown in upper right corner). From the calibration between the ultrasound imaging field and the electroanatomical system the location of every electrode in the sock within the ultrasound imaging field is known. With this experimental setup it is possible to measure how far away from the electrodes UCSDI can detect the activation wave. This setup can be used to gauge the ability of UCSDI imaging system to find a pacing location, a stand in for focal arrhythmia. The picture of the epicardial electrode sock is from the home page of UnEmap systems in Auckland, New Zealand [15].

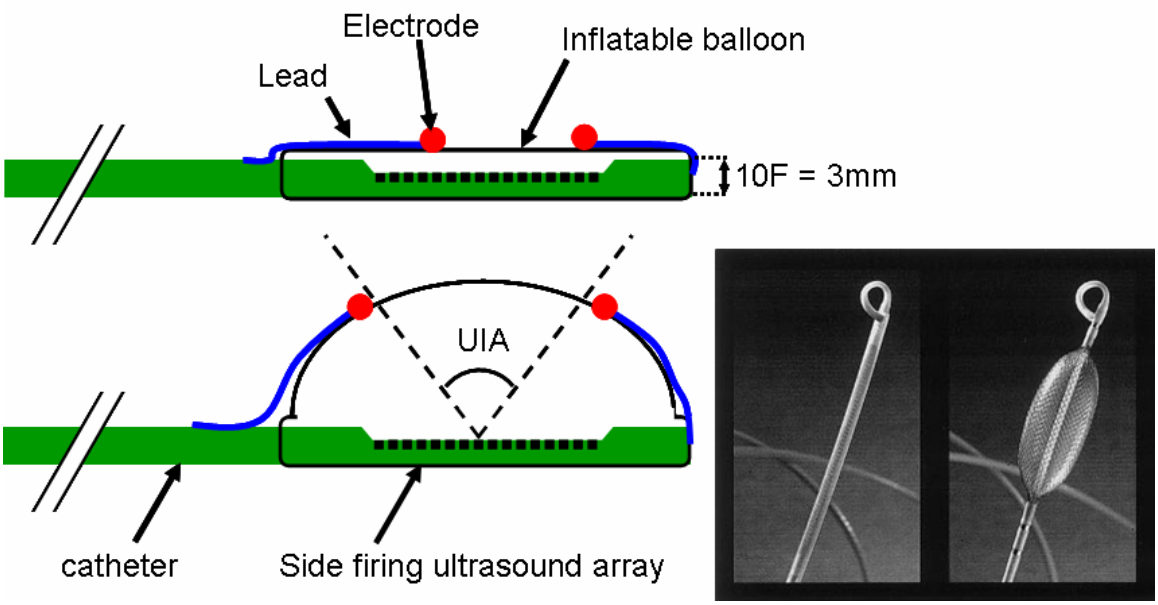

Figure 5.6. An sketch of a possible catheter with a high density side firing ultrasound array and a sparse electrode array. Surrounding the ultrasound array is an inflatable balloon on which are attached electrodes. The figure on top is prior to balloon inflation and the figure on the bottom is after inflation (UIA=ultrasound imaging arc). An example of an inflatable electrode array is the Ensite system depicted in the photograph on the right. The photograph is adapted from [14].

5.4. References

[1] J. Jossinet, B. Lavandier, and D. Cathignol, "Impedance modulation by pulsed ultrasound," *Electrical Bioimpedance Methods: Applications to Medicine and Biotechnology,* vol. 873, pp. 396-407, 1999.

[2] S. Markides V., O.R., Tondato F., Peters N.S., "Chapter 93: Mapping," in *Cardiac Electrophysiology: From Cell to Bedside*, D. P. Zipes, Jalife J., Ed. Philidelphia, Pennsylvania: Saunders, 2004, pp. 858-868.

[3] F. H. M. Wittkampf, E. F. D. Wever, R. Derksen, A. A. M. Wilde, H. Ramanna, R. N. W. Hauer, and E. O. R. de Medina, "LocaLisa - New technique for real-time 3-dimensional localization of regular intracardiac electrodes," *Circulation,* vol. 99, pp. 1312-1317, 1999.

[4] O. Jia C., R., Kim, K., Kolias T. J., Rubin, J. M., Weitzel,W.F., Witte, R.S., Huang, S.-W., Richards, M. S., Deng, C.X. and O'Donnell, M., "2D Cardiac Elasticity Imaging on a Controlled Isolated Rabbit Heart," *Ultrasound in Medicine & Biology,* vol. In submission, 2008.

[5] S. Kettlewell, N. L. Walker, S. M. Cobbe, F. L. Burton, and G. L. Smith, "The electrophysiological and mechanical effects of 2,3-butane-dione monoxime and cytochalasin-D in the Langendorff perfused rabbit heart," *Experimental Physiology,* vol. 89, pp. 163-172, Mar 2004.

[6] L. Y. Rao, H. B. Sun, and D. S. Khoury, "Global comparisons between contact and noncontact mapping techniques in the right atrium: Role of cavitary probe size," *Annals of Biomedical Engineering,* vol. 29, pp. 493-500, Jun 2001.

[7] B. Angelsen, "Chapter 5: Radiation field from a single element transducers," in *Ultrasound Imaging: Waves Signals and Signal Processing,*. vol. I Norway: Emantec, 2000, pp. 5.1-5.97.

[8] J. A. Jensen, " Field: A Program for Simulating Ultrasound Systems,," in *10th Nordic-Baltic Conference on Biomedical Imaging published in Medical & Biological Engineering & Computing*. vol. 34, 1996, pp. 351-353.

[9] J. A. Jensen and N. B. Svendsen, "Calculation of pressure fields from arbitrarily shaped, apodized, and excited ultrasound transducers," *IEEE Transactions on Ultrasonics Ferroelectrics and Frequency Control,* vol. 39, pp. 262-267, 1992.

[10] R. Witte, S., Olafsson, Ragnar and O'Donnell, Matthew, "Acousto-electric detection of current flow in a neural recording chamber," in *2006 IEEE International Ultrasonics Symposium*, Vancouver, BC, Canada, 2006, pp. 5-8.

[11] J. S. Hung, M. Fu, K. H. Yeh, C. J. Wu, and P. Wong, "Usefulness of intracardiac echocardiography in complex transseptal catheterization during percutaneous transvenous mitral commissurotomy," *Mayo Clinic Proceedings,* vol. 71, pp. 134-140, Feb 1996.

[12] X. K. Li, J. Pemberton, K. Thomenius, A. Dentinger, R. I. Lowe, M. Ashraf, K. K. Shung, R. Chia, D. N. Stephens, M. O'Donnell, A. Mahajan, S. Balaji, K. Shivkumar, and D. J. Sahn, "Development of an electrophysiology (EP)-Enabled intracardiac ultrasound catheter integrated with NavX 3-dimensional electrofield mapping for guiding cardiac EP interventions - Experimental studies," *Journal of Ultrasound in Medicine,* vol. 26, pp. 1565-1574, Nov 2007.

[13] L. Y. Rao, R. J. He, C. X. Ding, and D. S. Khoury, "Novel noncontact catheter system for endocardial electrical and anatomical imaging," *Annals of Biomedical Engineering,* vol. 32, pp. 573-584, Apr 2004.

[14] C. C. Gornick, S. W. Adler, B. Pederson, J. Hauck, J. Budd, and J. Schweitzer, "Validation of a new noncontact catheter system for electroanatomic mapping of left ventricular endocardium," *Circulation,* vol. 99, pp. 829-835, Feb 16 1999.

[15] "UnEmap-system : High channel count electrical mapping and pacing," [Online document], [cited 2008 Mar 31], Available HTTP: http://www.bioeng.auckland.ac.nz/commercial/unemap/unemap_electrodes.htm.